

# The formation of ultracold rubidium molecules using ultrafast photoassociation

David J. M<sup>c</sup>Cabe  
St Cross College, Oxford



Submitted for the degree of Doctor of Philosophy  
Michaelmas Term 2009

Supervised by  
Prof. Ian A. Walmsley

Clarendon Laboratory  
University of Oxford  
United Kingdom

To my grandfather

# The formation of ultracold rubidium molecules using ultrafast photoassociation

David J. McCabe  
St Cross College, Oxford

Submitted for the degree of Doctor of Philosophy  
Michaelmas Term 2009

## ABSTRACT

The establishment of robust laser-cooling techniques for the formation of ultracold atoms has provided a test-bed for low-temperature science, with scattering events changing character from incoherent thermal interactions to coherent quantum mechanical events. A natural extension is the pursuit of ultracold molecules in prescribed low-energy internal states. Atomic cooling techniques, however, do not generalize to the molecular regime due to the complex energy-level structure afforded by its extra degrees of motion.

An indirect approach to ultracold molecule formation — photoassociation using ultrafast laser pulses — is the focus of this thesis. A broadband field associates atom pairs into a localized molecular wavepacket that evolves within the attractive excited-state potential. A suitably timed dump pulse may thus be applied to stabilize population into deeply bound ground vibrational states. This strategy may be generalized to any species whose spectroscopy matches the pulse spectrum, and offers a coherent population transfer scheme that does not require precise knowledge of the system.

This thesis presents experiments using high-energy photoassociation pulses applied to ultracold rubidium atoms. The pulses quench the background ground-state molecular population but form bound dimers within the excited state. A pump-probe experiment was designed to chart the excited-state dynamics; however, the oscillations predicted by theoretical calculations were not evident in the molecular signal.

The nature of the dynamics is expected to be strongly dependent on the initial state of the atom pairs addressed by the ultrafast pulse: a bound molecular population provides an additional candidate to free atoms. A spectroscopic measurement characterizes these bound molecules and identifies their formation mechanism. A subsequent experiment provides evidence that the predominant contributor to the pump-probe signal is the unbound initial population. The consequences with regard to both the observation of excited-state dynamics and the subsequent application of a dump pulse are discussed.



## Acknowledgements

*A Warrior of Light knows that he has much to be grateful for.*

I have a confession. Reading back through the contents of this thesis has instilled me with a niggling sense of foreboding that it doesn't *really* tell the story. Granted, it offers — I hope — a veneer of veracity and scientific integrity. But it falls palpably short of capturing what I've *actually* been up to over the last four-and-a-bit years. Alas that tale of workshop bodes, *Gladiator*-themed LabVIEW, late-night data sessions and the daring capture of Corsican hill forts will have to go untold. A token insight, however, may be gleaned by reading both along and between the following lines. A certain degree of indulgence is traditionally tolerated within the sanctuary of one's acknowledgements. I intend to abuse this concession unashamedly through a hotchpotch of effusive thank-yous, indulgent remarks and oblique references to in-jokes. So there.

Foremost thanks are due to my supervisor, Prof. Ian Walmsley, within whose research group it has been a pleasure and a privilege to work. Ian's insightful guidance on the experiment, together with his forbearance during the setbacks, were always much appreciated. I am likewise obliged to Prof. Chris Foot, whose advice and experience have been invaluable during the construction of the new BEC experiment.

Much gratitude is due to the pantheon of molecules colleagues with whom I have shared these experiments. Alex Dicks was welcoming upon my arrival, and both helpful and patient with his explanations of molecular spectroscopy. Antoine Monmayrant was a bewildering bundle of energy, and my ear drums are still recovering. Duncan England deserves an all-round and eclectic thank-you, ranging from his technical skills and lab savvy ('Bigger problem? *Bigger hammer!*'), through his marvellous repertoire of impressions, to all the half-trackers and 'M<sup>c</sup>Cabe-cutters' he served up in the nets. Please make sure he gets fed when I'm gone. Jovana 'Mini-boss' Petrovic — the greatest Serbian cricketer — was a welcome addition to the team and the lab, with her no-nonsense approach perfectly suited to the unenviable task of keeping the rest of us in order. Béatrice Chatel's visits were always a welcome boost for the experiment, and I look forward to working with her in Toulouse. Much fun was had building the BEC with 'General' Giuseppe Smirne and fellow dwellers of the basement lair. And Hugo Martay is a phenomenon of a tamed theorist. Thanks for tolerating all my stupid questions, keeping Optics Quotes solvent, and eating my breakfast. I'm so sorry about the bike...

The roll call must also be extended in general to the rest of the Ultrafast family, and in particular to a number of ‘Warriors of Light’. The first ‘high-five’ goes to Monty ‘Phil’ Bustard, for keeping me ever on my toes through stimulating discussions — ranging from the philosophical ramifications of phase-locked cw lasers to the best way to cook anything from bankers to potatoes. Shame you never did tell me about that putt, chap. Ben Sussman was my go-to man for physics, rock and roll, and everything in between. Brian Smith’s formidable mind hosts a struggle between razor-sharp physicist and all-American frat boy, with neither party showing signs of letting up. The resident SPIDER-men (Dane Austin, Tobias Witting and Adam Wyatt) were always generous with their advice and help. Every workplace needs a Klaus Reim, in which gentleman’s company is it impossible to be downcast. Josh Nunn truly understands what it is to drink tea.

I am indebted to the departmental support staff for sharing their experience and expertise throughout. Sue Gardner, Aga Borkowska and Kamna Pruvost offered continual guidance through the murky waters of departmental bureaucracy, and organized some memorable group dinners. Graham Quelch kept us on the *safe* and narrow in the basement, and plays a mean blues harp. Rob Harris, Simon Moulder and Bill Seagar were a mine of information, experience and entertainment, and the motivation for many a spurious trip to the research workshop. Alan Francis and Mohammed Cheddi ruled over a wealth of exciting riches within the magic sliding shelves of Stores. The building services team, notably Alan Hodgson and George Dancer, were always most accommodating to our regular pleas for help. And Leo Catney held both the departmental purse strings and Jack Cox new ball with equal aplomb.

Finally, sincerest thanks are due to my parents, the rest of my family, and to Mel for supporting and encouraging me during the ebbs and flows of my D. Phil.

## Table of abbreviations

*A Warrior of Light knows that certain moments repeat themselves.*

<i>Abbreviation</i>	<i>Description</i>
AOM	Acousto-optic modulator
AOPDF	Acousto-optic programmable dispersive filter
BEC	Bose-Einstein condensate
BBO	$\beta$ -barium borate
CEM	Channel electron multiplier
CCD	Charge-coupled device
CPA	Chirped pulse amplification
cw	Continuous wave
Dark SPOT	Dark spontaneous-force optical trap
ECDL	External-cavity diode laser
FWHM	Full width at half maximum
MCP	Multi-channel plate
MOT	Magneto-optical trap
NOPA	Non-collinear optical parametric amplifier
PZT	Piezo-electric transducer
REMPI	Resonantly enhanced multiphoton ionization
SFG	Sum-frequency generation
SHG	Second-harmonic generation
SPIDER	Spectral phase interferometry for direct electric-field reconstruction
STIRAP	Stimulated Raman adiabatic passage
Ti:sapphire	Titanium-sapphire
TOF	Time-of-flight



# Contents

<b>List of Figures</b>	<b>xiii</b>
<b>List of Tables</b>	<b>xvii</b>
<b>1 Introduction</b>	<b>1</b>
1.1 Thesis outline . . . . .	4
1.2 Author’s contribution . . . . .	7
<b>2 Techniques for cold molecules</b>	<b>9</b>
2.1 A physical model for diatomic molecules . . . . .	10
2.1.1 The Born–Oppenheimer approximation . . . . .	11
2.1.2 Hund’s coupling cases . . . . .	14
2.1.3 Long-range asymptotic behaviour . . . . .	16
2.1.4 The Franck–Condon principle for vibronic transitions . . . . .	20
2.1.5 Scattering theory . . . . .	22
2.2 Direct cooling techniques . . . . .	27
2.3 Indirect cooling techniques . . . . .	29

---

2.3.1	Feshbach resonances . . . . .	29
2.3.2	Continuous-wave photoassociation . . . . .	33
2.3.3	Incoherent optical cycling . . . . .	36
2.3.4	STIRAP . . . . .	39
2.3.5	Ultrafast photoassociation . . . . .	40
2.4	Purity considerations . . . . .	46
2.5	Summary . . . . .	48
<b>3</b>	<b>Quantum control</b>	<b>51</b>
3.1	Introduction to quantum control . . . . .	52
3.2	Closed-loop control . . . . .	55
3.3	Control of ultrafast photoassociation . . . . .	55
3.4	Summary . . . . .	57
<b>4</b>	<b>Experimental apparatus</b>	<b>59</b>
4.1	Choice of species . . . . .	61
4.2	Magneto-optical trap . . . . .	62
4.2.1	Modifications . . . . .	68
4.3	Pulsed laser systems . . . . .	77
4.3.1	Modifications . . . . .	78
4.4	Detection scheme . . . . .	82
4.4.1	Modifications . . . . .	83
4.5	Signal processing . . . . .	87

---

4.5.1	Modifications . . . . .	88
4.6	Summary . . . . .	93
<b>5</b>	<b>Quenching of ground-state molecules</b>	<b>95</b>
5.1	Detection scheme . . . . .	97
5.2	Ground-state quenching with amplified ultrafast pulses . . . . .	100
5.3	Quenching with chirped pulses . . . . .	101
5.4	Summary . . . . .	103
<b>6</b>	<b>Pump-probe study of excited-state molecules</b>	<b>105</b>
6.1	Experimental method . . . . .	107
6.2	Numerical pump-probe simulations . . . . .	111
6.2.1	Excited-state population densities . . . . .	112
6.2.2	Ionization signal simulations . . . . .	114
6.3	Rubidium pump-probe dynamics . . . . .	116
6.4	Summary . . . . .	121
<b>7</b>	<b>Characterization of the initial state</b>	<b>123</b>
7.1	Bound and unbound initial states . . . . .	126
7.2	Background molecule spectroscopy . . . . .	127
7.2.1	Bound excited-state dimers . . . . .	133
7.3	Summary . . . . .	140
<b>8</b>	<b>Conclusion and outlook</b>	<b>143</b>

---

8.1 Outlook . . . . .	147
<b>A Rubidium: atomic and molecular data</b>	<b>151</b>
A.1 Atomic data . . . . .	151
A.2 Molecular potentials . . . . .	155
A.3 Two-photon ionization wavelengths . . . . .	155
<b>B MOT characterization</b>	<b>159</b>
B.1 MOT number characterization . . . . .	159
B.2 MOT temperature characterization . . . . .	161
<b>Bibliography</b>	<b>163</b>

# List of Figures

2.1	Vibrational eigenstates within an adiabatic Born–Oppenheimer representation of the $\text{Rb}_2$ ground singlet electronic potential. . . . .	13
2.2	Vector diagrams illustrating the angular momentum coupling for Hund’s cases (a) and (c). . . . .	15
2.3	An illustration of the impact of the Franck–Condon factors for transitions from the ground to first excited singlet state of $\text{Rb}_2$ . . . . .	21
2.4	An illustration of the impact of the centrifugal barrier term on the long-range ground-state potential for a pair of colliding rubidium atoms. . . . .	23
2.5	The modification of the scattering length by a Feshbach resonance with a near-resonant bound state within a closed channel. . . . .	30
2.6	A schematic illustration of the cw photoassociation process. . . . .	32
2.7	The incoherent optical cycling scheme of Viteau <i>et al.</i> . . . . .	36
2.8	STIRAP as a tool for the formation of deeply bound molecules. . . . .	39
2.9	A schematic illustration of broadband photoassociation. . . . .	42
3.1	The principle of closed-loop control. . . . .	54

---

4.1	The hyperfine splitting of the Rb $D_2$ line and the trapping and re-pumping transitions. . . . .	63
4.2	A schematic diagram of the MOT chamber layout. . . . .	67
4.3	A schematic diagram of the slave laser system layout. . . . .	70
4.4	Simulations of the dynamics of atoms captured in the MOT. . . . .	74
4.5	Spectral and temporal form of the ultrafast laser pulses. . . . .	79
4.6	The TOF detection scheme. . . . .	82
4.7	Typical TOF traces for the pump-probe experiment obtained with the CEM detector, with and without amplification. . . . .	84
4.8	Typical TOF traces for the pump-probe experiment obtained with the MCP detector, with and without amplification. . . . .	86
4.9	The two approaches to a background-compensated molecular signal measurement using the boxcar integrators. . . . .	89
4.10	A typical dependence of the molecular signal size on the NOPA probe laser power. . . . .	92
5.1	The REMPI ground-state detection pathway. . . . .	98
5.2	Molecular ion signal versus CPA pulse fluence, together with an exponential fit. . . . .	99
5.3	The impact of a linearly chirped ultrafast pulse on the suppression of the ground-state molecular ion signal. . . . .	102
6.1	A schematic of the pump-probe experiment. . . . .	108

---

6.2	Layout and timing of the pump-probe experiment. . . . .	109
6.3	Simulations of the time- and position-dependent excited-state population density induced by the pump pulse. . . . .	113
6.4	Simulations of the molecular ion signal. . . . .	117
6.5	Typical atomic and molecular ion signals as a function of pump-probe delay, together with simulations. . . . .	118
7.1	The impact of the initial state on the excited-state dynamics. . . . .	124
7.2	The mechanism for the preparation of a background molecule population by MOT laser photoassociation. . . . .	127
7.3	A schematic of the initial-state characterization experiment. . . . .	128
7.4	A spectroscopic measurement of the initial state. . . . .	130
7.5	The fractional occupation of the $a^3\Sigma_u^+$ vibrational states populated through MOT photoassociation. . . . .	132
7.6	Normalized atomic and molecular ion signals at a fixed pump-probe delay versus detuning of the pump-pulse spectral cut. . . . .	134
7.7	Normalized calculations of the excited-state population transfer induced by the pump pulse versus spectral-cut detuning, together with the experimental signal and an optimized theoretical fit. . . . .	136
7.8	The population distributions of both the background molecules and a scattering state, together with an analytical best fit of the population distribution that contributes to the pump-probe signal. . . . .	139

---

A.1	Rb <sub>2</sub> molecular potentials asymptotic to a $5S+5P$ atom pair, together with the ground triplet and singlet potentials and the ground Rb <sub>2</sub> <sup>+</sup> potential. . . . .	153
A.2	As per the previous figure but for the case of the $5S + 4D$ potential manifold. . . . .	154
A.3	Two-photon ionization wavelengths from the ground singlet and triplet potentials via an intermediate potential within the $5S + 5P$ manifold.	157
A.4	Two-photon ionization wavelengths from the ground singlet and triplet potentials via an intermediate potential within the $5S + 4D$ manifold.	158
B.1	A release-and-recapture measurement of the MOT temperature. . . .	162

# List of Tables

7.1	Analytical models applied to the initial population distribution. . . .	137
A.1	Properties of the isotopes of rubidium. . . . .	152
A.2	Rubidium energy levels with fine structure. . . . .	152
B.1	Typical MOT experimental parameters. . . . .	161



# Chapter 1

## Introduction

*At the beginning of his struggle, the Warrior of Light stated: 'I have dreams.'*

The development of laser-cooling techniques for the formation of cold, trapped atoms represents one of the most significant scientific advances of recent decades. Such pioneering techniques as optical molasses, magneto-optical trapping and optical lattices have since become cornerstones of laboratory experiments worldwide [2-4]. These techniques have advanced experimental low-temperature science past the sub-millikelvin barrier.

Yet this new regime has offered more cardinal benefits than an increment in the state of the art. At these ultracold temperatures, collisions that were dominated by incoherent thermal interactions at room temperature become coherent quantum mechanical events. These low-energy interactions are mediated by interatomic forces that extend to hundreds of Bohr radii, and the de Broglie wavelength of the colliding

atoms are of the same order. Furthermore, the characteristic long-range interaction energies are commensurate with the shifts that may be induced by optical and magnetic fields, offering the possibility of external control.

The emergence of the study of ultracold physics has catalyzed advances in such areas as ultracold atomic collisions, atomic fountains, atomic clocks and high precision spectroscopy [5, 6]. Furthermore, the achievement of sub-microkelvin temperatures with evaporative cooling has culminated in the macroscopic quantum degeneracy of the Bose-Einstein condensate (BEC) [7, 8].

The fecundity of the field of cold atoms has inspired interest in the generation of ultracold molecules in prescribed low-energy internal states. Prospects ranging from precision molecular spectroscopy [9] to the coherent control of chemical reactions and new techniques for quantum computing [10, 11] would be offered. Proposals have advocated the application of ultracold molecules to the search for the permanent electric dipole moment of the electron [12].

Atomic cooling techniques, however, cannot be generalized even to simple diatomic molecules due to the lack of availability of a closed-loop cooling cycle within the rich molecular internal energy level structure: population would inextricably be driven into a range of vibrational and rotational levels that were dark to the cooling cycle before significant cooling could be accomplished. Various alternative direct cooling techniques have been developed that stabilize hot molecules efficiently into their lowest vibrational levels; however, these are unable to cool their translational motion significantly below the millikelvin regime [13, 14]. In order to reach mi-

crokelvin or nanokelvin temperatures, it is necessary instead to associate ultracold atoms via approaches such as photoassociation [15, 16], the manipulation of Feshbach resonances [17, 18], or three-body collisions [19]. These processes, however, favour the formation of ultracold but vibrationally excited molecules.

These indirect approaches form the basis of some recent techniques that seek to transfer translationally cold but vibrationally excited molecules into more deeply bound states. An incoherent broadband cycling scheme specific to caesium has been used to transfer the vibrational distribution of photoassociated dimers to a predetermined state in the ground potential [20]. Stimulated Raman adiabatic passage (STIRAP) has been applied to transfer Feshbach molecules of various species to lower-lying states [21–24]. This transfer process is coherent and efficient but requires phase-stabilized control lasers that are specific to the vibrational spectroscopy of the system.

A complementary quantum control strategy to those outlined above is the coherent control [25, 26] of the photoassociation process using broadband tailored optical fields. The broad bandwidth of an ultrafast pulse from a modelocked Ti:sapphire laser is a promising tool for the manipulation of typical diatomic molecules, with significant spectral intensity concentrated at ground- to excited-state atomic transitions. The Franck–Condon principle restricts the useable spectral bandwidth for atom-pair association (thus motivating the future development of picosecond pulse generation and shaping technologies); however, the surplus spectral intensity is nonetheless resonant with bound-bound molecular transitions at a range of inter-

nuclear separations. These pulses therefore offer flexibility for the conception of a multi-step protocol for wavepacket association and transfer.

An ultracold scattering event may therefore be steered towards a target state through a variety of vibronic pathways, with phase and amplitude shaping of the excitation pulse offering control over the system Hamiltonian via the dipole interaction. Furthermore, closed-loop feedback may be applied to the choice of pulse shape in order to identify an empirical optimum. The generality of this approach is thus limited merely by the frequency and bandwidth of the laser system and shaping capabilities, rather than any requirement for precise spectroscopic knowledge.

Early experiments investigating ultrafast photoassociation processes revealed coherent mechanisms that resulted in a *reduction* of the background molecular population [27, 28]. The desire to understand this quenching and *create* molecules has impelled attempts to learn about the dynamics induced within the excited state following photoassociation, as well as to characterize the initial state interacting with the broadband pulse and understand its influence on the experimental outcome. The merging of the realms of the ultrafast and ultracold is thus an enticing prospect, and will be the subject of this thesis.

## 1.1 Thesis outline

In Chapter 2, some key concepts relating to the physical description of the formation of ultracold diatomic molecules by photoassociation are described. Both direct and indirect approaches to the generation of cold molecules in prescribed internal

---

states are summarized, with emphasis on the indirect techniques that offer more promise for the ultracold regime. The application of ultrafast pulses for ultrafast photoassociation is introduced and the merits of this approach discussed.

Chapter 3 concerns the diverse range of techniques that apply control fields to manipulate quantum states of matter and fall within the broad remit of quantum control. The value of closed-loop algorithms for broadband control schemes is discussed. The chapter concludes with a discussion of the specific relevance of these techniques to the ultrafast photoassociation of ultracold atoms.

Chapter 4 describes the experimental apparatus. An obstacle to the development of the excited-state experiments described in Chapters 6 and 7 was presented by certain significant limitations of the existing apparatus — particularly concerning stability and signal-to-noise levels. The steps taken to address these problems are described.

Chapter 5 discusses preliminary experiments to investigate the action of high-energy sub-picosecond pulses on the background ground-state molecular population, in extension of the work of Brown *et al.* [27]. An intensity-dependent quenching of population is observed, with the background signal decreasing exponentially with pulse fluence. No impact is detected of a linear chirp on the quenching rate, though signal-to-noise levels of around 15%, which limit experimental sensitivity, motivate the improvements to the apparatus detailed in Chapter 4.

In Chapter 6, the results of a pump-probe experiment to measure the excited-state dynamics that follow broadband photoassociation are presented. An ultrafast

pump pulse promotes atom pairs into bound states within an excited potential manifold. This population is allowed to evolve freely for a controllable time delay before being ionized by a second ultrafast pulse. The molecular ion yield is monitored as a function of pump-probe delay, and the results are compared to numerical simulations. The results indicate evidence of excited-state population; however, wavepacket dynamics are not discernible. This is discussed within the context of both the selectivity of the probe pulse and the initial state of the atom pairs.

Chapter 7 addresses the question of the initial state directly. In addition to the cold atoms, the setup is known to contain a background population of pre-associated molecules. These background molecules are alternative candidates to unbound scattering atom pairs for interaction with the pump pulse. They would be expected to undergo different characteristic excited-state dynamics due to their shorter range compared to a scattering state. A spectroscopic measurement of the bound initial-state occupation is presented, and the result allows the identification of the background formation mechanism. The pump-probe experiment is revisited, with the atomic and molecular ion signals compared as a function of the pump-pulse detuning from atomic resonance. The persistence of the molecular signal at detunings that deplete the atomic signal confirms the formation of bound excited-state dimers. Furthermore, a quantitative interpretation allows the initial population distribution to be derived. The result is consistent with the association of free atom pairs — rather than background molecules — by the pump pulse.

In Chapter 8, the thesis concludes with an evaluation of the results presented

within, together with their context and relevance to the field. The direction of future research is proposed, with emphasis placed on the lower temperatures and higher densities that would enhance efficiency and increase signal size.

## 1.2 Author's contribution

The experiments described within this thesis were conducted in association with various colleagues within the research group of Prof. Ian Walmsley at the University of Oxford. The ground-state results of Chapter 5, together with the modifications to the ultrafast system discussed in Chapter 4, were obtained under the guidance of a post-doctoral researcher (Antoine Monmayrant) and a senior D. Phil. student (Alex Dicks). Following the departure of these colleagues, a new post-doctoral researcher (Jovana Petrovic) and D. Phil. student (Duncan England) joined the experiment. The remainder of the apparatus modifications, together with the excited-state studies (Chapters 6 and 7), were carried out in collaboration with these colleagues. Another student (Melissa Friedman) also worked on the design of the new pulse shaper. Meanwhile the theoretical simulations of excited-state dynamics (Chapter 6) and the initial-state distribution (Chapter 7) were conducted by Hugo Martay.



## Chapter 2

# Techniques for cold molecules

*A Warrior of Light shares with others what he knows of the path.*

In this chapter, a theoretical framework for the description and study of diatomic molecules will be introduced. Some important approximations that counter the intractability of the Schrödinger equation for a diatomic molecule will be described. The Born–Oppenheimer approximation, which allows the separation of electronic and nuclear motion, will be outlined. A description will be given of both the long- and short-range asymptotic behaviour of the molecular potentials, and the quantities that serve as good and bad quantum numbers within these regimes will be presented. The Franck–Condon principle, which governs the probability of vibrational transitions, will be derived. Some scattering theory for the description of cold collisions will be introduced.

Progress in both direct and indirect molecule cooling techniques will be summarized and their respective merits compared. Indirect techniques currently offer the best prospects for the formation of translationally ultracold molecules in deeply bound internal states. The state of the art of such techniques will be outlined, and the concept of ultrafast photoassociation — the focus of this thesis — will be presented.

## 2.1 A physical model for diatomic molecules

The tractability of the Schrödinger equation,

$$\frac{-\hbar^2}{2m}\nabla^2\psi + V(R)\psi = E\psi, \quad (2.1)$$

for the hydrogen atom [29] with a Coulomb potential,  $V(R)$ , makes this system an elegant illustration of the laws of quantum mechanics. More complex systems, however, possess a Hamiltonian including interaction terms that must be summed over all the electrons; these systems are not, in general, separable. Instead the central field approximation and successive perturbations may be applied to the Hamiltonian so as to facilitate the inference of some physical meaning.

Likewise the terms in the molecular Hamiltonian that specify the additional vibrational and rotational degrees of freedom introduce an extra richness to molecular spectra. Inter-nuclei effects and the coupling of the nuclear and electronic degrees of freedom complicate the complete physical analysis of the molecule; numerical so-

lution of the energy-level structure is typically required. There are, however, several powerful approximations that can be made in order to illuminate the problem. The topic is treated thoroughly in such textbooks as Herzberg [30] and Atkins [31]; some important results are summarized below.

### 2.1.1 The Born–Oppenheimer approximation

The Schrödinger equation for even a simple diatomic molecule is analytically intractable due to the number of particles involved. A useful approximation notes that the electronic mass is much less than the nuclear mass of the constituent atoms. Given further that the electrons and nuclei will experience electrostatic forces of a similar magnitude, the timescale for electronic motion will consequently be much shorter and the electron may be considered to respond to the motion of the nuclei instantaneously. This is the basis of the Born–Oppenheimer approximation.

Under the condition that the electronic wavefunction varies slowly with respect to internuclear separation (see Section IV.1 of Herzberg [30]), it is possible to separate the system eigenstates into a product of its nuclear and electronic components,

$$|\psi(R, \mathbf{r})\rangle = |\psi_{\text{N}}^{n,p}(R)\rangle |\psi_{\text{e}}^p(R, \mathbf{r})\rangle, \quad (2.2)$$

where  $|\psi_{\text{N}}^{n,p}(R)\rangle$  is the  $n^{\text{th}}$  nuclear eigenstate within the  $p^{\text{th}}$  electronic eigenstate,  $|\psi_{\text{e}}^p(R, \mathbf{r})\rangle$ , and  $R$  and  $\mathbf{r}$  are<sup>1</sup> the internuclear separation and the electronic coordinates. (A convention that subscript indices distinguish electronic components whilst

---

<sup>1</sup>...not to mention a bit of a mouthful.

superscript indices denote the nuclear and electronic eigenstates is adopted.)

The Schrödinger equation can therefore be solved parametrically for the electronic motion at fixed internuclear coordinate  $R$  under the Hamiltonian  $\hat{H}_e(R, \mathbf{r})$ :

$$\hat{H}_e(R, \mathbf{r})|\psi_e^p(R, \mathbf{r})\rangle = U^p(R)|\psi_e^p(R, \mathbf{r})\rangle. \quad (2.3)$$

The electronic energy eigenvalues,  $U^p(R)$ , trace out a series of curves that vary with the internuclear separation. Together with the electrostatic repulsion of the two nuclei, these form the total effective potential energy of the two nuclei,

$$V^p(R) = U^p(R) + \frac{Z_1 Z_2 e^2}{4\pi\epsilon_0 R}, \quad (2.4)$$

where  $Z_1$  and  $Z_2$  are the atomic numbers of the two nuclei,  $e$  is the electronic charge, and  $\epsilon_0$  is the free-space permittivity. Subsequently the nuclear motion under these electronic potentials can also be calculated:

$$\hat{H}_N^p(R)|\psi_N^{n,p}(R)\rangle = E_N^{n,p}(R)|\psi_N^{n,p}(R)\rangle, \quad (2.5)$$

where the nuclear Hamiltonian,  $\hat{H}_N^p(R) = \hat{T}_N(R) + \hat{V}^p(R)$ , includes kinetic and potential energy terms.

Thus the Born–Oppenheimer approximation allows the construction of a set of electronic potential energy surfaces,  $V^p(R)$ , that govern the motion of the nuclei. These ‘adiabatic Born–Oppenheimer potentials’ are valid at close range ( $R \leq 30 a_0$ )

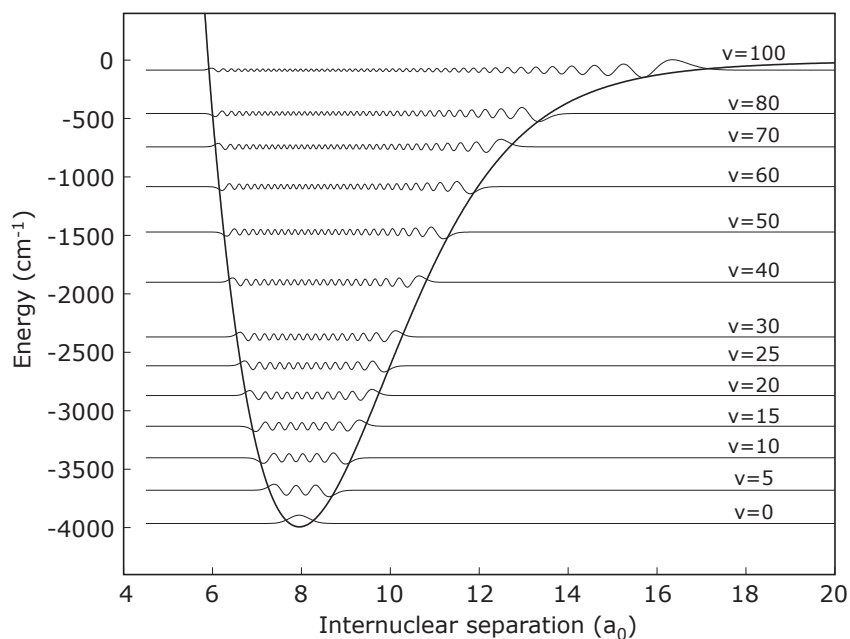


**Figure 2.1** Vibrational eigenstates within an adiabatic Born–Oppenheimer representation of the Rb<sub>2</sub> ground singlet electronic potential. The anharmonicity of the potential results in the vibrational state energy spacing becoming smaller and the wavefunctions more asymmetric at larger  $v$ .

[32]. At longer range, where the electron clouds of the two atoms do not significantly overlap, the molecular potentials may instead be formulated using the product of the two atomic wavefunctions to describe the molecular wavefunction. This is described in more detail in Section 2.1.3.

Calculation of these electronic potentials is a complex task; however, they do obey certain useful approximations under certain regimes of  $R$ . For  $R$  close to equilibrium, the anharmonic oscillator [30] offers a good approximation with regard to the vibrational levels. For small anharmonicities, the solutions to the harmonic

oscillator  $E_v^{\text{har}} = \hbar\omega_e \left(v + \frac{1}{2}\right)$  are modified:

$$E_v^{\text{anhar}} = \hbar\omega_e \left[ \left(v + \frac{1}{2}\right) - x_e \left(v + \frac{1}{2}\right)^2 + y_e \left(v + \frac{1}{2}\right)^3 + \dots \right] \quad (2.6)$$

where  $y_e \ll x_e \ll 1$ . The vibrational levels in the molecular potentials become more tightly spaced at larger  $v$ . Various eigenstates within the ground-state singlet potential of  $\text{Rb}_2$  are presented in Fig. 2.1; the anharmonicity of the potential may be observed in the form of a decreasing eigenstate separation and increasing asymmetry with increasing  $v$ .

### 2.1.2 Hund's coupling cases

The orbital angular momentum of electrons moving in the isotropic Coulomb field of a nucleus is a constant of the motion, provided that electron-electron interactions and spin-orbit coupling may be neglected. The operator for the total electronic orbital angular momentum commutes with the Hamiltonian, and thus takes a well defined eigenvalue,  $L$ , for an energy eigenstate of the system. For a diatomic molecule, however, the internuclear electric field may couple the orbital angular momentum to the internuclear axis. If this coupling is sufficiently strong compared to the spin-orbit interaction or the coupling to the nuclear rotation,  $N$ , then only the projection,  $\Lambda = L \cdot \hat{\mathbf{k}}$ , upon the internuclear axis,  $\hat{\mathbf{k}}$ , becomes a good quantum number.

The relative strengths of the couplings to the internuclear axis, the spin-orbit interaction, and the coupling to the nuclear rotation determine which quantities may be deemed 'good quantum numbers'. Different regimes, known as Hund's coupling

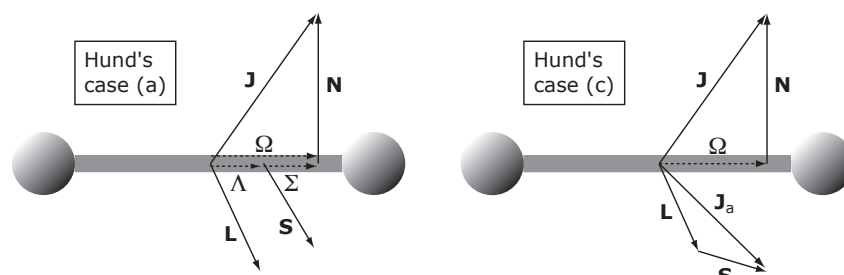


**Figure 2.2** Vector diagrams illustrating the angular momentum coupling for Hund's cases (a) and (c).

cases, may be identified according to this hierarchy. For the ultracold collisions pertinent to this thesis, the effects of nuclear rotation may be ignored, as discussed in Section 2.1.5; thus the following discussions are confined to Hund's cases (a) and (c), which are introduced below (and summarized in Fig. 2.2).

**Hund's case (a).** In Hund's case (a), the strongest interaction is the coupling of the orbital angular momentum,  $\mathbf{L}$ , to the internuclear axis. As a result,  $\Lambda$  is a good quantum number. For  $\Lambda \neq 0$  states, the spin-orbit interaction couples the total electron spin,  $\mathbf{S}$ , to the orbital angular momentum and hence to the molecular axis; consequently the projection  $\Sigma$  of  $\mathbf{S}$  onto this axis is also a good quantum number. The resultant vector sum of  $(\Lambda + \Sigma)\hat{\mathbf{k}}$  and  $\mathbf{N}$  then forms the total angular momentum,  $\mathbf{J}$ , with projection  $\Omega = \mathbf{J} \cdot \hat{\mathbf{k}} = \Lambda + \Sigma$  onto the internuclear axis. The molecular state is denoted  $^{2S+1}|\Lambda|_{g/u}^{\pm}$  in accordance with these conserved quantum numbers, where the *gerade* (*g*) or *ungerade* (*u*) parity describes the inversion symmetry through the centre of mass, and  $\pm$  accounts for the reflection symmetry of the spatial wavefunction through a plane containing the internuclear axis. Furthermore,

the electronic states have historically been labelled as  $X, A, B, \dots$  (for the singlet states) and  $a, b, c, \dots$  (for the triplet states) in ascending energy (see Fig A.1).

**Hund’s case (c).** If the spin-orbit interaction is stronger than the individual coupling of  $\mathbf{L}$  and  $\mathbf{S}$  to the internuclear axis, then  $\Omega = (\mathbf{L} + \mathbf{S}) \cdot \hat{\mathbf{k}} = \mathbf{J}_a \cdot \hat{\mathbf{k}}$  remains a good quantum number though  $\Lambda$  and  $\Sigma$  individually become ill defined. The subsequent coupling of  $\Omega \hat{\mathbf{k}}$  and  $\mathbf{N}$  forms the total angular momentum,  $\mathbf{J}$ . Since  $\Lambda$  and  $\Sigma$  are no longer individually good quantum numbers, the molecular term symbol  $|\Omega|_{g/u}^{\pm}$  is employed (where  $\pm$  indicates the symmetry of the total wavefunction).

In the context of this work, the Hund’s case (a) basis is appropriate for the description of close-range ( $R \leq 20 a_0$ ) dimers, whereas Hund’s case (c) may be applied at longer range.

### 2.1.3 Long-range asymptotic behaviour

At the short-range internuclear separations described above, the electron clouds of the two atoms overlap significantly, with exchange interactions and chemical bonding becoming significant. At long range, however, this is not the case, and the molecular wavefunction is well described by the product of the atomic wavefunctions. Likewise the properties of these long-range molecules (termed “physicists’ molecules” by Jones *et al.* [32]) may be related asymptotically to those of the constituent atoms. Under these circumstances, it is convenient to expand the asymptotic form of the potential curves as a power series in  $1/R$ . The leading order term is determined by the dominant long-range interaction mechanism for a pair of atoms in their given

electronic states.

Outside the range of the interactions mediating the form of the potential well, the spin-orbit coupling becomes more significant, and it becomes necessary to consider a term proportional to  $\mathbf{L}\cdot\mathbf{S}$ . As a result of this coupling,  $\Lambda$  and  $S$  are no longer good quantum numbers; instead, it is necessary to consider the projection  $\Omega$  of the total angular momentum  $\mathbf{J} = \mathbf{L} + \mathbf{S}$  upon the internuclear axis.

As well as spin-orbit interactions, it is necessary to consider the role played by dipole-dipole interactions between the two atoms. The electric potential of a classical dipole  $\boldsymbol{\mu}$  is

$$V(\mathbf{R}) = \frac{\boldsymbol{\mu}\cdot\mathbf{R}}{4\pi\epsilon_0 R^3}, \quad (2.7)$$

where  $R = |\mathbf{R}|$  is the distance from the dipole, and is taken to be large compared to the dipole itself. The dipole electric field is therefore

$$\mathbf{E} = -\nabla V = \frac{3(\boldsymbol{\mu}\cdot\hat{\mathbf{R}})\hat{\mathbf{R}} - \boldsymbol{\mu}}{4\pi\epsilon_0 R^3}, \quad (2.8)$$

where  $\hat{\mathbf{R}}$  is a unit vector in the direction of  $\mathbf{R}$ . Thus the dipole-dipole interaction energy is

$$V_{\text{dd}} = -\boldsymbol{\mu}_2\cdot\mathbf{E}_1 = \frac{\boldsymbol{\mu}_1\cdot\boldsymbol{\mu}_2 - 3(\boldsymbol{\mu}_1\cdot\hat{\mathbf{R}})(\boldsymbol{\mu}_2\cdot\hat{\mathbf{R}})}{4\pi\epsilon_0 R^3}. \quad (2.9)$$

The dipole interaction obeys the selection rule  $\Delta L = \pm 1$  and thus couples  $S$ -state to  $P$ -state atoms and vice versa, but not pairs of atoms of equal  $L$ . Consider a four-level system comprising two atoms that may each occupy either an  $S$  or  $P$  state

such that

$$|\Psi\rangle = c_1|S_1S_2\rangle + c_2|S_1P_2\rangle + c_3|P_1S_2\rangle + c_4|P_1P_2\rangle, \quad (2.10)$$

and is described by the vector  $\begin{pmatrix} c_1 \\ c_2 \\ c_3 \\ c_4 \end{pmatrix}$ . When a perturbation is introduced into the system Hamiltonian due to the dipole coupling  $V_{\text{dd}}$ , it takes the form

$$H = \begin{pmatrix} 0 & 0 & 0 & V_{\text{dd}} \\ 0 & \varepsilon_1 & V_{\text{dd}} & 0 \\ 0 & V_{\text{dd}} & \varepsilon_2 & 0 \\ V_{\text{dd}} & 0 & 0 & \varepsilon_1 + \varepsilon_2 \end{pmatrix}, \quad (2.11)$$

where  $\varepsilon_1$  and  $\varepsilon_2$  denote the unperturbed eigenenergies of the  $P$ -state atoms. Since the dipole interaction separately couples  $|S_1S_2\rangle \leftrightarrow |P_1P_2\rangle$  and  $|S_1P_2\rangle \leftrightarrow |P_1S_2\rangle$ , the perturbed eigenvalues may be treated separately for these two subspaces:

$$\begin{pmatrix} 0 & V_{\text{dd}} \\ V_{\text{dd}} & \varepsilon_1 + \varepsilon_2 \end{pmatrix} \begin{pmatrix} c_1 \\ c_4 \end{pmatrix} = E_{\text{A}} \begin{pmatrix} c_1 \\ c_4 \end{pmatrix} \quad (2.12)$$

$$\begin{pmatrix} \varepsilon_1 & V_{\text{dd}} \\ V_{\text{dd}} & \varepsilon_2 \end{pmatrix} \begin{pmatrix} c_2 \\ c_3 \end{pmatrix} = E_{\text{B}} \begin{pmatrix} c_2 \\ c_3 \end{pmatrix}. \quad (2.13)$$

The perturbed eigenenergies are

$$E_{\text{A}} = \bar{\varepsilon} \pm \sqrt{\bar{\varepsilon}^2 + V_{\text{dd}}^2} \quad (2.14)$$

$$E_{\text{B}} = \bar{\varepsilon} \pm \sqrt{\Delta\varepsilon^2 + V_{\text{dd}}^2}, \quad (2.15)$$

where  $\bar{\varepsilon} = (\varepsilon_1 + \varepsilon_2)/2$  and  $\Delta\varepsilon = (\varepsilon_1 - \varepsilon_2)/2$ . In the limit of  $V_{\text{dd}}^2 \ll \bar{\varepsilon}^2$  and  $V_{\text{dd}}^2 \ll \Delta\varepsilon^2$  this reduces to

$$E_{\text{A}} = \bar{\varepsilon} \pm \left( \bar{\varepsilon} + \frac{V_{\text{dd}}^2}{2\bar{\varepsilon}} \right) \quad (2.16)$$

$$E_{\text{B}} = \bar{\varepsilon} \pm \left( \Delta\varepsilon + \frac{V_{\text{dd}}^2}{2\Delta\varepsilon} \right). \quad (2.17)$$

On the other hand, for the case of an interacting pair of identical atoms where  $\varepsilon_1 = \varepsilon_2$ , Equation 2.15 reduces to

$$E_{\text{B}} = \bar{\varepsilon} \pm V_{\text{dd}}. \quad (2.18)$$

Thus the leading term in the power series expansion for the long-range form of heteronuclear molecular potentials correlating with  $S + S$ ,  $S + P$  and  $P + P$  atoms scales as  $V_{\text{dd}}^2 \sim R^{-6}$  (Equations 2.16, 2.17). This is also the case for homonuclear molecular potentials correlating with  $S + S$  and  $P + P$  atoms. The physical origin of this term is the van der Waals dispersion forces between the two atoms. Though the atoms do not possess a permanent electric dipole moment, density fluctuations in the electron cloud of one atom may nevertheless arise, causing that atom to possess an instantaneous dipole moment. This may, in turn, induce a dipole moment in the partner atom, giving rise to an attractive induced-dipole–induced-dipole interaction between the pair of atoms. An exception to this situation arises for the case of homonuclear molecules with long-range  $S + P$  atomic character, where the leading order term scales instead as  $V_{\text{dd}} \sim R^{-3}$  (Equation 2.18), since the atoms are

resonantly coupled by the dipole-dipole interaction.

#### 2.1.4 The Franck–Condon principle for vibronic transitions

The overall wavefunction of the molecule may be described as the product of nuclear, electronic spatial and electronic spin components:

$$|\Psi\rangle = |\Psi_N\rangle|\Psi_e\rangle|\Psi_S\rangle. \quad (2.19)$$

The probability amplitude for the transition from initial state  $|\Psi\rangle$  to final state  $|\Psi'\rangle$  is thus described by the matrix element

$$P = \langle\Psi'|\boldsymbol{\mu}|\Psi\rangle, \quad (2.20)$$

where the dipole operator  $\boldsymbol{\mu} = \boldsymbol{\mu}_e + \boldsymbol{\mu}_N$  includes components derived from the distributions of both the electrons and the nuclei. The probability amplitude can thus be evaluated as follows:

$$\begin{aligned} P &= \langle\Psi'_N|\Psi_N\rangle\langle\Psi'_e|\boldsymbol{\mu}_e|\Psi_e\rangle\langle\Psi'_S|\Psi_S\rangle + \langle\Psi'_N|\boldsymbol{\mu}_N|\Psi_N\rangle\langle\Psi'_e|\Psi_e\rangle\langle\Psi'_S|\Psi_S\rangle \\ &= \langle\Psi'_N|\Psi_N\rangle\langle\Psi'_e|\boldsymbol{\mu}_e|\Psi_e\rangle\langle\Psi'_S|\Psi_S\rangle \end{aligned} \quad (2.21)$$

for  $\Psi'_e \neq \Psi_e$  since  $\langle\Psi'_e|\Psi_e\rangle = 0$ .

The integrals  $\langle\Psi'_e|\boldsymbol{\mu}_e|\Psi_e\rangle$  and  $\langle\Psi'_S|\Psi_S\rangle$  respectively give rise to the electronic dipole and spin selection rules of the transition. These terms hold the greatest

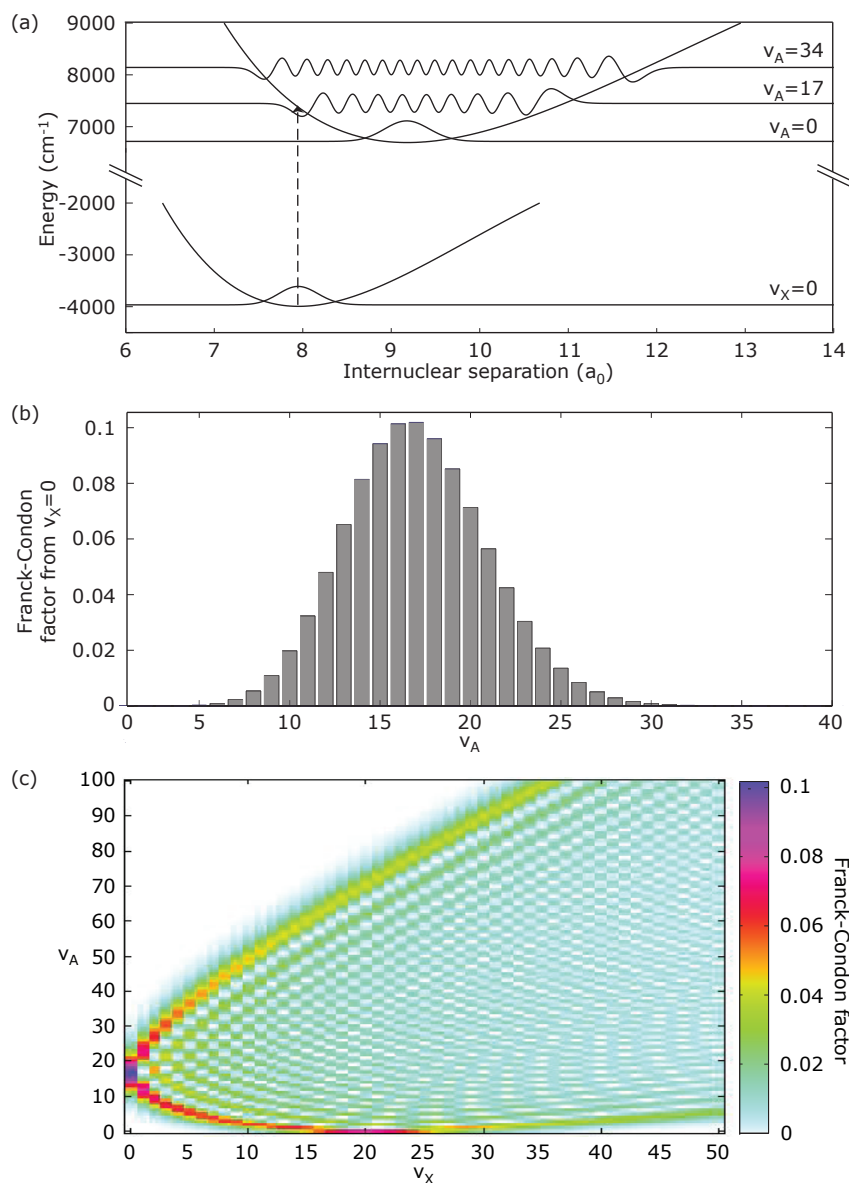


**Figure 2.3** An illustration of the impact of the Franck–Condon factors for transitions from the ground (X) to first excited (A) singlet state of Rb<sub>2</sub>. (a) Selected deeply bound vibrational eigenstates. The transition probability from  $v_X = 0$  is greatest to  $v_A = 17$ , due to the good alignment with the excited-state classical inner turning point. (b) Franck–Condon overlaps  $|\langle \Psi_A | \Psi_X \rangle|^2$  from  $v_X = 0$  to deeply bound excited vibrational states. (c) The Condon parabola showing the Franck–Condon factors between low-lying states within X- and A-potentials. The two branches of the parabola correspond to inner and outer turning-point transitions.

influence over the transition probability; the overlap integral between the initial and final vibrational states,  $\langle \Psi'_N | \Psi_N \rangle$ , contributes a modulation to the probability of a given electronic transition dependent on the vibrational states concerned. The transition probability depends on the square of this overlap integral, known as the Franck–Condon factor, with the Franck–Condon principle dictating that a vibronic transition is rendered more probable by a spatial overlap of the initial and final wavefunction. This principle is depicted in Fig. 2.3 for transitions between deeply bound vibrational states of the ground and first excited singlet states of  $\text{Rb}_2$ .

For increasing degrees of excitation, the probability distributions of vibrational eigenstates become increasingly localized at the classical turning points of the potential. A physical interpretation of the Franck–Condon principle is therefore that vibronic transitions occur ‘vertically’ between these classical turning points (known as the Condon points), such that

$$V'(R_C) - V(R_C) = \hbar\omega. \quad (2.22)$$

### 2.1.5 Scattering theory

This section presents some key results of scattering theory as applied to ultracold collisions and indicates their physical implications. Further details may be found in Chapter 14 of Metcalf and van der Straten [33], Chapter 9 of Pitaevskii and Stringari [34], Chapter 5 of Pethick and Smith [35] or Chapter 13 of Townsend [36].

The de Broglie wavelength of a thermal sample of atoms of momentum  $p$ , mass  $m$

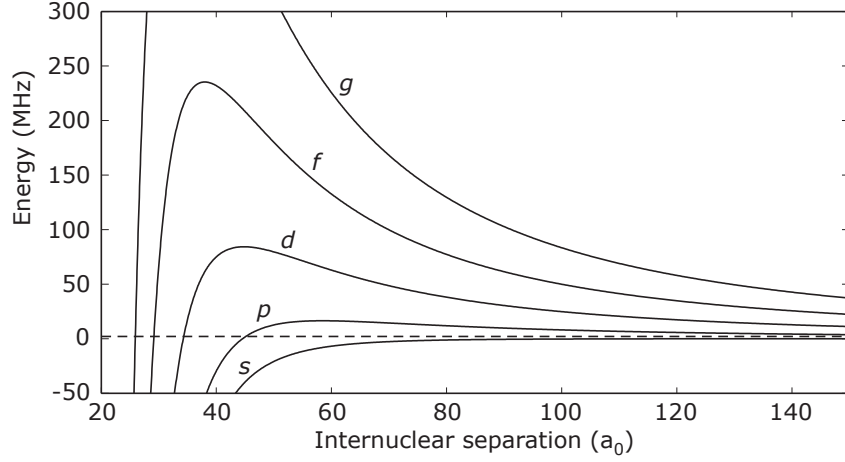


**Figure 2.4** An illustration of the impact of the centrifugal barrier term from Equation 2.24 on the long-range ground-state potential for a pair of colliding rubidium atoms. The height of the centrifugal barrier increases with angular momentum  $l$  ( $l = 0, 1, 2, 3, 4$  are denoted  $s, p, d, f, g$ ). At ultracold temperatures (the dotted line indicates  $100 \mu\text{K}$ ), no  $l \neq 0$  partial waves will penetrate the barrier sufficiently to contribute to the scattering process. This is known as the  $s$ -wave scattering regime.

and temperature  $T$  is  $\lambda_{\text{deB}} = h/p = \frac{h}{\sqrt{3mk_B T}}$ . In the ultracold regime, this begins to exceed the interatomic interaction range (typically  $R_{\text{int}} \lesssim 2000a_0$ ). Thus scattering events become coherent, quantum mechanical processes that are best described using the potential scattering model, whereby the collisional protagonists are treated as structureless hard objects moving in an interaction potential.

The Schrödinger equation for an ultracold scattering atom pair takes the form

$$-\frac{\hbar^2}{2\mu}\nabla^2\Psi(R) + V(R) + \frac{\hbar^2 l(l+1)}{2\mu R^2} = E\Psi(R), \quad (2.23)$$

where  $V(R)$  is the scattering potential,  $l$  is the angular momentum quantum number for the relative motion of the two colliding atoms, and  $\mu$  is their reduced mass. At

large internuclear separation,  $V(R)$  can be described by the leading non-zero term in a power series expansion in  $1/R$  (see Section 2.1.3). For two ground-state  $S$  atoms, this is the  $V(R) = -C_6/R^6$  van der Waals interaction term, where  $C_6$  is the relevant dispersion coefficient. The interaction potential can therefore be treated at long range as the leading term in this power series augmented by a centrifugal term dependent on angular momentum:

$$V_{\text{eff}}(R) = -\frac{C_6}{R^6} + \frac{\hbar^2 l(l+1)}{2\mu R^2}. \quad (2.24)$$

The  $\hbar^2 l(l+1)/2\mu R^2$  angular momentum term acts as a centrifugal barrier to the incoming wave that increases in height with  $l$ , as demonstrated in Fig. 2.4. Contributions to the scattering process are therefore suppressed at high angular momentum. Due to the dependence of  $V(R)$  on angular momentum, it is convenient to consider the sum of the contributions to the scattering process of a series of partial waves with well defined angular momenta. In the ultracold regime, characterized by sub-millikelvin temperatures, bosonic collisions (such as the Rb—Rb interactions considered within this work) are of sufficiently low energy that all  $l \neq 0$  partial waves are suppressed; thus  $s$ -wave scattering is the dominant channel. Fermionic  $s$ -wave interactions, by contrast, are prohibited by the Pauli exclusion principle, with  $p$ -wave interactions consequently providing the dominant contribution.

At small internuclear separations,  $V(R)$  becomes significant with respect to other terms in the Schrödinger equation, and complicates the solution. At large  $R$ , how-

ever, this term can be neglected, and the result tends towards an oscillating free space solution.<sup>2</sup> Beyond the influence of the scattering potential, the asymptotic long range form of the  $s$ -wave scattering wavefunction is described by the sum of an incident plane wave in the relative coordinate system and a scattered spherical wave,

$$\Psi(R, \theta) \xrightarrow{R \rightarrow \infty} e^{ikR} + f(\theta) \frac{\sin(kR - \delta)}{R}, \quad (2.25)$$

where the scattering amplitude,  $f(\theta)$ , is a function of the scattering angle with respect to the internuclear axis, and is symmetric about this axis, and  $k$  is the wavevector.

The origin of the phase shift  $\delta$  stems from boundary condition constraints on the wavefunction at short range. In the absence of a short-range potential,  $\delta$  would be zero due to the requirement that the wavefunction remains finite as  $R \rightarrow 0$ . In the presence of the scattering potential, however, the asymptotic wavefunction must instead be matched to the close-range wavefunction within the potential. This asymptotic wavefunction will, in general, be phase-shifted with respect to the cor-

---

<sup>2</sup>Such a solution must satisfy Equation 2.23 for

$$V(R) + \frac{\hbar^2 l(l+1)}{2\mu R^2} \xrightarrow{R \rightarrow \infty} 0,$$

and the standard approach is to seek solutions of the form  $\Psi(R) = \Phi(R)/R$ . Under this substitution, the free-space Schrödinger equation reduces to a one-dimensional form:

$$-\frac{\hbar^2}{2\mu R^2} \frac{d^2}{dR^2} \Psi(R) = E\Psi(R).$$

This substitution is of physical significance since the probability of finding the two nuclei separated by  $R$  is given by the integral

$$\int |\Psi(R)|^2 4\pi R^2 dR \propto \int |\Phi(R)|^2 dR.$$

responding free space solution in the absence of any potential by an amount whose magnitude is affected by the strength of the potential. In this way the effect of the scattering potential can be described by a single parameter in the form of the phase accrued by the long-range scattering wavefunction.

It is convenient to expand the scattering amplitude as a sum over the Legendre polynomials,<sup>3</sup>

$$f(\theta) = \sum_{l=0}^{\infty} (2l+1) a_l(k) P_l(\cos \theta), \quad (2.26)$$

where  $l$  corresponds to the angular momentum quantum number for the relative motion of the two particles and the coefficients  $a_l(k)$  can be shown to take the form (see Townsend, Chapter 9 [36])

$$a_l(k) = \frac{e^{i\delta_l} \sin \delta_l}{k}. \quad (2.27)$$

Under the  $s$ -wave scattering regime, only the  $l = 0$  term from the summation

---

<sup>3</sup>The motivation for choosing this particular orthogonal basis set for the decomposition of the scattering amplitude is as follows. The eigenvalue equation of the orbital angular momentum operator,

$$\hat{\mathbf{L}}^2 \chi(\theta, \phi) = -\hbar^2 \left\{ \frac{1}{\sin \theta} \frac{\partial}{\partial \theta} \left( \sin \theta \frac{\partial}{\partial \theta} \right) + \frac{1}{\sin^2 \theta} \frac{\partial^2}{\partial \phi^2} \right\} \chi(\theta, \phi) = \lambda \chi(\theta, \phi),$$

may be solved via a separation of variables  $\chi(\theta, \phi) = \Theta(\theta)\Phi(\phi)$ , giving rise to an eigenvalue equation in  $\Theta(\theta)$  taking the form

$$-\hbar^2 \left\{ \frac{1}{\sin \theta} \frac{\partial}{\partial \theta} \left( \sin \theta \frac{\partial}{\partial \theta} \right) \right\} \Theta(\theta) = \lambda \Theta(\theta)$$

(see, for example, Foot, Chapter 2 [37] or Townsend, Chapter 9 [36]). Under the substitution  $\xi = \cos \theta$  and  $\lambda = l(l+1)$  this reduces to the Legendre equation (see, for example, Boas, Chapter 12 [38]),

$$(1 - \xi^2) \frac{\partial^2 \Theta(\theta)}{\partial \xi^2} - 2\xi \frac{\partial \Theta(\theta)}{\partial \xi} + l(l+1)\Theta(\theta) = 0,$$

such that the solutions are the Legendre polynomials  $P_l(\cos \theta)$  for angular momentum quantum number  $l$ . Thus this basis set describes the scattering amplitude in terms of a summation index that corresponds to the angular momentum quantum number.

in Equation 2.26 needs consideration. Furthermore all phase shifts become small as  $k$  approaches zero and  $P_0(\cos \theta) = 1$  [35]. The scattering amplitude therefore approaches a constant value under this small  $k$  limit:

$$\lim_{k \rightarrow 0} f(\theta) = \frac{\delta_0}{k} = -a, \quad (2.28)$$

where  $a$  is termed the *scattering length* due to the similarity to the scattered long-range wavefunction induced by a hard-sphere potential [36]. Meanwhile the large  $R$  wavefunction (Equation 2.25) approaches the limit

$$\lim_{k \rightarrow 0} \Phi(R) \xrightarrow{R \rightarrow \infty} R - a. \quad (2.29)$$

As the energy tends to zero, the large  $R$  wavelength tends to infinity, and the wavefunction tends to a straight line that would intercept the  $R$ -axis at  $R = a$ .

The scattering length is an important parameter relating to ultracold collisions. It determines the low-energy elastic cross-section for colliding bosons [35]. It also determines both the strength and sign of the mean-field interaction within the description of a BEC formulated by the Gross–Pitaevskii equation [39].

## 2.2 Direct cooling techniques

The earliest popular approach to the direct cooling of molecules involved the supersonic expansion of a molecular beam. When a supersonic nozzle is installed onto the end of a high-speed rotor [40], the mean longitudinal velocity of the molecular beam

increases, but the width of its distribution decreases, and the internal temperature of the molecules is decreased via collisional relaxation. The beam velocity distribution can be increased or decreased in the laboratory frame depending on the relative velocities of the rotation and the molecular jet. This technique can form internally cold molecules in any species, but only produces translational temperatures of the order of a few Kelvin.

Under the process of helium buffer gas cooling, paramagnetic molecules are loaded into a  $^3\text{He}$  or  $^4\text{He}$  buffer gas which thermalizes them to a temperature of approximately 240 mK in their lowest internal energy configuration [41]. They are then loaded into a magnetic trap where evaporative cooling can subsequently be applied.

A third approach is Stark deceleration, or electrostatic slowing, whereby an adiabatically cooled beam of polar molecules such as deuterated ammonia are slowed by time-varying inhomogeneous electric fields prior to storage in an electrostatic trap [14, 42]. State-selected molecules are cooled to translational temperatures below 350 mK.

The common limitation of these direct approaches is the relatively warm translational molecular temperatures obtained. Recently, an optical cycling scheme has been applied to SrF molecules in order to effect a degree of translational cooling [43]. A dissipative cooling cycle has also been proposed for polar molecules trapped in electric fields [44]. Despite this preliminary promise of translational temperatures within the millikelvin range via direct routes, indirect schemes nevertheless show

the greater potential for the obtention of ultracold, sub-millikelvin temperatures.

## 2.3 Indirect cooling techniques

In order to attain ultracold translational temperatures within the  $s$ -wave scattering regime, it is necessary to pursue indirect cooling techniques. The application of near-resonant laser fields to cool and trap hot atoms (see Section 4.2 and references therein) is a robust and well documented technique. It relies on the availability of a two-level closed-loop cooling cycle that is offered by many atomic species but which may not easily be isolated within the more complicated molecular environment. Further evaporative cooling may be applied to the atoms to increase the density and consequently improve association efficiency, with the target the coherent, macroscopically degenerate state of matter that is the BEC [7, 8].

The various indirect techniques presented within this section all share the same initial step of starting with pre-cooled atoms via these established techniques. They differ in terms of the subsequent step, whereby cold atom pairs are associated to form molecules, as well as the internal energy level distributions that may typically result.

### 2.3.1 Feshbach resonances

The Feshbach resonance is a valuable tool for manipulating ultracold collisional processes via tuning the scattering length [45]. As described in Section 2.1.5, atomic collisions at ultracold temperatures can be described in terms of the  $s$ -wave scatter-

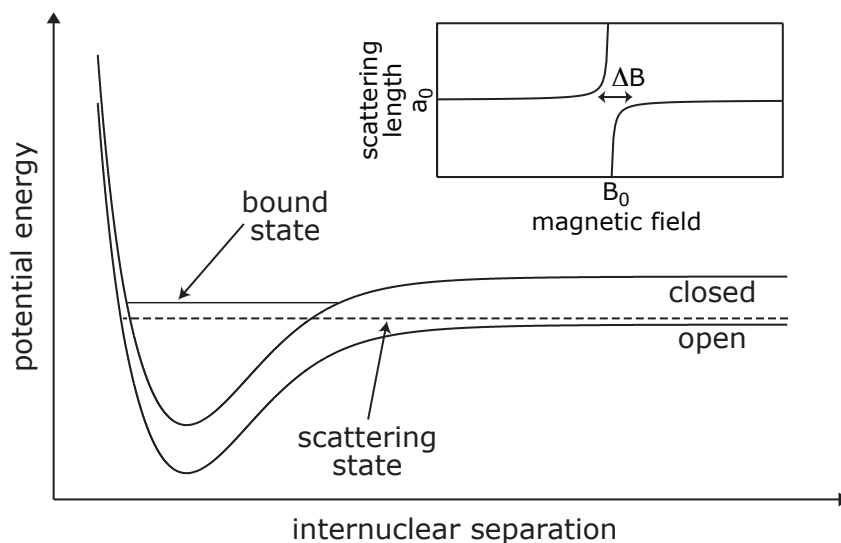


**Figure 2.5** The modification of the scattering length by a Feshbach resonance with a near-resonant bound state within a closed channel. The resonant deviation of the scattering length from its off-resonant value,  $a_0$ , across a resonance of width  $\Delta B$  induced by a Zeeman splitting at magnetic field  $B_0$  is inset.

ing length  $a$ . The scattering length takes, in general, a constant value for a particular collisional species. It can, however, be greatly modified by a resonant process due to the presence of a near-resonant bound state in a closed channel. Such a channel may alter the scattering properties of the atom pair despite being energetically inaccessible to the colliding atoms. This resonant situation is illustrated in Fig. 2.5.

This resonant variation in the scattering length can, under certain circumstances, be tuned in the laboratory [46]. Both molecular potentials and their atomic asymptotes are subject to hyperfine splittings. This results in a series of closely spaced molecular potentials, each correlating with atomic thresholds with different combinations of total angular momentum  $F$ . Some of the loosely bound vibrational states within the higher potentials may be nearly resonant with the dissociation threshold

of the lower potentials. This resonance may be tuned by application of a magnetic field such that the induced Zeeman splitting is different between the open and closed channels. This allows for sensitive manipulation of the scattering length, and hence control of the interactions, between the cold atoms.

In addition to tuning scattering lengths, Feshbach resonances may be harnessed as a technique to transfer population from a scattering state to a bound state. If the magnetic field is swept slowly across the resonance, the scattering-state population will adiabatically follow its dressed state across the resonance and end up in a bound state. If the sweep is sufficiently slow for the adiabaticity condition to be met, then the transfer may be effected with an efficiency approaching 100 % [47, 48].

Feshbach resonances have been harnessed in this manner to produce loosely bound dimer molecules of various bosonic species:  $^{85}\text{Rb}$  [49],  $^{133}\text{Cs}$  [50],  $^{87}\text{Rb}$  [51] and  $^{23}\text{Na}$  [52]. Feshbach association has also been demonstrated within the environment of fermionic gases such as  $^6\text{Li}$  [19, 53, 54] and  $^{40}\text{K}$  [55], as well as Bose–Fermi mixtures such as  $\text{KRb}$  [56] (with encouraging prospects for  $\text{RbCs}$  [57]).

Though high transfer efficiencies may be obtained, these product molecules are constrained to high-lying vibrational states. The reason for this is the unrealistic strength of the magnetic field that would produce the Zeeman splitting required to bring more deeply bound states into resonance. Further techniques are therefore required in order to transfer these vibrationally excited states to deeply bound ones.

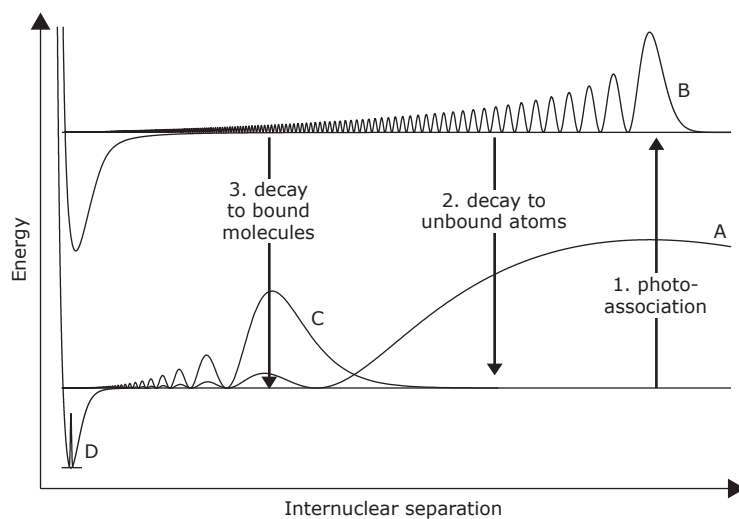


**Figure 2.6** A schematic illustration of the cw photoassociation process. (1) Two colliding atoms absorb a photon and photoassociate to form a weakly bound excited-state molecule. The molecule then spontaneously decay to either form: (2) an unbound pair of atoms, or (3) a bound molecule in the electronic ground state. Probability distributions of an initial  $s$ -wave scattering state (A), a photoassociated long-range excited state (B), a ground state with a favourable Franck–Condon factor for decay from B (C), and the lowest ground vibrational state with poor Franck–Condon overlap (D) are all shown.

### 2.3.2 Continuous-wave photoassociation

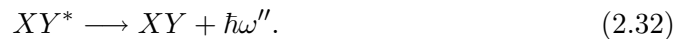
An alternative technique for the indirect synthesis of ultracold molecules from pre-cooled atoms is that of photoassociation,<sup>4</sup> as first proposed by Thorsheim *et al.* [15]. A pair of ultracold colliding atoms absorb a photon from the photoassociation laser field to form a bound excited-state molecule:



The subsequent spontaneous decay of the excited molecule may either form an unbound pair of atoms,



or a bound molecule in the electronic ground state,



This process is illustrated schematically in Fig. 2.6 for a typical *s*-wave scattering state in rubidium. Due to the long-range nature of the scattering-state wavefunction the excited-state molecule is also of long range and vibrationally excited, as dictated by the Franck–Condon principle. Consequently, the Franck–Condon factors governing the population of the most deeply lying ground vibrational states via spontaneous decay are small.

---

<sup>4</sup>The semantic issue of whether one photoassociates *atoms* or *molecules* is a potentially befuddling but immaterial diversion. The former convention will be adopted herein in accordance with the greater part of the literature.

The absolute rate of photoassociative molecule formation per atom in the initial state may be derived according to a perturbative approach as [58]:

$$R_{\text{PA}} = A \left( \frac{3}{2\pi} \right)^{3/2} \pi \hbar n \lambda_{\text{deB}}^3 e^{\frac{-\hbar\Delta}{k_{\text{B}}T}} \frac{\Omega^2}{4} |\langle \Psi' | \Psi \rangle|^2, \quad (2.33)$$

where  $A$  is an angular factor,  $n$  is the atomic density,  $\Delta$  is the detuning from resonance,  $\Omega$  is the atomic Rabi frequency and  $|\langle \Psi' | \Psi \rangle|^2$  is the Franck–Condon factor. Key factors in attaining a high formation rate are therefore the temperature, number of atoms and density, as well as the spatial overlap of the scattering state with the target molecular state.

Homonuclear and heteronuclear molecules offer complementary advantages with regard to the formation of bound ground-state molecules at ultracold translational temperatures. As discussed in Section 2.1.3, the long-range asymptotic behaviour for heteronuclear molecular potentials corresponding to both  $S+S$  and  $S+P$  atomic states scales as  $R^{-6}$ . By contrast, excited homonuclear  $S+P$  states scale as  $R^{-3}$ . As a consequence, the photoassociation illustrated in step 1 of Fig. 2.6 is more favourable for homonuclear dimers due to the greater Franck–Condon overlap between the scattering state and the longer range  $R^{-3}$  excited state. The Franck–Condon factors for a subsequent stimulated or spontaneous decay to bound ground states, however, are greater for the case of heteronuclear molecules due to the similarity of ground and excited states.

The complementary merits of homonuclear and heteronuclear dimers have been

reflected in research progress within this field. Initial advances addressed homonuclear molecules: continuous-wave (cw) photoassociation and spontaneous decay were used to form  $\text{Rb}_2$  [59, 60],  $\text{K}_2$  [61],  $\text{Cs}_2$  [16, 62–64] and  $\text{Na}_2$  [65] in a range of ground singlet and triplet vibrational states. Nikolov *et al.* subsequently employed a second cw field to couple the long-range photoassociated excited state to a short-range higher lying excited state, which decayed to deeply bound vibrational states within the ground-state singlet potential [66]. Subsequently, following the feasibility study of Wang and Stwalley of appropriate heteronuclear molecules that supported an attractive long-range excited-state potential [67], similar techniques have been applied to dual-species experiments. These initially applied cw photoassociation followed by spontaneous decay to produce a mixture within the ground singlet and triplet potentials in  $\text{NaCs}$  [68] and  $\text{KRb}$  [69, 70]. Meanwhile the DeMille group developed a two-step excitation scheme followed by stimulated transfer to  $v = 0$  within the ground singlet potential in  $\text{RbCs}$  [71–74]. More recently, high-power photoassociation has enabled the population of an excited state with good Franck–Condon overlap to  $v = 0$  in the ground singlet state of  $\text{LiCs}$  [75].

As outlined above, however, the Franck–Condon principle tends to restrict these techniques to the production of highly vibrational product states. In the case of the multi-step routes to deeply bound vibrational states via an intermediate with favourable Franck–Condon overlap, a reliance on a spontaneous decay step results in the production of an incoherent mixture, as well as centre-of-mass heating. In general, more advanced approaches are required in order to target deeply lying

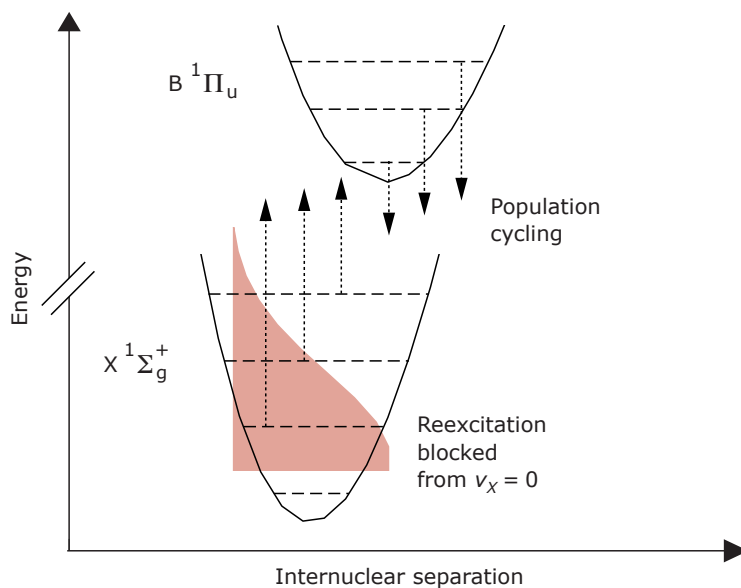


**Figure 2.7** The incoherent optical cycling scheme of Viteau *et al.* [20]. Initial population in a mixture of deeply bound vibrational states within the  $X^1\Sigma_g^+$  potential is pumped to vibrational states within the  $B^1\Pi_u$  potential using a broadband optical pulse. Spontaneous decay then returns the population to the  $X^1\Sigma_g^+$  ground state. The blocking of spectral intensity that would excite population from  $v_X = 0$  results in population accruing within this vibrational ground state within a few cycles.

vibrational states, as well as to prepare cold molecular samples of high purity.

### 2.3.3 Incoherent optical cycling

In 2008, Viteau *et al.* reported the demonstration of a broadband optical cycling scheme that prepared an ultracold molecular gas of  $\text{Cs}_2$  in the  $v = 0$  level of the ground singlet electronic state from atoms in a magneto-optical trap (MOT) [20]. Under this scheme, population is first prepared in deeply bound vibrational states of the  $X^1\Sigma_g^+$  potential using a cw photoassociation route discussed below. This population is then pumped to vibrational levels within the  $B^1\Pi_u$  potential using a

broadband optical pulse:

$$|X^1\Sigma_g^+, v_X\rangle + \hbar\omega \rightarrow |B^1\Pi_u, v_B\rangle. \quad (2.34)$$

These excited states then spontaneously decay back down to the  $X$ -state, ideally populating some more tightly bound vibrational states:

$$|B^1\Pi_u, v_B\rangle \rightarrow |X^1\Sigma_g^+, v'_X\rangle + \hbar\omega'. \quad (2.35)$$

Since the highest transition energy for this cycle corresponds to transitions from  $v_X = 0$ , the introduction of a spectral cut into the pump pulse blocking all higher frequencies than this transition prevents the reexcitation of the ground vibrational state. In this manner, population is gradually accumulated within the dark  $v_X = 0$  state through repeated excitations and spontaneous decays. Of the fraction of the initial population that lies within the occupation window of  $0 \leq v_X \leq 10$ , 65% is transferred to  $v_X = 0$ . The process saturates after around 5000 pulses ( $60 \mu\text{s}$ ). Given that the interaction probability is 0.1% per pulse, this implies that a typical molecule undergoes no more than five cycles of optical pumping and spontaneous emission in order for transfer to  $v_X = 0$  to be completed, and thus heating of the centre-of-mass motion is not significant. This experiment was subsequently developed to include active pulse-shaping that blocked excitation frequencies from a number of low-lying singlet vibrational levels in order to demonstrate the proof-of-principle preparation of population in arbitrary vibrational states [76]. The results have also

been replicated using an incoherent light source [77].

The starting population for this experiment is prepared using a cw photoassociation laser detuned around  $1\text{ cm}^{-1}$  from the  $6S_{1/2}-6P_{3/2}$  caesium transition. Through resonant coupling of various molecular potentials [64], some population is transferred to the  $v = 0$  level within a potential curve correlating with the  $6S_{1/2} + 5D_{5/2}$  atomic asymptote, with internuclear separations commensurate with deeply bound levels within the  $X$ -state [78]. In this manner, a cw photoassociation route may be employed to prepare a significant initial population within low-lying ( $v_X \leq 10$ ) ground singlet states. Crucially, this both permits the subsequent broadband cycling using experimentally feasible pulse parameters, and expedites the transfer of population to  $v_X = 0$  within a few spontaneous decay cycles without significant heating. This pathway is not, in general, available within other species. Caesium is the heaviest stable alkali metal,<sup>5</sup> and, as such, possesses the largest quantum defect between the low- $l$  outer electronic energy levels and their equivalents in atomic hydrogen. The  $5D$  term experiences less nuclear shielding than in the lighter alkalis due to the greater extent of the closed electronic shells, and the  $6P-5D$  splitting is consequently much lower than for the equivalent  $nP - (n - 1)D$  splittings in the lighter alkalis. The existence, therefore, of a deeply bound vibrational state within a  $6S_{1/2} + 5D_{5/2}$  potential that is near-degenerate with  $6S_{1/2} + 6D_{3/2}$  (and the associated pathway to low  $v_X$ ) is a serendipity unique to caesium.

---

<sup>5</sup>Trapping has also been demonstrated for the heaviest alkali atom, francium [79]; however the lack of a stable isotope (the highest half-life is 22 minutes) requires the extra complication of a francium production mechanism.

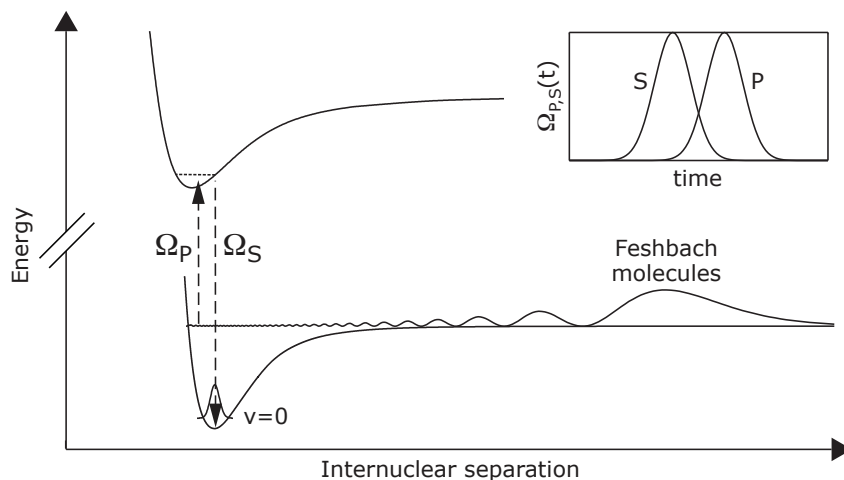


**Figure 2.8** STIRAP as a tool for the formation of deeply bound molecules. A highly vibrational ground-state molecule is associated using the Feshbach resonance technique. This bound state is coupled to an excited state by a time-varying pump laser with Rabi frequency  $\Omega_P(t)$ . A Stokes laser with Rabi frequency  $\Omega_S(t)$  couples the excited state to a deeply bound final state. The pulse sequence is inset.

### 2.3.4 STIRAP

A robust technique for the complete transfer of population between states is STIRAP [80]. A pairs of pulses, partially overlapped in time, indirectly couple an initial to a final quantum state via an intermediate state. The pulses are applied in a counter-intuitive sequence, with the Stokes field first coupling the two initially unpopulated states before the pump field couples in the occupied initial state. The process and pulse sequence are illustrated in Fig. 2.8. The population evolves adiabatically during the evolution of the control fields, and is steered to the target state via a dressed-state eigenstate that contains no intermediate state population. This enables a coherent population transfer to be carried out without spontaneous losses.

STIRAP schemes have been implemented experimentally in a number of species.

Cs<sub>2</sub> Feshbach molecules have been transferred into the  $v = 73$  level of the ground singlet [21]. The scheme has recently been extended to transfer population into the rovibronic ground state [81]. The technique has also been used to populate the ground vibrational state within the ground-state <sup>87</sup>Rb<sub>2</sub> triplet [22], more deeply bound states within the singlet [23], and both singlet and triplet ground states of the heteronuclear KRb [24].

STIRAP transfer of Feshbach molecules to deeply bound vibrational states has been demonstrated to be an efficient technique in a variety of species, so long as sufficient initial density can be attained. It has the advantage of being a coherent process and can be reversed through the time reversal of the control fields. The choice of the phase-stabilized control fields, however, requires full spectroscopic knowledge of the system.

### 2.3.5 Ultrafast photoassociation

The application of ultrafast pulses to the photoassociation of ultracold molecules represents an apparent contradiction. The ultrafast regime is generally ascribed to processes that occur on sub-picosecond timescales. Ultrafast pulses are typically used as tools to probe such processes in a time-resolved manner [82], as well as in applications that benefit from the very high peak intensities of the short pulses. By contrast, the term ‘ultracold’ signifies sub-millikelvin temperatures, corresponding to ‘ultraslow’ thermal motion. Typical timescales in the context of this thesis range from the many-picosecond periods of long-range vibrationally excited molecules,

through the 26 ns excited-state lifetime of the rubidium trapping transition, to the millisecond timescales over which  $\text{Rb}_2$  dimers photoassociated from the MOT will drift out of the interaction region. The resolution of this contradiction lies in the fact that the broad coherent bandwidth of a Ti:sapphire ultrafast pulse is well matched to typical alkali dimer potential binding energies, while the carrier frequency is appropriate for ground- to excited-state transitions. An ultracold scattering event may therefore be steered toward a target state through a variety of vibronic pathways. Additionally, femtosecond pulses offer a time-resolved probe for molecular dynamics (see Chapter 6).

### **Motivation and approach**

Due to the expertise required to combine ultrafast and cold matter technologies, this experimental trail has been less well blazed than the alternative approaches to ultracold molecules in low internal energy configurations introduced above. It is nevertheless an important strategy to explore, as it offers some advantages over both STIRAP and incoherent optical cycling. The choice of tailored optical photoassociation pulses may be guided by a closed-loop optimization of the desired target state signal (see Chapter 3); thus neither specific knowledge of the vibrational spectroscopy of the species nor precise laser stabilization with respect to the transitions is required beyond the general matching of the broadband pulse to the transition as discussed above. The apparatus may, in principle, therefore be applied to other molecular systems with some flexibility. Through the use of both ‘pump’ and ‘dump’

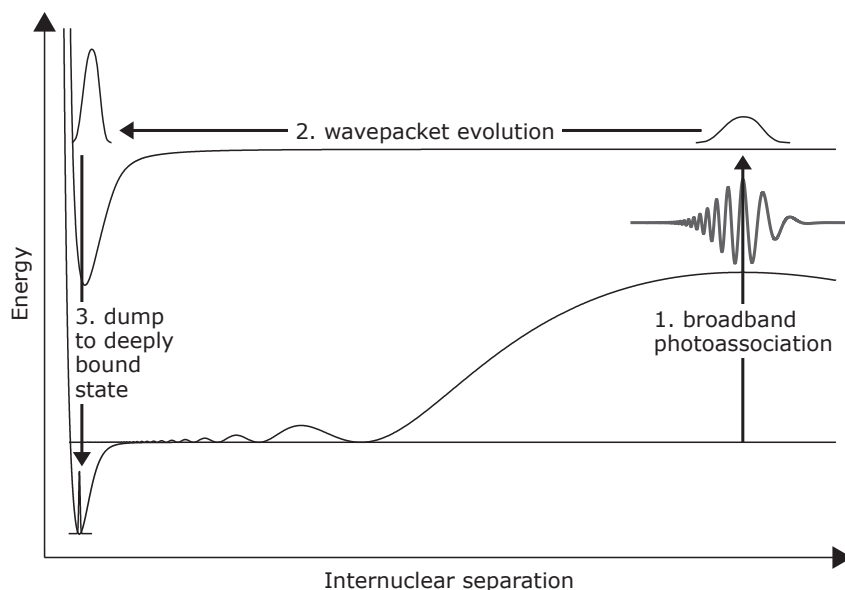


**Figure 2.9** A schematic illustration of broadband photoassociation. A broadband, shaped optical pulse photoassociates a colliding scattering atom pair to form a coherent superposition of excited vibrational states (1). This wavepacket evolves within the excited-state potential energy surface, moving to closer range (2). After a particular delay, the wavepacket has developed a favourable Franck–Condon overlap with a deeply bound target state, to which the population is transferred via a dump pulse. The anharmonicity of the excited state may be pre-compensated through the design of the control field, permitting some wavepacket focussing at close range.

pulses, a fully coherent transfer to the ground state may be effected.

The basic principle is that the ultrafast pulse photoassociates scattering population over a range of internuclear separations into a coherent superposition of excited rovibronic states. This coherent, non-stationary excited state — known as a wavepacket — undergoes time evolution on the excited-state potential energy surface, moving to shorter range due to its attractive nature. After some delay, the wavepacket will have developed a greater Franck–Condon overlap with deeply bound ground states than the initial population, and a second pulse may be employed to

‘dump’ the population into these target states. This mechanism is illustrated in Fig. 2.9. This exploitation of a coherent superposition of states thus offers a pathway to deeply bound product molecules despite the poor Franck–Condon factors of the individual vibrational states. Furthermore, shaping of the spectral phase and amplitude of the photoassociation pulse enables this process to be optimized, for instance by pre-compensating for the anharmonicity of the excited state in order to focus the wavepacket at close range.

### Recent theoretical and experimental history

Ultrafast photoassociation in ultracold matter with picosecond pulses was originally proposed by Machholm *et al.* in 1994 [83]. Over the next few years, some theoretical proposals and experimental progress materialized concerning the wavepacket dynamics ensuing from photoassociation with picosecond and femtosecond pulses in thermal vapours [84–86]. Vardi *et al.* proposed a scheme to transfer population to bound levels within the ground state with a nanosecond pulse pair [87]. The use of chirped picosecond pulses to form cold  $\text{Cs}_2$  molecules by photoassociation was proposed by Vala *et al.* in 2000 [88], and the concept was subsequently developed by Luc-Koenig *et al.* using a more realistic initial state [89, 90]. The extension of this work to a two-colour ‘pump-dump’ scheme was first proposed in 2006 by Koch *et al.* [91], who advocated picosecond dump pulses to populate a single target vibrational state or femtosecond dump pulses to populate several states.

In the meanwhile, experimental progress did not keep pace with this prolificacy of

theoretical proposals. An obstacle was the inconvenience of the picosecond regime: nanosecond pulses may be shaped directly in the temporal regime, and femtosecond pulses may be shaped indirectly in the spectral regime [92], however intermediate timescales constitute an experimental void. A ‘pump-decay’ experiment conducted by the author’s predecessors at Oxford revealed that 100 fs pulses caused a coherent quenching effect on pre-formed triplet molecules in the MOT when chirped by a factor of 50 [27, 93]; similar results were also obtained by a collaboration between research groups in Freiburg and Berlin [94]. A collaboration between research groups in Durham and Newcastle was set up to explore ultrafast photoassociation in heteronuclear RbCs, in parallel to the work in Oxford on Rb<sub>2</sub>.

At this stage, the direction of theoretical advances was adapted to take account of the experimentalists’ shortcomings with regard to picosecond pulse-shaping. Koch *et al.* investigated using chirped, few-picosecond pump-dump and pump-decay routes to bound ground-state Rb<sub>2</sub> [95]. Poschinger *et al.* sought to optimize the dump pulse [96], while Mur-Petit *et al.* studied time-dependent beatings in the excited state due to the spin-orbit coupling of two channels [97]. Koch and Moszyński subsequently proposed using an additional infrared control field to couple a Ca<sub>2</sub> excited state that is convenient for photoassociation to an auxiliary state with more favourable Franck–Condon factors to the ground state [98]. Koch *et al.* have also proposed two-photon broadband photoassociation to excite vibrational states close to the  $5S + 5P_{1/2}$  atomic asymptote whilst suppressing the atomic resonance [99].

Given that the ultrafast photoassociation experiments mentioned above had ob-

served an unexpected reduction of the ground-state signal, the next experiments employed pump-probe techniques [83, 100] to make a time-resolved measurement of the excited-state population. Knowledge of the wavepacket dynamics would inform the choice of parameters for a pump-dump scheme, and pulse-shaping techniques could be applied to focus the wavepacket in preparation for the dump step. The Freiburg and Berlin collaboration discovered coherent transient oscillations in the molecular ion signal [101, 102]. The sharp spectral cut applied to the pump pulse introduced a long tail into the pump-pulse envelope in the corresponding temporal domain. In exciting an atom pair, the pump pulse induces an electronic dipole which interacts coherently with this long temporal tail, causing oscillations in the excited-state population and hence the  $\text{Rb}_2^+$  signal. This behaviour is similar to the observations of Zamith et al. in a Rb vapour cell [103]. Meanwhile, a similar pump-probe experiment in Oxford was able to infer important initial-state information from the rate at which the molecular ion signal dropped off with pump-pulse detuning [104, 105]. The results of these experiments are presented within this thesis. Also, in an accompanying theoretical paper, Martay *et al.* proposed two experimentally feasible experiments to demonstrate coherent control of the pre-formed loosely bound molecules formed by MOT photoassociation [106]. This also demonstrated that an incoherent initial state of bound molecules would not preclude the initiation of coherent excited-state dynamics by a pump pulse.

## 2.4 Purity considerations

A discourse on cooling methods within a system with a number of different degrees of freedom requires a consideration of what is actually implied by the term ‘cooling’. A diatomic molecule possesses an internal energy-level structure consisting of electronic, rotational and vibrational components, as well as kinetic energy due to translational motion. The ‘cold molecules’ research field is motivated by the creation of samples of different molecular species with low kinetic energies that reside within their lowest internal state — or, at least, a low-lying, user-prescribed state or range of states. The pursuit of this goal is often affirmed to be ‘cooling’ as a matter of semantic convenience; however, the term must be used in this context with a certain degree of caution. The action of the MOT lasers may accurately be termed cooling, since it employs spontaneous emission as a means of dissipating the energy of the trapped atoms. The evolution of the internal degrees of freedom, however, is most accurately depicted in terms of the purity of the quantum state.

The most general representation of an impure quantum system is afforded by the density matrix,  $\rho$ . From this perspective, cooling of the system requires an increase in the system purity, as characterized by  $\text{Tr}(\rho^2)$ . Hamiltonian evolution, however, such as that effected by external control fields, does not change the purity of the

system:

$$\begin{aligned}
 \frac{d}{dt} \{ \text{Tr} (\rho^2) \} &= 2 \text{Tr} (\rho \dot{\rho}) \\
 &= \frac{2}{i\hbar} \text{Tr} (\rho [H, \rho]) \\
 &= \frac{2}{i\hbar} \text{Tr} (\rho H \rho - \rho \rho H) \\
 &= 0
 \end{aligned} \tag{2.36}$$

due to the cyclic invariance of the trace operator for finite matrices. Instead, an increase in the purity requires dissipation through, for example, spontaneous emission — a process which is inherently uncontrollable [107]. External control fields may therefore only be used to create a high-purity target state under one of the following circumstances:

- The system is prepared beforehand in an initial state of high purity. An example of this is the Feshbach association of molecules followed by STIRAP transfer to deeply bound vibrational states (see Section 2.3.4). In this scenario, the system's purity is increased to near unity via evaporative cooling prior to association.
- After Hamiltonian evolution of an impure initial state via the control field, a portion of the state is discarded, removing entropy and leaving a new subsystem of higher purity. An example of this is broadband photoassociation (Section 2.3.5). The selectivity of the photoassociation window (due to both the Franck–Condon factors and the pulse spectral intensity) and the subsequent

discarding of the remaining initial population create excited-state dimers of higher purity than the initial system. These dimers may be transferred to the ground state by means of a further pulse whilst retaining this purity.

- The system purity is increased through a process that includes dissipation of energy. An example is the broadband cycling scheme demonstrated in  $\text{Cs}_2$  (Section 2.3.3), where excitation of an impure population of ground-state molecules is combined with spontaneous decay to produce a higher purity state predominantly within  $v = 0$ .

## 2.5 Summary

This chapter has introduced a physical model of a diatomic molecule, and discussed the mechanisms that give rise to its key characteristics at different internuclear separations. The Franck–Condon principle, which relates the vibrational transition probability to the overlap integral of the initial and final states, was summarized. Some scattering theory for the description of ultracold collisions was also presented.

In order to set the context of the work presented within this thesis, various approaches to the formation of cold molecules have been discussed. These approaches fall easily into two categories. Techniques that cool hot molecules directly produce low internal energies but relatively warm translational temperatures. Indirect techniques that associate cold atoms harness the low translational temperatures achieved through laser cooling, and are beginning to be used as the basis for methods that address the problem of rovibrational cooling. STIRAP has been used to transfer Fes-

hbach molecules to deeply bound vibrational states. Broadband pulses have been applied to a pre-prepared distribution of deep-lying  $\text{Cs}_2$  vibrational states in order to cycle population into the rovibrational ground state through repeated absorptions and spontaneous emissions.

Though currently less advanced than these alternative schemes, the prospects of using ultrafast pulses to photoassociate ultracold molecules is an enticing one, and motivated by the impetus of a body of proposals. The limitations of cw photoassociation may be circumvented through the creation of a time-evolving wavepacket in the excited state, followed by the application of a dump pulse to transfer the short-range wavepacket to the target state. The key concepts of this fully coherent approach are broadly applicable to a range of species, since no detailed spectroscopic knowledge is required in the design.



## Chapter 3

# Quantum control

*The Warrior of Light is wary of people who think they know the path.*

The research described within this thesis is motivated by the challenge of producing samples of molecules that are ‘cold’ in every sense that may be ascribed. Specifically, translationally cold molecules that occupy the lowest energy levels with respect to all their internal modes of freedom are desired. As has been discussed in the previous chapter, this task is complicated by the rich rovibrational energy level structure of even a simple diatomic molecule, such that the relatively straightforward laser cooling approach that succeeds for cold atoms may not be adapted. Instead, various schemes exist that seek to address this problem indirectly via associating pre-cooled atoms using tailored fields (see Section 2.3). The technique favoured within this thesis is the photoassociation of molecular wavepackets using broadband optical pulses.

The challenge of cold molecule production may therefore be portrayed in terms

of the design of appropriate control fields to steer an initial population of cold atoms towards a target state of cold, deeply bound molecules. This falls within the remit of the field of quantum control, which is introduced in this chapter. The extension of two-pathway control, whereby the outcome of a coherent reaction is manipulated through control of the relative phases of the interfering pathways, to broadband control is presented. The calculation of the optimal control pulses can be prohibitively hard for complex systems; however closed-loop feedback algorithms may be applied to solve the problem without full knowledge of the system Hamiltonian. Finally, the control considerations relevant to ultrafast photoassociation are briefly discussed.

### 3.1 Introduction to quantum control

A beguiling prospect for scientists aspiring beyond the mere observation of quantum mechanical systems is the application of optical control fields to influence their evolution [108, 109]. The 1960s heralded the arrival of laser technology and the subsequent availability of coherent light sources as a laboratory tool for such quantum control. The coherence properties of the light could be used to control quantum interference effects between two competing pathways of a chemical reaction, with the outcome influenced by the corresponding relative phase:

$$|A_1 + A_2|^2 = |A_1|^2 + |A_2|^2 + 2|A_1||A_2|\cos(\phi_1 - \phi_2), \quad (3.1)$$

where  $A_1 = |A_1|e^{i\phi_1}$  and  $A_2 = |A_2|e^{i\phi_2}$  are the amplitudes of the two pathways.

This process of manipulating interferences between a pair of specific pathways is known as two-pathway control. Though such schemes show promise in both solid-state [110] and gas phases [111, 112], problems can be encountered within more complex systems due to population transfer to the many internal energy modes [25].

The experimental burden of extending two-pathway control to multiple pathways using combinations of cw lasers becomes prohibitive; however, the development of sub-picosecond solid-state laser systems in the 1990s triggered the inception of broadband coherent control schemes. The maturation of pulse-shaping technology — particularly the  $4f$ -line with an active shaping element in the Fourier plane [92] — allowed phase and amplitude control over many simultaneous pathways in more complex systems. Broadband control schemes have been demonstrated for applications such as multiphoton transitions [113, 114], molecular alignment and dissociation control using the Stark effect [115, 116], and the control and shaping of molecular wavepacket evolution [117–119].

The ‘open-loop’ design of a broadband control field requires, in effect, the reverse engineering of the correct Hamiltonian that drives the system from an initial state to a desired target state:

$$|\psi(0)\rangle \xrightarrow{\hat{H}(t)} |\psi(t)\rangle = |\psi_{\text{target}}\rangle. \quad (3.2)$$

Laboratory control is effected over  $\hat{H}(t)$  via the dipole interaction with the control

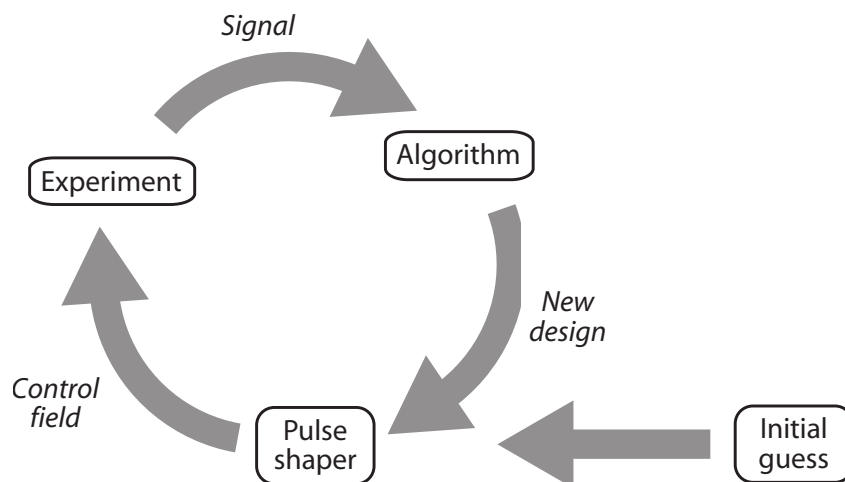


**Figure 3.1** The principle of closed-loop control. An initial pulse shape is guessed and applied to the experiment. A signal indicating the resemblance of the result to the target product is measured, and applied to an algorithm that generates an improved control field. This loop is iterated until it converges onto a solution.

field  $E(t)$ ,

$$\hat{H}(t) = \hat{H}_0 - \hat{d} \cdot E(t), \quad (3.3)$$

where  $\hat{H}_0$  is the field-free Hamiltonian. The multiple pathways that may thus be addressed, however, compound the theoretical complexity of designing suitable control fields from first principles. It was noted in Chapter 2 that certain approximations are required to describe the Hamiltonian of even a diatomic molecule. Furthermore, the theoretical description is obfuscated by decoherence effects and other interactions with the environment, as well as the robustness of the system with respect to variations in the desired electric field due to the performance of the pulse shaper.

## 3.2 Closed-loop control

An alternative approach to the direct design of the control field is to allow the experimental system to converge upon a solution via an iterative loop [120, 121]. An initial guess is ventured, and a learning algorithm is applied to converge upon an optimum design via trial and improvement (see Fig. 3.1). An experimental measurement that compares the final state to the desired outcome is used as the feedback signal. In this sense, the system may be considered to solve the Schrödinger equation despite the lack of knowledge of the true system Hamiltonian. Furthermore, the optimized pulse shape may yield spectroscopic information about the system as well as offer enlightenment over the reaction pathway. As a result, the desired outcome may be optimized despite imperfect knowledge of the system. Closed-loop schemes have been demonstrated as tools for pulse compression [122, 123], molecular population transfer [124, 125], the control of molecular photodissociation branching ratios [126, 127], as well as for other strong-field control applications [128, 129]. Consideration has been made of the robustness and simplicity of the control pulse, as well as the accuracy of the end product [130, 131].

## 3.3 Control of ultrafast photoassociation

The techniques outlined above lend themselves to the control of cold molecule formation via ultrafast photoassociation. A number of studies have proposed the use of picosecond or sub-picosecond pulses to form excited-state molecular wavepackets

and stabilize them into the ground state (see Section 2.3.5 and references therein). These techniques have addressed the design of both temporal and spectral pulse characteristics — for example via the timing of a dump pulse, or through a chirp applied to the pump pulse to increase population transfer.

Positively chirped pulses may be used in order to achieve a complete inversion of population to an excited-state potential — a technique known as a ‘molecular  $\pi$ -pulse’ [132, 133]. A study by Brown *et al.* using a two-potential model offered qualitative insight into control schemes in  $\text{Rb}_2$  [134]. A sequence of ‘ $2\pi$  pulses’ may be applied that excites and immediately de-excites population, enabling an incremental acceleration of the atom pair towards one another via the long-range attractive  $R^{-3}$  potential without sustaining excited-state population long enough for spontaneous decay. Strong control fields with timescales commensurate with the wavepacket dynamics may drive multiple cycles between the ground and excited state, forming a deeply bound product.

In reality, a system such as  $\text{Rb}_2$  offers a much more complex environment than the two-level system considered by these schemes for computational tractability. A manifold of potentials connect to the  $5S + 5P$  atomic asymptote (see Appendix A). Furthermore, effects such as the hyperfine interaction, rotation, transitions to higher potentials, and a realistic description of the initial state are typically omitted. Therefore, though such calculations offer insight into some physical mechanisms that show promise for the formation of deeply bound molecules, they do not offer a precise quantitative prediction of the system evolution. They should instead be considered

---

the motivation for optimizing the control pulse via closed-loop feedback, with the expectation that the structure of the optimized pulse will contain signatures of one or several of these mechanisms.

### 3.4 Summary

The formation of cold molecules that occupy their lowest electronic and rovibrational energy levels may be contemplated in terms of quantum control using tailored broadband pulses. In this chapter, the concept of quantum control has been introduced, along with the extension of two-pathway control schemes that manipulate quantum interferences to the more general approach with broadband pulses and complex systems. The merits of using closed-loop feedback to perform a robust optimization of the field despite imperfect system knowledge is summarized. Some control schemes specific to ultrafast photoassociation have been introduced. These schemes offer qualitative descriptions of mechanisms that show promise under an approximate model; a closed-loop optimization, however, is desirable in order to account implicitly for the limitations of this approximation.



## Chapter 4

# Experimental apparatus

*The Warrior of Light is always trying to improve.*

In this chapter, the apparatus used to conduct the experiments described within this thesis is described. The design of the MOT is presented together with the motivation for the choice of rubidium. The ultrafast system is described together with laboratory capabilities for broadband pulse shaping and characterization. The detection system is discussed in terms of the ionization lasers, ion detectors and data acquisition and manipulation.

The amalgamation of ultrafast optical techniques with ultracold atoms is a novel and recent approach to the pursuit of cold molecules. Since 2000, various theoretical proposals have advocated shaped short laser pulses as a tool for the photoassociation of ultracold atoms and stabilization into more deeply bound vibrational ground states than may readily be accessed by cw means (see Section 2.3.5). Experimental exploration of these suggestions has not been expeditious, principally due to

technological deficiencies regarding the generation and shaping of few-picosecond transform-limited pulses. The technology for sub-picosecond ultrafast pulse generation and shaping, however, is commercially available. When the author joined the Oxford experiment, it was one of two laboratories seeking to apply concepts from the picosecond photoassociation proposals using such ultrafast pulses;<sup>1</sup> as a consequence, little guidance could be gleaned from the literature, and aspects of the early experimental design were naturally somewhat exploratory. Following earlier experiments that identified coherent ground-state quenching [27, 93, 135], the author and colleagues sought to redesign the apparatus to allow the excited-state pump-probe studies discussed within this thesis. The crux of the design problem was that a lack of experimental molecular signal does not distinguish between shortcomings regarding production or detection.

A large part of the author's time working on the experiment was therefore spent addressing the detection and signal-to-noise issues, and making improvements to the apparatus to this effect. Since these improvements — though a very necessary part of the ensuing research — predominantly concern technical issues, their discussion has been confined to this chapter, with distinctions drawn as appropriate between the original apparatus inherited by the author and subsequent modifications. Unless otherwise stated, the modifications were implemented after the sets of experiments described in Chapters 5 but before those of Chapters 6 and 7.

---

<sup>1</sup>See Section 2.3.5 for more details of the recent history of this field.

## 4.1 Choice of species

The studies reported within this thesis were carried out in a rubidium MOT. Rubidium is an alkali metal with an atomic number of 37 and a ground-state configuration of  $1s^2 2s^2 2p^6 3s^2 3p^6 3d^{10} 4s^2 4p^6 5s^1$ . It is a soft, silvery metal at room temperature, and, though highly reactive in elemental form, occurs naturally in various minerals. It was discovered in 1861 by Gustav Kirchoff and Robert Bunsen, who named it after the past participle *rubidus* of the Latin *rubere* ('to become red') in reference to its spectroscopic lines [136]. Rubidium occurs naturally in two isotopes:  $^{85}\text{Rb}$  and  $^{87}\text{Rb}$ . The former is 72.2% abundant and is stable, whilst the latter accounts for the remaining fraction and has a half-life of  $4.9 \times 10^{10}$  years.<sup>2</sup> For both isotopes, the  $5P$  first excited term is divided into two levels by the fine-structure splitting: the  $5S_{1/2} \rightarrow 5P_{1/2}$  ' $D_1$  line' at 794.76 nm and the  $5S_{1/2} \rightarrow 5P_{3/2}$  ' $D_2$  line' at 780.03 nm (wavelengths in air). Both species are suitable for magneto-optical trapping using the  $F = I + S \rightarrow F' = F + 1$  hyperfine transition of the  $D_2$  line (see Fig. 4.1). A useful source of the two isotopes'  $D$ -line reference data has been compiled by Steck [137, 138].

A realizable coherent control scheme requires the frequency and bandwidth of the ultrafast pulses to be married with the pertinent transition energies of the ultracold atoms. To this effect, rubidium was selected for these experiments ahead of the other optically trappable alkali metals due to the suitability of its atomic and molecular spectroscopy to Ti:sapphire wavelengths. The rubidium  $D$ -lines are

---

<sup>2</sup>Which is a long time on the ultrafast timescale.

located near the peak of the Ti:sapphire gain profile, and the spread of transition energies from the  $\text{Rb}_2$   $a$ - and  $X$ -states to potentials within the  $5S + 5P$  manifold are commensurate with the pulse bandwidths of Ti:sapphire-based ultrafast laser systems (see Fig. A.3). A further motivation was the extent to which its collisional properties [139–145] and photoassociation spectroscopy [146–150] have been studied and catalogued. Rubidium therefore provides a convenient test bed for the control scenarios discussed within this thesis, though the concepts are expected to be of much broader utility.

## 4.2 Magneto-optical trap

The MOT system was based upon the design of Wieman *et al.* [151]. For a background to laser cooling and trapping, the textbooks of Metcalf and van der Straten [33] or Foot [37] are suggested. Alternatively, a historical insight may be obtained from the Nobel lectures of Chu, Cohen-Tannoudji and Phillips [2–4].

The hyperfine structure of  $^{85}\text{Rb}$  pertinent to laser cooling is shown in Fig. 4.1.<sup>3</sup> The trapping light is red-detuned from the  $F = 3 \rightarrow F' = 4$  transition. Due to its relative proximity, however, the trapper also excites a small fraction of the trapped atoms to the  $F' = 3$  level. From here, decay may occur to  $F = 2$ , from where reexcitation by the trapping light is not possible. The population thus remains in this ‘dark state’ and is lost to the cooling cycle. To counter this, an additional

---

<sup>3</sup>Note that the equivalent structure holds for  $^{87}\text{Rb}$  with the difference that each angular momentum value  $F$  is reduced by one, since the nuclear angular momentum  $I = 3/2$  for  $^{87}\text{Rb}$ , compared to  $I = 5/2$  for  $^{85}\text{Rb}$ .

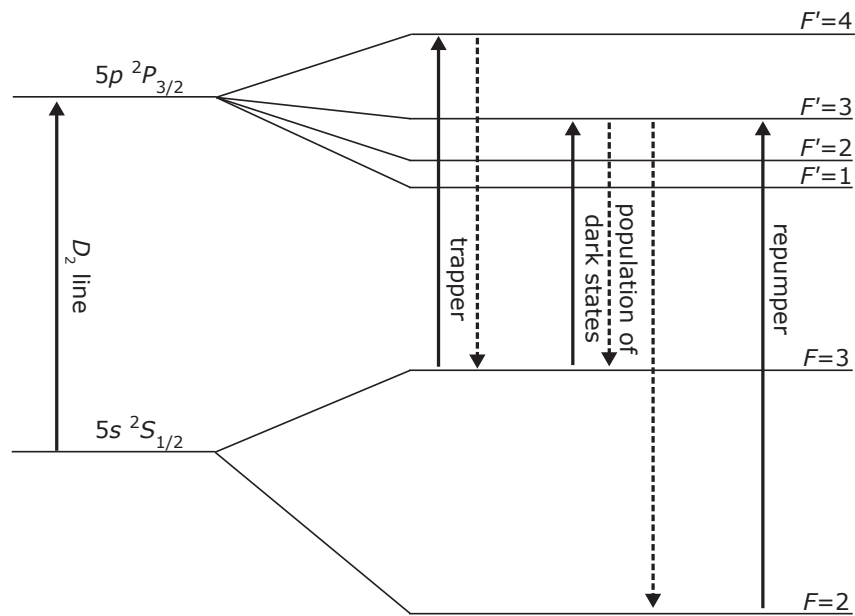


**Figure 4.1** The hyperfine splitting of the Rb  $D_2$  line and the trapping and repumping transitions. The trapping light is red-detuned from the  $F = 3 \rightarrow F' = 4$  hyperfine transition ('trapper'). Upon occasion, excitation occurs to  $F' = 3$ , from where decay is possible to  $F = 2$  as well as  $F = 3$  ('population of dark states'). The former state is dark to the trapping light, and so an extra laser is required to repump this population back into the cooling cycle ('repumper'). Transitions are shown for  $^{85}\text{Rb}$  ( $I = 5/2$ ); the equivalent picture for  $^{87}\text{Rb}$  ( $I = 3/2$ ) has corresponding angular momenta  $F$  and  $F'$  reduced by 1.

repumper laser is employed and tuned into resonance with the  $F = 2 \rightarrow F' = 3$  transition, thus restoring this population to the cooling cycle.

The light was generated by a pair of home-built external-cavity diode lasers (ECDLs) using 80 mW Sanyo DL7140-201S and 50 mW Hitachi HL7851-G laser diode chips for trapper and repumper respectively. The lasers were employed in the Littrow configuration, with the first order of an external grating coupled back into the diode cavity and offering wavelength feedback. The setup was based upon the designs of MacAdam *et al.* [152] and Ricci *et al.* [153]. A useful discussion of the trials and tribulations of harnessing commercial laser diodes for atomic physics experiments is offered by Wieman *et al.* [154].<sup>4</sup> Long-timescale immunity to wavelength drifts and mode-hops was improved using temperature stabilizers (Wavelength Electronics MPT-2500); meanwhile a piezo-electric transducer (PZT) that controlled the external cavity length, and tuning of the diode current, both offered faster frequency control.

Doppler-free spectroscopy was conducted on a pair of rubidium vapour cells using pick-offs from the trapper and repumper beams [155]. The technique employs a weak probe beam augmented by a strong counter-propagating pump beam. The twin mechanisms of transition saturation and population shelving allow the hyperfine structure to emerge from within the Doppler-broadened spectra, permitting a more precise measurement [156]. The resulting spectrum was differentiated electronically via a dither applied to the laser frequency together with a measurement of the

---

<sup>4</sup>The author of this thesis particularly relates to Section III G: *Catastrophic failure modes, or 1001 ways to kill a laser.*

induced change in probe-beam absorption. The resulting gradient was used as a feedback loop for locking the lasers to spectral maxima or minima via control over the PZT and diode current (Oxford Physics Central Electronics Group EW1225).

The trapper and repumper were protected from feedback due to back reflections from subsequent optical components via Faraday isolators (30 dB, OFR). They subsequently each passed through an acousto-optic modulator (AOM) (Isomet 1205C-2), which served to tune the lasers from their locking points to the desired frequency, as well as to act as fast optical shutters. As a result, the trapper was red-detuned 15 MHz from the  $F = 3 \rightarrow F' = 4$  transition (corresponding to a detuning of  $2.5\Gamma$ , where the natural linewidth  $\Gamma = 2\pi \times 6.1$  MHz), and the repumper was tuned in resonance with the  $F = 2 \rightarrow F' = 3$  transition.

In order to minimize the deleterious impact on the lifetimes of atoms in the trap of collisions with hot background atoms and molecules, the experiment was conducted within an evacuated stainless steel chamber with numerous glass viewports for optical access. The chamber was held at high vacuum by means of a turbomolecular pump (Pfeiffer TMU 071 P) backed by a rotary vane roughing pump (Edwards E2M1.5). A foreline trap between the two pumps filtered oil and water vapour that would otherwise contaminate the high vacuum. A Granville Phillips 275 Convec-tron Gauge monitored the roughing-line pressure and a hot-cathode ionization gauge (Granville Phillips Series 270) monitored the pressure inside the chamber. A typical roughing line pressure was 3 mTorr whilst the ion gauge indicated that the vacuum chamber was below its low-pressure threshold of  $10^{-8}$  Torr.

The expanded trapper beam was split into three equal-intensity beams using half-waveplates and polarizing beamsplitter cubes, and merged with the repumper. Typical powers were 4-5 mW of trapping light per beam and 2-3 mW total repumping light. The three circularly polarized beams intersected orthogonally within the vacuum chamber and were retroreflected. The MOT trapping region was thus the volume of overlap of these beams, which coincided with the minimum of a constant magnetic field gradient produced by passing an electric current through a pair of wire coils in the anti-Helmholtz configuration.

It is awkward to introduce solid rubidium into the vacuum chamber as a source of atoms due to its high reactivity, as well as its excessively high vapour pressure at room temperature ( $5 \times 10^{-7}$  Torr). Instead, three commercial ‘getters source’ rubidium dispensers were employed in series [157]. A getters source is a stainless steel housing that contains a rubidium compound together with a reducing agent; passing a current through the casing initiates the reduction reaction and releases rubidium vapour. Atoms from the low-velocity wing of the Maxwell–Boltzmann distribution are captured by the trapping light. The chamber vapour pressure may therefore be regulated by the choice of current with respect to the reaction threshold.

The atom cloud was imaged onto a charge-coupled device (CCD) camera (Cohu 4910) in conjunction with a beam analyzer (Spiricon LBA-100) in order to provide real-time information about the MOT number and profile for alignment and monitoring purposes. A second CCD camera with lower dynamic range provided an auxiliary image of the MOT from a different direction. The fluorescence from

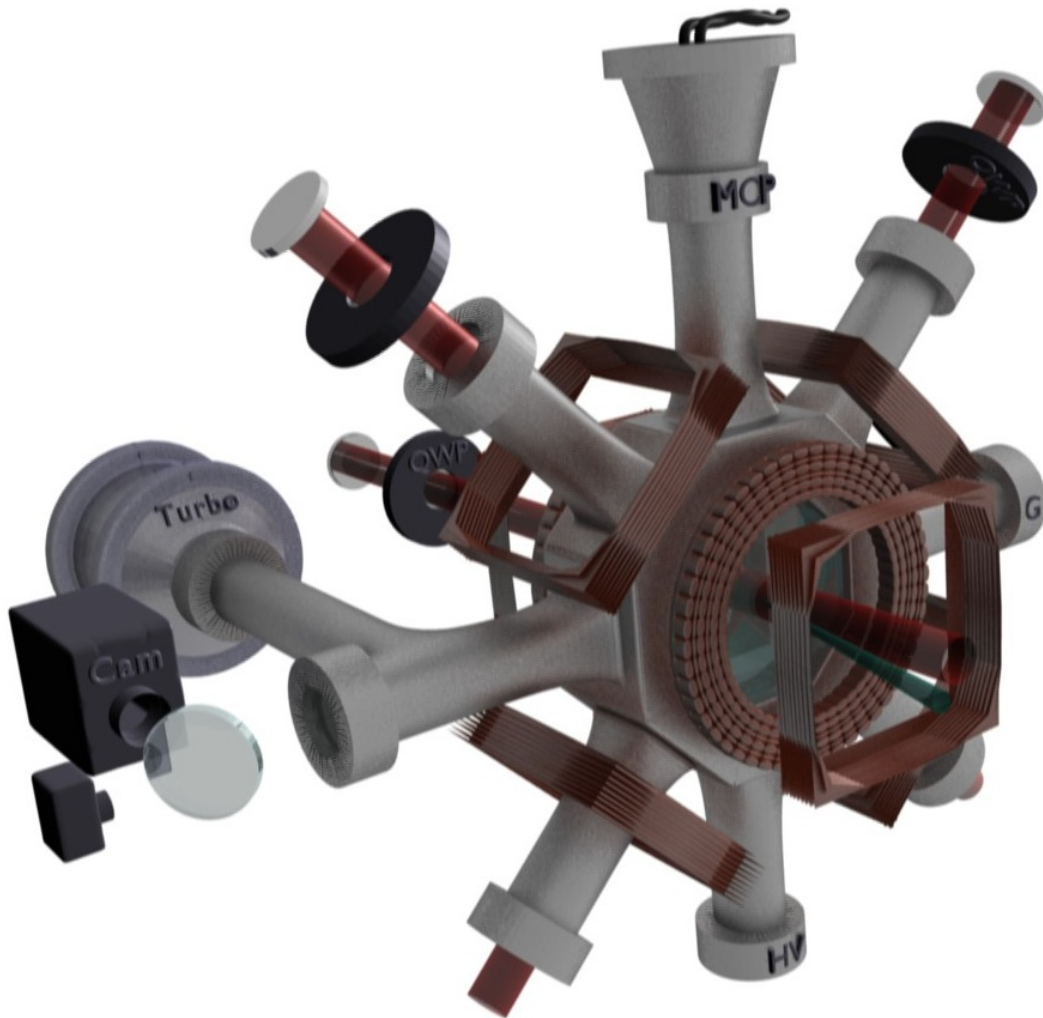


**Figure 4.2** A schematic diagram of the MOT chamber layout. Three orthogonal circularly polarized trapper beams intersect in the middle of a vacuum chamber evacuated by a turbomolecular pump (Turbo) backed by a roughing pump. Each beam is retroreflected and its polarization is reversed by means of a quarter-waveplate (QWP). A magnetic field gradient is generated by the current passing through a pair of coils (round) in the anti-Helmholtz configuration. Rubidium atoms released by a getters source (G) are captured in the centre of the MOT, and the MOT is monitored and imaged by a camera (Cam) and photodiode (PD). Atomic and molecular ions generated by the pulsed lasers are sent towards an MCP detector by a positive voltage applied to a pushing grid (HV). Three orthogonal sets of Helmholtz coils (square) are used to null stray magnetic fields. The photoassociation and ionization beams are also focussed onto the MOT through the front viewport.

the MOT was also imaged onto a photodiode in order to calibrate the number of atoms according to the method outlined in Section VI C of Wieman *et al.* [151]. A schematic diagram of the vacuum chamber layout is presented in Fig. 4.2.

### 4.2.1 Modifications

During the course of the experiments described in Chapter 5 and the early attempts at those of Chapter 6, it emerged that the inherent limitations of the MOT were impeding experimental progress. The daily optimization of the ultrafast system was a time-consuming process, and the similarly lengthy nature of the subsequent alignment onto the MOT meant that it often took the majority of the day to establish a perceptible molecular signal.

It became obvious that the day-to-day instability of the MOT itself was a particular hindrance to this daily routine. The trapper and repumper beams passed along several metres of beampath via many mirrors and other optical components before reaching the vacuum chamber. As a result, a slight alignment drift — due, for instance, to a loose mount or thermal fluctuations — had a drastic impact on the eventual alignment of the three orthogonal beams. Logging of the trap location on the Spiricon beam analyzer together with the number of atoms revealed fluctuations on a day-to-day timescale. Over a fortnight period, the MOT was observed to fluctuate randomly with a standard deviation of  $120\ \mu\text{m}$  in the horizontal and  $280\ \mu\text{m}$  in the vertical plane — with the result that the photoassociation and detection beams (whose waists were of the order of  $100\ \mu\text{m}$  at the MOT) needed realignment on a

daily basis. This drift also worsened the overlap of the MOT beams, and reduced the power coupled through various ‘bottleneck’ optical components, reducing the number of trapped atoms. Thus significant effort was required on a daily basis to maintain the quality of the MOT as well as to realign the other experimental beams onto its new location. Furthermore, the poor spatial profile of the diode lasers reduced the sphericity of the trap and worsened the matching to the transverse mode of these other beams.<sup>5</sup>

These issues were addressed via some modifications to the MOT apparatus. A considerable fraction of the available trapper diode power is lost through the various optical components prior to the MOT (notably the external cavity, the anamorphic prism pair, the pick-off to the saturated absorption spectroscopy cell, the Faraday isolator and the AOM). The trapping laser system was therefore modified to employ a master-slave configuration to increase the available trapper power (see Fig. 4.3). The slave was a 150 mW free-running laser diode (Roithner RLT780-150GS) housed inside a Thorlabs TCLDM9 mount in conjunction with a temperature controller (Newport 325B TEC) and a current driver (Oxford Physics Central Electronics Group EW1250). The existing frequency-stabilized trapper laser served as the master laser and was injected into the slave laser in order to stimulate lasing on the same mode. The injection power was adjustable with a half-waveplate and a polarizing beamsplitter. A Faraday rotator (Leysop FOI5/57) separated the slave output and

---

<sup>5</sup>A 50  $\mu\text{m}$  spatial filter placed at the focus of a trapping-beam telescope was not found to have a significant impact on the size of molecular signal, as the benefit of slightly improved mode was roughly cancelled by the effect of a reduction in trapping power. The omission of the spatial filter did, however, render the MOT more sensitive to the evolving spatial profile of ageing diodes.

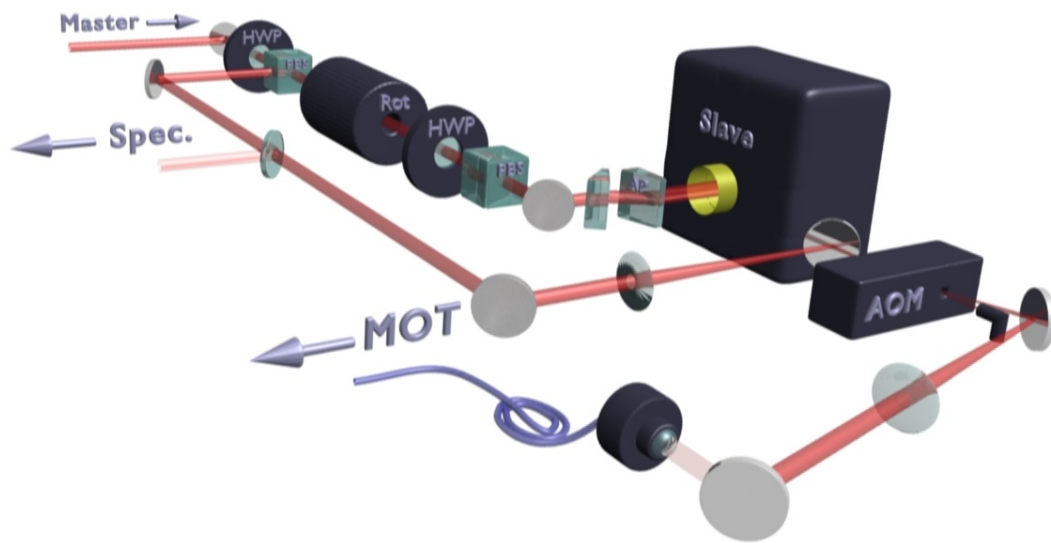


**Figure 4.3** A schematic diagram of the slave laser system layout. The master ECDL is used to inject a free-running diode laser, resulting in the availability of more trapping power. The master laser injection power is controlled with a half-waveplate (HWP) and a polarizing beamsplitter cube (PBS). The elliptical slave beam is made circular by an anamorphic prism pair (AP) and isolated from back reflections by a Faraday rotator (Rot) and a second polarizing beamsplitter cube. The output is separated from the master beampath and a pick-off is sent for monitoring and diagnosis via saturated absorption spectroscopy (Spec.). The beam then passes through an AOM before being coupled into a single-mode optical fibre and sent to the MOT.

the master input across two faces of the polarizing beamsplitter cube, and ensured optical isolation of the slave diode from back reflections in conjunction with a second beamsplitter. Saturated absorption spectroscopy on the slave output served as a diagnostic for the injection, with around 1 mW of master laser power being ample for good injection given careful optimization of the trapper alignment and slave current. The slave output then passed through the AOM,<sup>6</sup> followed by a single-mode, polarization maintaining optical fibre (Oz Optics PMJ-3AF3AF-850-5/125-3-1-1). This served to clean the transverse mode of the beam, improving the sphericity of the MOT. The fibre also acted as a bottleneck in the trapper beam path, with any alignment drift originating before the fibre resulting merely in a drop in power at the output. Thus the MOT could be reoptimized to its prior form through the act of adjusting the coupling efficiency through the optical fibre. Finally, three orthogonal pairs of compensation coils in Helmholtz configuration were added to the chamber in order to allow background magnetic fields to be nulled.

The selection of certain key parameters for the new MOT was guided by some atom capture calculations, discussed in more detail below. As a result of the introduction of the single-mode fibre, the systematic and random drift of the MOT was improved: the day-to-day location was repeatable to within  $50\ \mu\text{m}$ , and it became possible to retrieve a ground-state molecular ion signal immediately upon switching on the apparatus (Section 5.1) without realignment of either MOT or laser (a procedure which could previously take several hours). Furthermore, the slave laser system

---

<sup>6</sup>It would have been possible to obtain more trapper power for the MOT had the AOM been located in the master laser beam path prior to the slave, but this would have prevented the use of the AOM as a fast optical shutter for the photoassociation experiments.

increased the available trapper power from 4-5 mW to 8-9 mW per beam after the beam expanding and splitting optics. A typical MOT trapped  $2 \times 10^7$  atoms with a maximum density of  $10^{10} \text{ cm}^{-3}$  and a half-maximum diameter of 0.8 mm (see Appendix B). The MOT size was found to be reasonably stable with respect to minor fluctuations in trapper power coupled through the fibre, consistent with the onset of saturation in the simulations of Fig. 4.4(c). The MOT temperature was measured by the release-and-recapture method [158] to be  $111 \mu\text{K}$  (see Appendix B).

A limitation to the density of a MOT is the repulsive force resulting from the reabsorption of scattered light by other atoms. This problem is addressed by the dark spontaneous-force optical trap (dark SPOT) MOT [159]. Under this technique, a central repumper-free region is created within the MOT by imaging an opaque spot in the middle of the beam. Atoms within this ‘dark’ region accumulate within the lower hyperfine level and no longer participate in the trapping cycle. This technique was trialled in order to ascertain whether an improvement to the photoassociation rate (which scales in proportion to the product of the density and the number of trapped atoms) could be made. This modification was found to be impractical, however, within the confines of the existing apparatus. The rubidium loss rate to the dark state within the trapping cycle (see Fig. 4.1) is low. This concomitantly requires a high extinction ratio of the repumper laser within the dark region — or even a ‘depumper’ laser resonant with  $F = 3 \rightarrow F' = 3$  (see Fig. 4.1) — if population is to be shelved within this dark state. It was not possible to obtain the precise alignment of the repumper to overlap the spot images along each axis, since

the chamber geometry required the repumper to share a long common beampath with the trapper. Thus no improvement to the molecular ion signal was observed in this case. Were sufficient optical access to be available for a separate repumper beampath, however, a dark SPOT MOT might yet improve the signal (indeed, the technique was found to be beneficial in a different experiment [101]).

### MOT capture simulations

In order to elucidate the atom capture process and its dependence on various physical parameters, the dynamics of atoms of a range of initial velocities under the influence of the MOT fields were calculated. In the interests of tractability the calculations were effected for a two-level atom (and thus were only accurate for trapper detunings much less than the hyperfine  $F' = 3 \rightarrow F' = 4$  splitting of 121 MHz), and were constrained to motion in one dimension. The region of interaction with the cooling light was defined by the Gaussian intensity profile of the transverse beam clipped according to the size of the optics. The results of these calculations, presented below, were used to aid the design of the new MOT apparatus.

The atoms' motion evolved according to the sum of the scattering forces from the counter-propagating MOT beams,

$$F = F_{\sigma^+} + F_{\sigma^-}, \quad (4.1)$$

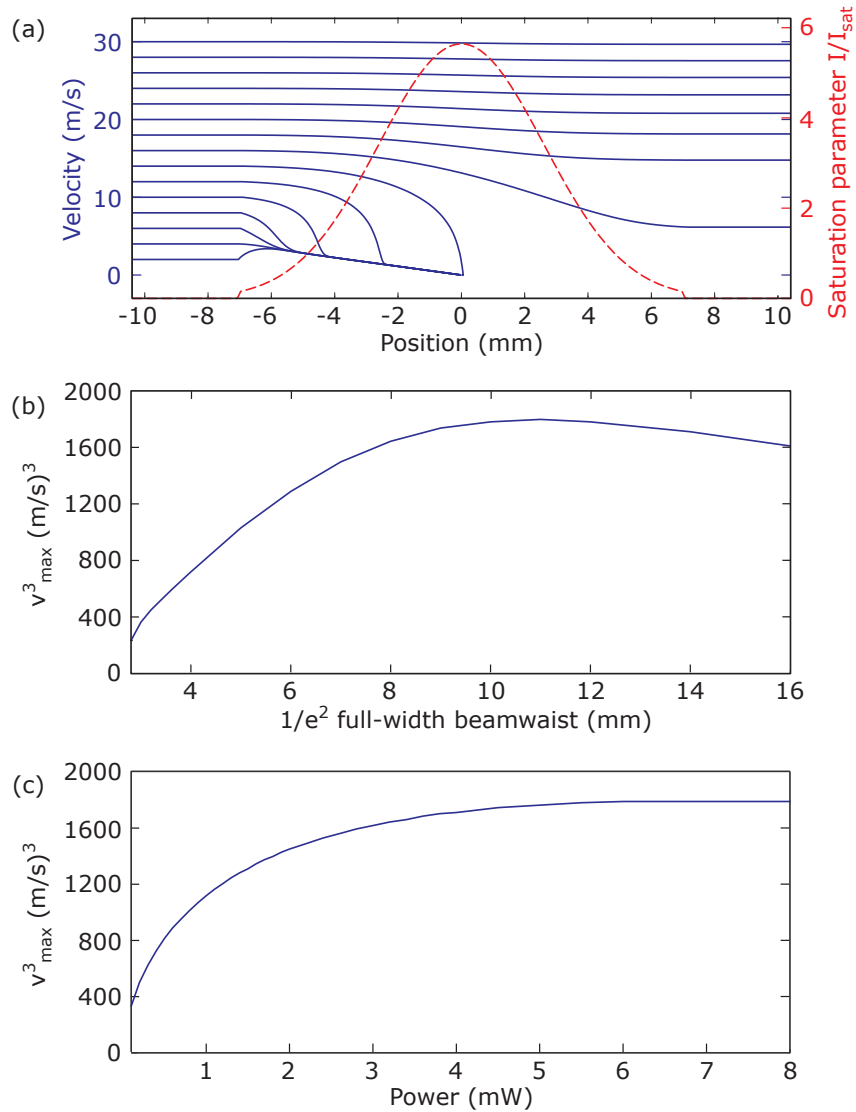


**Figure 4.4** Simulations of the dynamics of atoms captured in the MOT. (a) The evolution of the velocities and positions of atoms of a range of initial velocities, calculated under typical MOT conditions (blue, solid). Slow moving atoms are trapped whilst faster atoms pass through the MOT. The cooling interaction is assumed to take place over a region defined by the clipped Gaussian intensity profile of the transverse beam (red, dashed). (b) The dependence of the cube of the maximum capture velocity,  $v_{\text{max}}^3$ , on beamwaist for the parameters given in the text. (c) The dependence of  $v_{\text{max}}^3$  on trapper power for the parameters given in the text. The increase in  $v_{\text{max}}$  saturates at powers of around 8 mW per beam.

where

$$F_{\sigma^\pm} = \frac{\hbar k \Gamma}{2} \frac{I/I_{\text{sat}}}{1 + I/I_{\text{sat}} + (2\delta_\pm/\Gamma)^2} \quad (4.2)$$

and the atoms experience an effective detuning according to their position  $x$  and velocity  $v$  of

$$\delta_{\sigma^\pm} = \omega - \omega_0 \mp \frac{\mu_B B'}{\hbar} x \mp kv. \quad (4.3)$$

Here  $\omega$ ,  $k$  and  $I$  are respectively the trapper frequency, wavevector and intensity,  $\Gamma$  and  $\omega_0$  are the transition linewidth and frequency,  $B'$  is the magnetic field gradient,  $I_{\text{sat}}$  is the saturation intensity,  $\mu_B$  is the Bohr magneton and  $\hbar$  is the reduced Planck constant [37].

Typical dynamics obtained under these calculations are presented in Fig. 4.4(a). The evolution of the velocities and positions of atoms of a range of initial velocities is shown for realistic experimental conditions, together with the intensity profile of the cooling light that defined the interaction region. Atoms with initial velocities below 14 m/s are captured by the MOT.

The atomic speeds of the background vapour will be distributed according to the Maxwell–Boltzmann distribution,

$$P(v) = 4\pi \left( \frac{m}{2\pi k_B T} \right)^{3/2} v^2 \exp \left[ \frac{-mv^2}{2k_B T} \right], \quad (4.4)$$

which scales as  $P(v) \sim v^2$  for  $\frac{1}{2}mv^2 \ll k_B T$ . Thus the total number of atoms with speeds within the maximum capture velocity,  $v_{\text{max}}$ , scales as  $\int_0^{v_{\text{max}}} P(v) dv \sim v_{\text{max}}^3$ .

The dependence of  $v_{\max}^3$  on beamwaist,  $w$  (defined as full width at  $1/e^2$  intensity) was thus calculated [Fig. 4.4(b)]. The total power per beam and trapper detuning were set as 8 mW and -15 MHz respectively in accordance with typical experimental conditions after the installation of the slave (Section 4.2.1). At relatively small waist sizes, the saturation of the scattering force in Equation 4.2 results in a steady gain in capture velocity with beam size due to the increase in interaction region. At larger waist sizes, the scattering force is no longer saturated by the ensuing low intensities. The capture velocity (which scales as  $v_{\max}^2 \sim \frac{2Fw}{m}$  for atom mass  $m$ ) decreases with increasing waist size due to the  $w^{-2}$  dependence of the intensity and the limitation of beam clipping on the interaction region. Though the simulations indicate a larger optimum, a beamwaist of 6 mm was employed, as any further increase using available optics was found to have a negligible impact on the size of the MOT.

Though increasing the trapping power would increase the capture velocity indefinitely with a corresponding increase in beamsize, these practical beamsize limitations result in diminishing returns for excessive trapper powers. The behaviour of  $v_{\max}^3$  as a function of total trapping power was thus calculated in order to determine a fruitful goal for the slave laser system [Fig. 4.4(c)]. The calculations revealed that the increase in  $v_{\max}^3$  with trapper power is fully saturated at around 8 mW per beam. Operating within this saturated regime is desirable, both in terms of optimizing the MOT size and providing some immunity of atom number to minor fluctuations in trapping power.

### 4.3 Pulsed laser systems

The experiments preceding those reported herein regarding the coherent control of ultracold molecules using ultrafast pulses [27, 93] were conducted using a commercial oscillator (Spectra Physics Mai Tai). A description of the apparatus and related pulse-shaping and characterization technology have been described in an earlier thesis [135]. Within this previous work, shaping of the spectral intensity was effected by a zero-dispersion  $4f$  line, whilst large positive chirps of the order of  $10^5 \text{ fs}^2$  were applied via multiple passes through a dispersive glass block. In addition to these techniques, a commercial acousto-optic programmable dispersive filter (AOPDF) (Fastlite Dazzler) was available within the laboratory [160].

It was decided to transfer subsequent experiments to a Ti:sapphire regenerative chirped-pulse amplifier (CPA) laser system [161, 162] that also resided within the laboratory. The CPA system produced 90 fs, 100  $\mu\text{J}$  pulses with an 18 nm full width at half maximum (FWHM) bandwidth at a repetition rate of 2 kHz. The phase and amplitude of the CPA pulses was deduced using spectral phase interferometry for direct electric field reconstruction (SPIDER) [163]. The system had been designed to operate at the relatively red central wavelength of 840 nm in order to be suitable for an experiment with hot  $\text{K}_2$  molecules [164, 165]. In particular, the amplifier cavity end mirrors were treated with an anti-reflection coating designed to suppress the peak of the Ti:sapphire gain bandwidth at 800 nm.

The detection of ground-state molecules was implemented using a pulsed, tunable dye laser (Sirah Cobra) that was pumped with the second harmonic of a Q-

switched Nd:YAG laser (Spectra Physics Quanta Ray LAB-130-50). A mixture of Rhodamine B and 101 dyes was employed, producing 9 ns pulses at 50 Hz, with wavelengths tunable in the range of 598-636 nm and with typical pulse energies of the order of 1 mJ. The use of this laser for a resonant multi-photon ionization (REMPI) detection scheme will be discussed in more detail in Sections 5.1 and 7.2.

### 4.3.1 Modifications

Earlier experiments revealed a coherent quenching of the background population by chirped ultrafast pulses [27, 93], detected via a REMPI scheme using nanosecond pulses after sufficient time for decay to the ground state. These results motivated the pump-probe experiments described in Chapter 6, where ionization was effected directly from the excited state in order to probe the dynamics therein. The probe pulses were therefore required to be short in comparison to the dynamical timescales. To serve this purpose, a non-collinear optical parametric amplifier (NOPA) was constructed using the second harmonic of the CPA as the pump [166]. The NOPA provided a tunable source of broadband photons within the range 480–720 nm. Typical NOPA parameters for the pump-probe experiment were a bandwidth of 15–20 nm at 500 nm central wavelength and a pulse energy of 4  $\mu$ J. An intensity autocorrelation measurement indicated a pulse duration of 390 fs.<sup>7</sup> Figure 4.5(c) shows a typical spectrum together with this autocorrelation measurement. A long-pass filter with a 480 nm cut-off removed spectral intensity that would contribute to a resonant

---

<sup>7</sup>Note that a long  $\beta$ -barium borate (BBO) crystal was employed for the autocorrelation measurement in order to derive a measurable signal in the second harmonic. The indicated pulse duration must therefore be considered to place an upper limit on the true value.

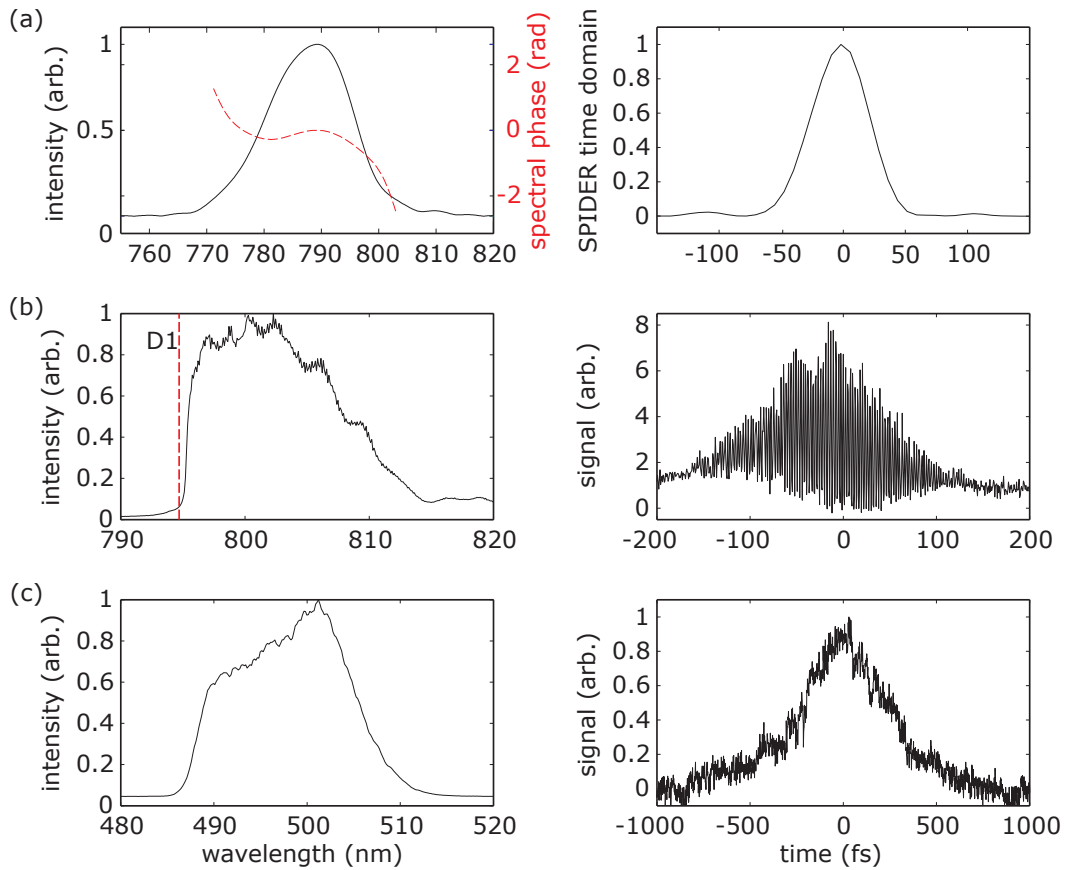


**Figure 4.5** Spectral (left) and temporal (right) form of the ultrafast laser pulses. (a) The spectral intensity and phase of the CPA pulses used to generate the pump and probe, together with a SPIDER reconstruction of the temporal pulse form. The pulses were centred at 790 nm with 20 nm bandwidth, and were of 53 fs duration. (b) A typical pump-pulse spectrum (filtered at the  $D_1$  line by the pulse shaper), together with an interferometric autocorrelation measurement indicating a pulse duration of 85 fs. (c) A typical NOPA probe pulse spectrum (filtered at 480 nm) revealing 20 nm bandwidth pulses at 500 nm, together with an intensity autocorrelation measurement indicating a 390 fs pulse duration.

ionization of rubidium atoms.

For the pump-probe experiments described in Chapter 6, the CPA served as the source of the pump pulse. Early attempts at the pump-probe experiment were able to achieve a molecular ion signal with the NOPA and an unshuttered MOT,<sup>8</sup> but not with the CPA, NOPA and a shuttered MOT. It was apparent that this signal was attributable to the formation of molecular ions from either excited-state atom pairs in the trapping cycle, or loosely bound excited-state molecules that had been formed through photoassociation by the trapping light. The failure of the CPA to excite any population that could be detected by the NOPA was attributed to the CPA's red central wavelength: the Franck-Condon factors for photoassociation fall away rapidly with detuning from the atomic asymptote, and so the pump pulse was not able to photoassociate a wavepacket with sufficient efficiency. It was therefore necessary to modify the CPA system to restore its central wavelength closer to the spectral region of highest photoassociation efficiency. The principal changes involved replacing all the custom-coated optical elements with versions with a standard broadband antireflection coating, and realigning the oscillator to restore its central wavelength to 790 nm. As a result, the modified CPA produced 200  $\mu\text{J}$  pulses with a 20 nm FWHM bandwidth. The pulse duration was 53 fs FWHM when optimally compressed. The spectral phase and intensity of the CPA system after this modification are shown in Fig. 4.5(a) together with the SPIDER reconstruction of the pulse form in the temporal domain.

---

<sup>8</sup>Conventionally, the trapping light was shuttered for a few microseconds prior to the arrival of the photoassociation pulse, in order to allow all atomic population to decay to the ground state.

A new pulse shaper was constructed for the pump-probe experiments based upon a zero-dispersion  $4f$  line (1200 lines/mm diffraction gratings separated by twice the 75 cm focal length of the spherical mirrors) with a resolution of 0.1 nm (as determined by the beam waist in the Fourier plane and the  $4f$ -line dispersion). The pulse pulse could be spectrally filtered by this shaper by means of razor blades placed within its Fourier plane. The position of the spectral cut was set to eliminate excitation of unbound excited-state population above the  $5S + 5P_{1/2}$  atomic asymptote [see Fig. 4.5(b)]. The pump-pulse bandwidth could be restricted by means of a second razor blade. Interferometric autocorrelation indicated pulses of 85 fs FWHM duration.

The pump pulse was next passed through a variable delay line: a retroreflecting mirror was positioned on a stage controlled by a motorized actuator (Newport LTA-HS interfaced with a Newport ESP300 Motion Controller). Positive pump-probe delays of up to 250 ps were employed, corresponding to a translation of the stage of 3.75 cm due to the double-pass configuration. It was then combined with the probe using a dichroic mirror, and the beams were focussed onto the MOT with a 20 cm focal-length lens. The reference point for zero delay was identified using sum-frequency generation between the pump and probe pulses in a BBO crystal.

Some new dye solutions were trialled with the dye laser in order to gain access to different ground-state detection schemes. The dyes and corresponding tuning ranges were Rhodamine B (588-614 nm), Pyridine 1 (667-720 nm) and Styryl 8 (712-782 nm). The REMPI scheme employed for ground-state molecular spectroscopy is

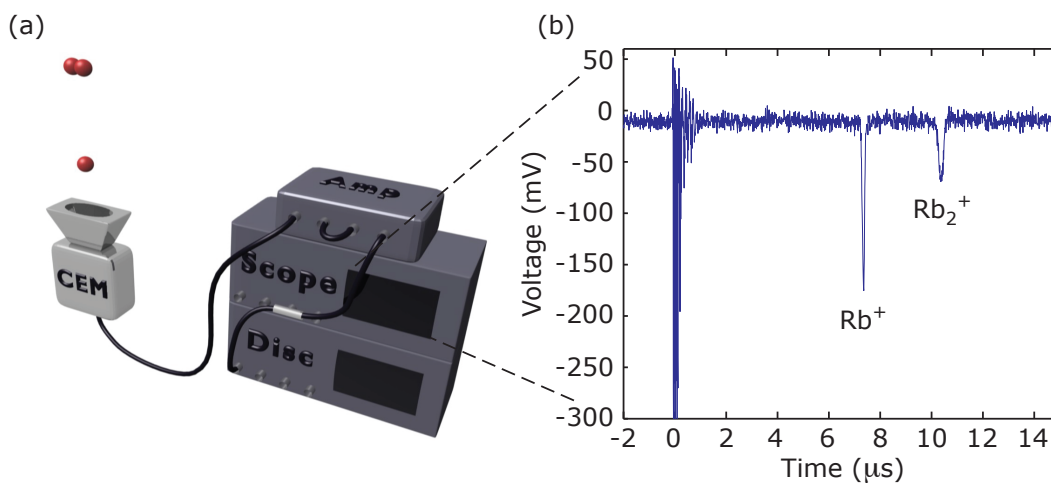


**Figure 4.6** The TOF detection scheme. (a) Atomic and molecular ions are attracted towards a negative high voltage at the entrance to a CEM detector. The signal passes through two stages of a broadband preamplifier (Amp) and is monitored on an oscilloscope (Scope). The  $\text{Rb}_2^+$  signal is discriminated and recorded on a multi-channel scaler (Disc). (b) A typical TOF trace for the detection of ground-state molecules. Molecular ions arrive a factor of  $\sqrt{2}$  later than the atomic ions due to their greater mass. The spike at 0  $\mu\text{s}$  is electrical noise caused by the firing of the flashlamps for the dye pump laser.

outlined in Section 7.2. An alternative pump laser (Big Sky) was appraised, but the inferior transverse mode quality resulted in damage to the dye cuvette.

#### 4.4 Detection scheme

Detection of  $\text{Rb}_2$  molecules in their ground and excited states was effected via a range of ionization mechanisms discussed later in this thesis (Sections 5.1 and 7.2). Though the schemes were designed in order to ionize molecules preferentially over atoms, they nevertheless produced many atomic ions via off-resonant routes due to the intrinsic inefficiency of the molecular formation processes and consequent

relative paucity of molecules. The atomic and molecular ions were therefore resolved and distinguished via time-of-flight (TOF) mass spectrometry: a -2.2 kV bias voltage attracted them to the front face of a channel electron multiplier (CEM) (Dr. Sjuts Optotechnik KBL 408) positioned beneath the MOT. The CEM signal passed through two stages of a broadband pre-amplifier (Stanford Research Systems SR445), each with an amplification factor of 5. This arrangement is illustrated in Fig. 4.6(a). The amplified signal [see Fig. 4.6(b)] was monitored on a 500 MHz oscilloscope (Tektronix TDS744A). The experimental sequence was synchronized using a digital delay-pulse generator (Berkeley Nucleonics BNC555).

#### 4.4.1 Modifications

The pump-probe experiments of Chapter 6 gave rise to a much greater  $\text{Rb}^+$  ionization signal than the old pump-decay experiments. This was due to the much greater peak intensities of the pulses concerned: the pump-pulse energies were typically two to three orders of magnitude larger, and the NOPA ionization pulse was four orders of magnitude shorter than the dye pulse. Furthermore, the NOPA operating wavelength was sufficient for two-photon, off-resonant ionization of ground-state atoms, whereas three photons were required for the dye ionization scheme. Consequently, this enhanced TOF  $\text{Rb}^+$  signal heavily saturated the preamplifier, such that the  $\text{Rb}_2^+$  signal arrived on the sloping tail of the  $\text{Rb}^+$  signal. Even in the absence of amplification, the  $\text{Rb}_2^+$  signal nevertheless arrived within the recovery time of the CEM from the saturating  $\text{Rb}^+$  signal. A typical averaged pump-probe TOF trace

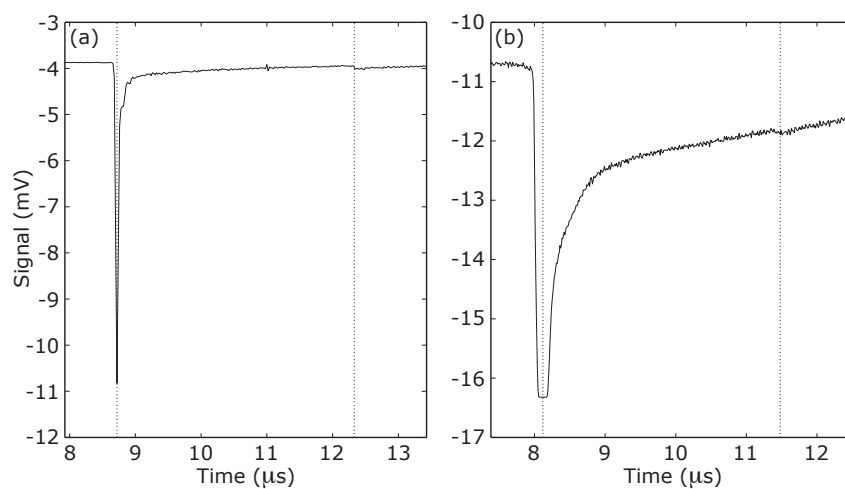


**Figure 4.7** Typical TOF traces for the pump-probe experiment obtained with the CEM detector: (a) without and (b) with the SR445 preamplifier. The locations of the atomic and molecular ion signals are marked with dotted lines. A much larger atomic ion signal is obtained than with the ground-state dye detection scheme. As a result, the amplified signal is heavily saturated. The molecular ions arrive on the tail of the atomic ion signal, rendering the signal harder to extract. This saturation effect is also seen to a lesser extent in the unamplified signal. These plots show the average of 10,000 traces.

with and without amplification is shown in Fig. 4.7.

The recovery time of the CEM after saturation by the atomic ions is attributable to the time taken to replenish the charge within the channel after the pulse. This is determined by the capacitance and resistance of the channel, and is typically of the order of 0.1 – 10 ms. The effects of saturation observed in both the unamplified and amplified CEM output, and the consequent arrival of the molecular ion signal on a sloping background, rendered this signal harder to extract and introduced noise into the measurement. This effect was particularly severe for the amplified output; meanwhile the small molecular signal size was at the limit of resolution of the signal integration procedures discussed below in Section 4.5.

It was therefore decided to replace the CEM with an multi-channel plate (MCP) (Photonis APD HT APTOF 18 6/5/12 AU 4.5"FM-2.75"FM). An MCP is another kind of electron multiplier ion detector and comprises a large number of microchannels distributed over a large surface area [167]. Individual MCP channel recovery times are typically of the same order as for CEM detectors, depending on the particular electrical characteristics. If the incident ions are independently distributed over the majority of the  $10^5 - 10^6$  channels, however, the effective recovery time may nevertheless be much faster.

The front face of the MCP was electrically grounded. Thus the ions were pushed towards the detector by means of a positive voltage applied to a wire mesh situated opposite the MCP inside the vacuum chamber. The sensitivity of the detection was changed by varying the voltage from 100 V to 1100 V: a high voltage ensured

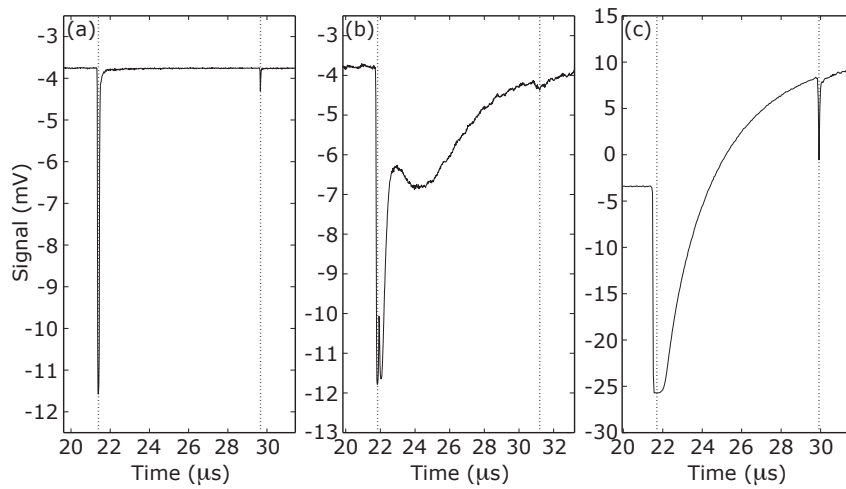


**Figure 4.8** Typical TOF traces for the pump-probe experiment obtained with the MCP detector: (a) without amplification, (b) with the SR445 preamplifier, and (c) with the Ortec 9326 preamplifier. The locations of the atomic and molecular ion signals are marked with dotted lines. The recovery time of the MCP is faster than that of the CEM, and the unamplified  $\text{Rb}_2^+$  signal arrives on a flat background in the absence of amplification. With either preamplifier, however, the  $\text{Rb}_2^+$  signal arrives during heavy ringing following the saturation of the amplifier by the  $\text{Rb}^+$  signal. These plots show the average of 10,000 traces.

sensitive detection of  $\text{Rb}_2^+$  whilst a low voltage ensured a linear response to  $\text{Rb}^+$  without MCP saturation.

The MCP was trialled with both an unamplified output and in conjunction with either the old SR445 broadband preamplifier or a newly acquired Ortec 9326 preamplifier. It was also found worthwhile to switch the pushing voltage from 0 V to the high voltage  $3.3 \mu\text{s}$  after ionization. This provided for an expansion of the ion cloud that reduced the impact of saturation within the central MCP channels by distributing the ions over a greater detector surface area [168]. This modification produced a useable molecular signal from the unamplified MCP output. The molecular ions arrived at the detector within a time window narrower than 100 ns. Typical averaged TOF traces are shown in Fig. 4.8. As before, the atomic ion signal produces a saturation effect in the TOF trace, with the result that the molecular signal is amplified but falls on a sloping background during the amplifier recovery period. The MCP was more sensitive to the molecular signal than the CEM, however, such that a much more visible unamplified signal is obtained. Furthermore, the MCP recovery time is observed to be significantly faster than that of the CEM.

## 4.5 Signal processing

Data were accumulated using a multi-channel scaler (Stanford Research Systems SR430), which discriminated the ion signal with respect to a user-defined threshold in order to compile a histogram of ion counts per time bin. The multi-channel scaler could also operate in an external ‘toggle’ mode, whereby a differential histogram

could be compiled dependent on the action of a chopper wheel (Stanford Research Systems SR540) on a photoassociation pulse. The purpose of this strategy was that data could slowly be accumulated over many shots of the ionization laser whilst preserving immunity to a slow signal drift due to factors such as alignment. Finally, the histogram compiled by the multi-channel scaler was loaded into the experimental control computer, and the signal was integrated over the time bins defined by the user.

#### 4.5.1 Modifications

As explained above in Section 4.5.1 and illustrated in Figs. 4.7 and 4.8, saturation of the amplified TOF signal by the atomic ions had the deleterious effect of adding a variable sloping background to the molecular signal. It was therefore no longer possible to use the multi-channel scaler in conjunction with an amplified TOF signal, as the discriminator could not sensibly be set. An alternative approach was to acquire averaged TOF traces from the oscilloscope; however, hardware processing overheads prevented every successive experimental trigger from contributing to the running average. The rate depended on the length of the acquired trace, but the optimum was no better than one averaged shot in every ten.

A couple of approaches were tested that used ‘boxcar’ gated integrators (Stanford Research Systems SR250) to extract the molecular signal from this background at the 2 kHz repetition rate of the laser system. Two channels were available that could each integrate the input signal electronically within the duration of a user-

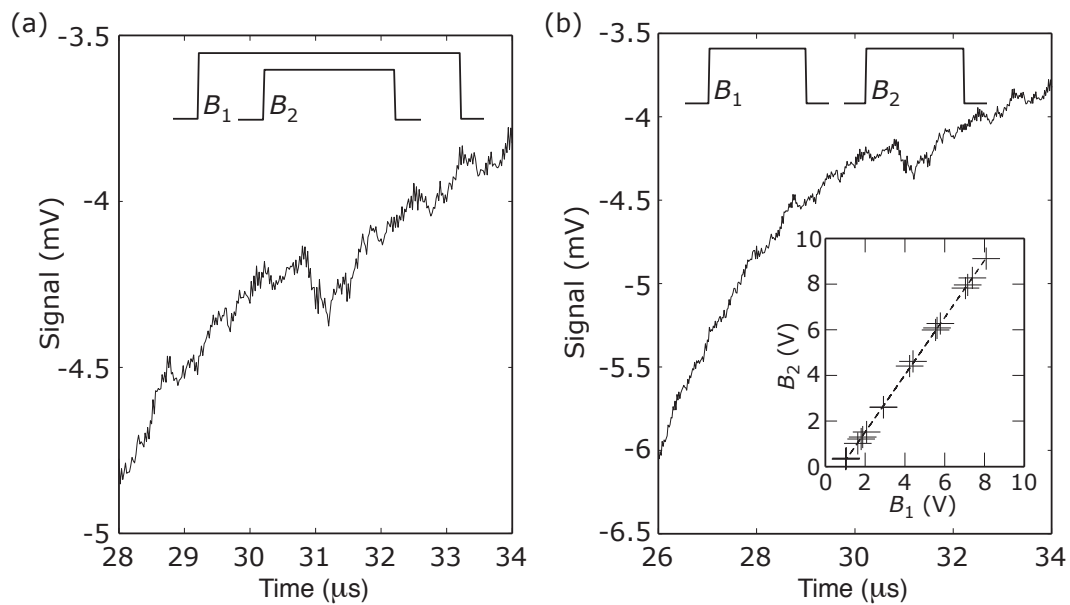


**Figure 4.9** The two approaches to a background-compensated molecular signal measurement using the boxcar integrators  $B_1$  and  $B_2$ . (a) The boxcar windows are both centred on the signal, with the width of  $B_1$  twice that of  $B_2$ . Under the approximation that the background is linear, the integrated background-free signal is given by  $S = 2B_2 - B_1$ . (b) The boxcar windows are positioned side by side, with  $B_2$  centred on the signal. The dependence of  $B_2 = f(B_1)$  in the absence of a molecular signal is calibrated (inset). The background-free signal may be calculated using this calibration as  $S = B_2 - f(B_1)$ .

defined window. Under the first approach, the first boxcar window,  $B_1$ , was set to twice the width of the second,  $B_2$ , and both were centred on the molecular signal [see Fig. 4.9(a)]. Under the approximation that the background was linear over the width of  $B_1$ , the integrated molecular signal,  $S$ , could be calculated according to  $S = 2B_2 - B_1$ . Some trial pump-probe measurements taken with this technique, however, were reasonably noisy, with shot-to-shot variations of the order of 20%. Molecular signals extracted in this manner were numerically analyzed for a series of sample TOF traces. ‘True’ signals were calculated by fitting a polynomial function to the background tail and numerically integrating the signal within a window. The ‘experimental’ signals were compared to these ‘true’ values, with discrepancies found of up to 50%.

Under the next scheme, the boxcar windows were instead positioned side by side, with the second boxcar centred on the molecular signal [see Fig. 4.9(b)]. A linear relationship was discovered between the backgrounds at the two locations, provided that the atomic signal did not heavily saturate the detector. This relationship was calibrated before the experiment in the absence of a molecular signal: the CPA alone was used to produce off-resonant atomic ionization, and the two boxcar readings were logged for a range of different powers. A typical calibration appears as an inset to Fig. 4.9(b). This calibration,  $B_2 = f(B_1)$ , was used to subtract an appropriate background from the molecular signal, according to  $S = B_2 - f(B_1)$ .

The discovery (detailed above in Section 4.4.1) that an initial free expansion of the ion cloud produced a useable  $\text{Rb}_2^+$  signal from the new MCP detector without

external amplification reopened the possibility of using the multi-channel scaler to accumulate data. A comparison was therefore made of the signal-to-noise ratio obtained with data accumulated via both boxcar and multi-channel scaler approaches. With the boxcars, 2,400 TOF traces at a fixed pump-probe delay were averaged (a process which took 8 seconds). The molecular signals were spread with a standard deviation of 6.4%. Furthermore, a constant drift on the potentiometer voltage that set the zero reference caused a systematic error. A similar process was carried out using the multi-channel scaler to count molecular ions from 2,000 TOF traces (which also took 8 seconds). The standard deviation for this method was 6.0%. However, a reduction in the number of data points logged by the oscilloscope shortened the acquisition time by approximately a factor of three. Due to this faster acquisition and the lower errors, it was therefore decided to use the multi-channel scaler for acquisition of TOF traces resembling Fig. 4.8(a) during the pump-probe experiments.

Another potential source of noise on the molecular pump-probe signals was the fluctuation of the NOPA that served as the probe. Typical fluctuations in power of 5% were observed over the timescale of a second. The dependence of the molecular signal on the NOPA power was therefore catalogued prior to an experimental run. Typical behaviour is shown in Fig. 4.10. A linear dependence was observed (commensurate with the single-photon transition effected by the probe) until saturation, when no further increase in signal with power was forthcoming. Although data could, in principle, be normalized to NOPA power within the linear regime, in

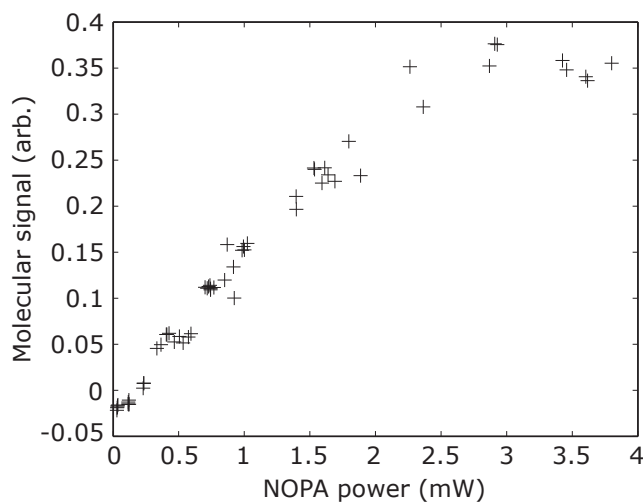


**Figure 4.10** A typical dependence of the molecular signal size on the NOPA probe laser power. A linear dependence is observed at lower powers that saturates at higher powers. The best experimental results were obtained when sufficient NOPA power was available for operation within this saturated regime.

practice these smaller signal sizes gave a poorer signal-to-noise ratio. It was consequently found that the best data were obtained without normalization but with the use of saturating NOPA powers.

As a further measure, for each pump-probe delay measurement, the  $\text{Rb}^+$  or  $\text{Rb}_2^+$  TOF signal was averaged 1,000 times and integrated numerically (taking around 6 seconds) at each delay. This ensured that the duration of the single-point averaging was greater than that of the characteristic NOPA power fluctuations but shorter than the long-timescale drifts of the MOT conditions. The signal-to-noise ratio of the pump-probe signal was further improved without compromising sensitivity to these long-term drifts by averaging several successive pump-probe scans.

## 4.6 Summary

This chapter has described the experimental apparatus used to conduct the experiments detailed elsewhere within this thesis. During the ground-state experiments of Chapter 5 and the preliminary attempts at the pump-probe experiments discussed in Chapter 6, it became apparent that certain technical limitations of the apparatus were hampering progress. The description of these exigent modifications to the MOT, pulsed laser systems, detection and signal processing has been afforded this separate chapter.

The photoassociation experiments were all conducted within the ultracold environment of a rubidium MOT. Stability issues within this MOT were addressed through improvements to the design, reducing the day-to-day alignment burden as a result. These modifications were guided by simulations of the dynamics of atoms captured by the MOT. A redesign of the ultrafast system was necessary to obtain sufficient spectral intensity at efficient photoassociation wavelengths, and a NOPA was constructed in order to allow the excited state to be probed.

The pump-probe TOF signals exhibited significant atomic ionization that saturated the pre-amplifier and occluded the molecular ion signal. Though various schemes were trialled to extract this signal, the problem was ultimately addressed through a change in detector and the introduction of a period of free expansion of the ion cloud. This engendered a more prominent molecular ion signal that rendered further amplification unnecessary; in this manner the saturation issue was avoided. Care was also taken to ensure that the probe-pulse energy was sufficient to escape

the linear regime of signal gain. This offered some immunity to the short-timescale NOPA fluctuations that were endemic to the apparatus.

## Chapter 5

# Quenching of ground-state molecules

*The Warrior of Light has the sword in his hands.*

Early attempts to apply ultrafast, sub-picosecond photoassociation pulses to a rubidium MOT observed the effect of chirped and transform-limited pulses on the population of background triplet molecules [27, 94]. A combination of photoassociation by the trapping light and three-body recombination were believed to contribute to this population. This is the subject of further study within Chapter 7, where MOT photoassociation is found to be the dominant mechanism within this experimental setup.

The ultrafast pulses were found to *reduce* the background population, rather than form new ground-state triplet molecules that were visible to the REMPI de-

tection scheme. The quenching effect was described to be coherent in nature: the positively chirped pulses engendered a greater quenching effect than their transform-limited counterparts. Despite this unexpected result, there was considered to be cause for optimism regarding the prospects of ultrafast photoassociation for cold molecule formation. The nature of the quenching alluded to coherent excitation channels through which background population is dissociated. The application of linear chirps to the control pulse represents a very limited subspace of the parameter space that could in principle be explored; a closed-loop control optimization would offer a more promising and thorough approach to the design problem. Such an algorithm, however, requires the control field to produce a positive effect for optimization: indeed, early attempts at a genetic algorithm by Brown *et al.* converged on a zero-amplitude control field as the optimum pulse for minimum quenching [135]!

These initial results of the author's predecessors were obtained using a femtosecond oscillator as the photoassociation laser. Typical pulse energies were 0.3 nJ at an 80 MHz repetition rate. By contrast, the amplified CPA system is capable of producing 200  $\mu$ J pulses at a 2 kHz repetition rate. The motivation for transposing the pump-decay experiments to an amplified ultrafast system is as follows. Firstly, the higher pulse energies produced by the amplified system increases the pathway flexibility through the prospects of multiphoton transitions to higher-lying potentials and Stark shifts. Furthermore, despite the high repetition rate of the unamplified ultrafast system, the ground-state detection was only implemented at 50 Hz. Subsequent ultrafast pulses would therefore act to quench any population photoassociated by

the preceding pulses. At the 2 kHz repetition rate, however, the nascent molecules would have sufficient kinetic energy to drift outside the volume addressed by the photoassociation laser during the interval between pulses. Trading off a lower repetition rate for a higher pulse energy would therefore increase the effective molecular formation rate. This slower repetition rate also allows the population to decay to the ground state between ultrafast pulses. Finally, it is compatible with an existing AOM pulse-shaping apparatus. The update rate of an AOM is limited by the transit time of the radio-frequency wave through the crystal (around  $10 \mu\text{s}$ ); the slower repetition rate of the CPA allows shot-to-shot updated waveforms.

## 5.1 Detection scheme

For the ground-state experiments, the population occupying the  $a^3\Sigma_u^+$  triplet potential was detected using REMPI followed by TOF mass spectrometry, as outlined in Section 4.4. The REMPI pathway is illustrated in Fig. 5.1. A two-photon process preferentially ionized the  $\text{Rb}_2$  via a resonant intermediate potential, while atomic ionization followed an off-resonant pathway and required an extra photon. The pathway employed loosely bound vibrational states within the  $(2)^3\Pi_g$  potential as the intermediate [59].

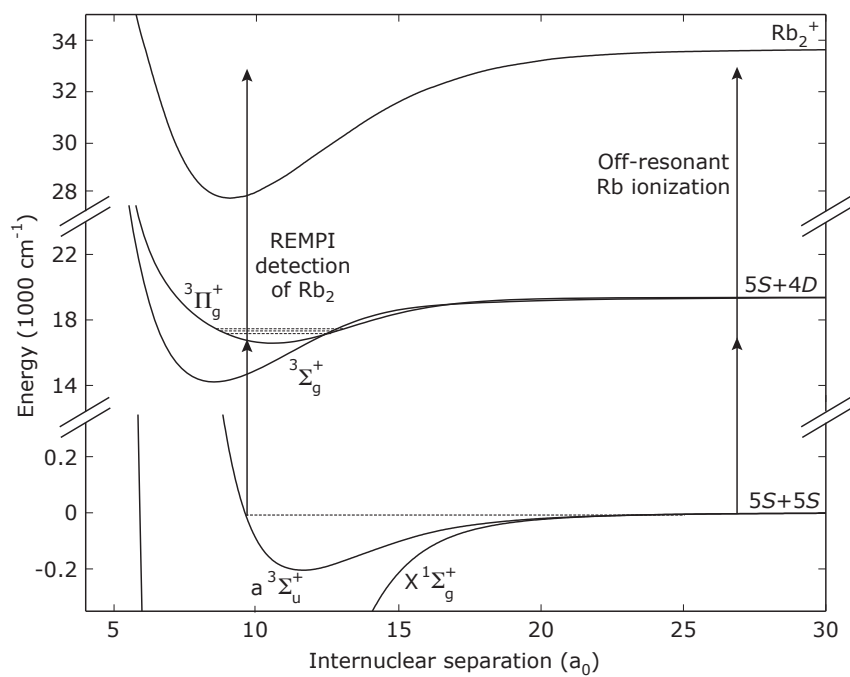


**Figure 5.1** The REMPI ground-state detection pathway. The ‘background’ triplet molecules may be detected via a two-photon resonant ionization pathway via deeply bound states within the  $(2)^3\Pi_g$  potential. Atomic ionization proceeds via an off-resonant, three-photon process.

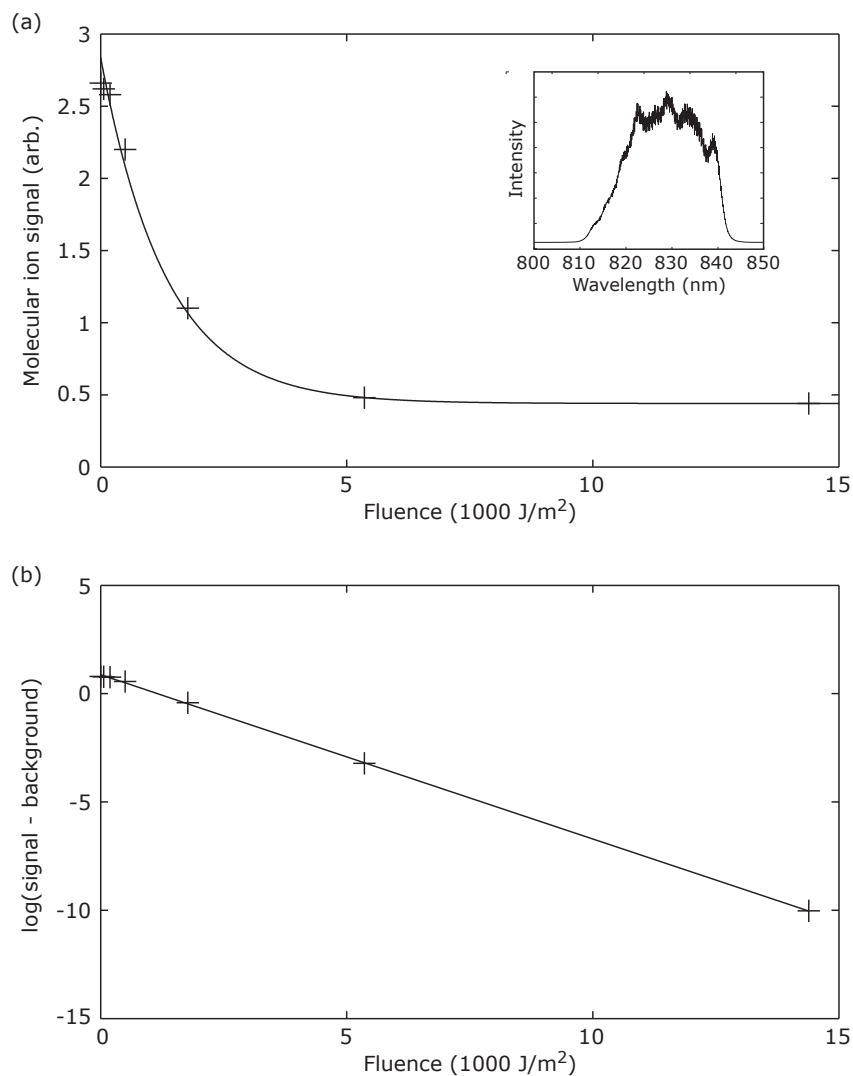


**Figure 5.2** (a) Molecular ion signal versus CPA pulse fluence, together with an exponential fit. At the 2 kHz repetition rate of the ultrafast system, the molecules may be expected to interact with only a few pulses before drifting out of the interaction region. The strong depletion of the background molecular signal at the fluences within this plot demonstrate the applicability of the strong field regime. The pulse spectrum is inset. (b) A logarithmic plot confirms the data to be well described by an exponential decay curve. The decay constant is found to be 1320 J/m<sup>2</sup> and the residual signal at large fluences is 0.44.

## 5.2 Ground-state quenching with amplified ultrafast pulses

As discussed above, the quenching effect on the background molecules observed by Brown *et al.* represented the cumulative impact of a train of unamplified ultrafast pulses preceding the ionization pulse (see Fig. 2 of Ref. [27]). The circumstances surrounding the analogous experiment with the amplified ultrafast system are altered by the slower repetition rate: a given molecule would only be expected to interact with a very small number of pulses before it drifted out of the beam.

A measurement was therefore made of the quenching of the molecular ion signal as the fluence of the CPA pulses was varied with attenuation by neutral-density filters. The results are shown in Fig. 5.2(a), together with the CPA pulse spectrum. A fitted exponential decay, with the decay constant and vertical offset<sup>1</sup> as fitting parameters, was found to be in close agreement with the data [see Fig. 5.2(b)]. This exponential decay of the molecular ion signal with pulse fluence is consistent with the earlier experiment. The significant depletion of the background molecular signal at single-pulse fluences of the order of  $1000 \text{ J/m}^2$  demonstrate that the strong-field interaction regime applies.

The experiment of Brown *et al.* observed quenching over peak intensity scales that imply a pulse fluence of the order of  $0.02 \text{ J/m}^2$ . During the millisecond timescale over which the molecule is expected to remain within the interaction region, 40,000 oscillator pulses arrived — compared to a single CPA pulse. The cumulative pulse fluence over this timescale is therefore comparable for both experiments.

---

<sup>1</sup>The unsuppressed background signal at large fluences is attributed to imperfect overlap between the spatial modes of the ultrafast and detection beams.

### 5.3 Quenching with chirped pulses

A further experiment was conducted to investigate the effects of a linear chirp upon the quenching of the ground-state molecular ion signal. The experiments of Brown *et al.* reported a heightened quenching effect for a positively chirped oscillator pulse; this experiment sought to extend this study to the amplified pulse regime. The CPA system pulse compressor was used to generate the chirp: the grating-grating separation was scanned using an automated actuator. The power of the beam was measured to be independent of compressor position [Fig. 5.3(a)]; this demonstrated that the pulse energy was not influenced by the choice of chirp. On the other hand, the pulse energy of the blue light that could be generated via second-harmonic generation (SHG) in a nonlinear BBO crystal was maximal for an optimally compressed pulse. This measurement identified the zero-chirp compressor position.

The molecular quenching rate as a function of linear chirp is shown in Fig. 5.3(b). The quenching appears to be independent of chirp, though noise levels as high as 15% are observed for an acquisition of 10,000 shots. This is in contrast to the observation of Brown *et al.* that a chirped pulse induced a greater quenching effect. However the level of noise is sufficiently high that any subtleties of the quenching behaviour would be likely to be occluded. The 10,000 shots that were averaged for each data point on the plot each took several minutes to acquire. Over this timescales the instabilities in the MOT and the pointing of the CPA beam were not insignificant. These stability issues therefore needed addressing in order to advance the experiment.

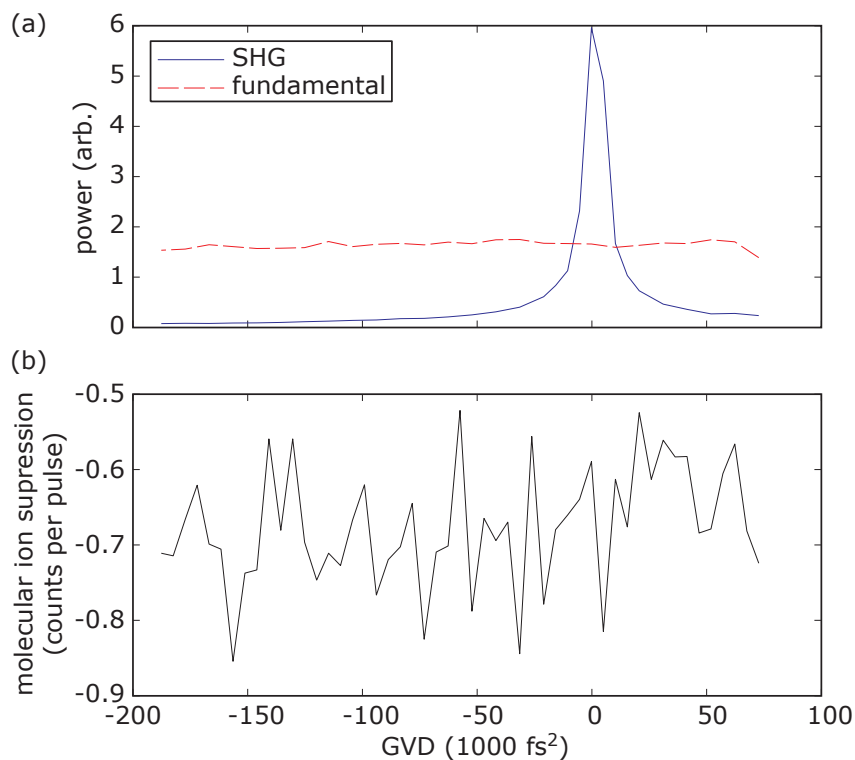


**Figure 5.3** The impact of a linearly chirped ultrafast pulse on the suppression of the ground-state molecular ion signal. The chirp was generated by scanning the grating separation within the CPA system pulse compressor. (a) The power was measured as a function of chirp (fundamental), together with the power of the second harmonic generated in a nonlinear crystal (SHG). The former was independent of grating position but the latter was maximal for an optimally compressed pulse. This plot therefore demonstrates that a constant pulse energy was applied, and identifies the zero-chirp position. (b) The suppression of the molecular ion signal as a function of pulse group velocity dispersion (GVD).

## 5.4 Summary

A previous experiment studied the impact of ultrafast pulses on the ground-state molecule population within a  $^{85}\text{Rb}$  MOT. They were observed to reduce the signal, indicating that the pulses were exciting pre-formed molecules to dissociative channels, rather than associating fresh atom pairs. A positively chirped pulse produced a heightened quenching effect compared to its transform-limited counterpart. This experiment applied pulse trains of low energy and high repetition rate; the results of this chapter present preliminary attempts to extend this work to the use of amplified pulses of much higher energy and lower rate.

The slower repetition rate of the amplified system implies that each molecule only interacts with one or a small number of pulses. This was not the case at the higher repetition rate of the unamplified system; however, subsequent pulses would have the opportunity to quench population photoassociated by their predecessors, inhibiting any accumulation effect. Furthermore the higher pulse energies allow the access of multiphoton pathways and broaden the scope for coherent control.

The REMPI ground-state molecular signal was observed to decay exponentially with pulse fluence, consistent with the prior experiments of Brown *et al.* with unamplified pulses. No obvious dependence of the degree of quenching on the linear chirp of the ultrafast pulse was observed, in contrast with these unamplified pulse studies. Improvements were desirable, however, to the stability of the experimental apparatus in order to reduce the relatively high signal-to-noise levels. These improvements have been discussed in Chapter 4.



## Chapter 6

# Pump-probe study of excited-state molecules

*The Warrior of Light studies the two columns on either side of the door  
he is trying to open.*

In response to growing theoretical clamour for the application of picosecond pulsed laser systems to the photoassociation of ultracold molecules, early experimental results first emerged in 2006 [27, 93, 94]. These results found that broadband pulses caused a quenching effect on pre-formed triplet molecules within a rubidium MOT. Though this reduction was naturally not the desired outcome, the coherent nature of the phenomenon intimated that the manipulation of wavepackets with ultrafast pulses nevertheless remained a propitious avenue for exploration. These experiments, which measured the molecular products after the conclusion of a pump-

decay process, however, were not able to elucidate the reaction pathway itself; thus information could not be gleaned about how to harness these effects to *produce* molecules.

It was therefore decided to devise a pump-probe experiment [83, 100] to study the excited-state dynamics in a time-resolved fashion. A characterization of the excited-state dynamics would represent an important step towards the design of a fully coherent ‘pump-dump’ route to deeply bound ground-state molecules. The pump-probe observation of wavepacket oscillations would allow the optimal delay for the application of a dump pulse to be determined. Furthermore, the nature of the oscillations could be manipulated through appropriate phase and amplitude shaping of the pump pulse, offering a potential gain in efficiency for the pump-dump transfer.

Within this chapter, the experimental method is first outlined. Accompanying numerical simulations of the excited-state dynamics (conducted by Hugo Martay at the University of Oxford) are briefly described. They indicate that excited-state oscillations may be expected with reasonable robustness to the experimental parameters and initial conditions. Though theoretical understanding of ionization is less well developed, an operator is conjectured that might mimic the action of the probe pulse, and hence allow a prediction of the experimental ion signal. This pump-probe experiment therefore also offers a test of both the selectivity of this probe with respect to the reaction coordinate and the value of this operator.

These simulations give consideration to two alternative scenarios concerning the

initial state of the atom pairs:

- The pump pulse photoassociates unbound, ultracold atom pairs from within the MOT.
- The pump pulse excites pre-formed ‘background’ molecules that occupy high-lying vibrational states within the electronic ground states.

An analysis of the respective contributions of these scenarios is contained within Chapter 7.

The chapter then presents the experimental results. Under a range of conditions, a molecular pump-probe signal is observed that undergoes a significant step at zero delay; however, Fourier analysis of the ensuing signal reveals no dominant characteristic oscillation periods. The detection of excited-state population is encouraging for the future development of a pump-dump scheme. The lack of observed wavepacket oscillations, however, is in contrast with the few-picosecond timescale dynamics predicted by theory, and implies an insufficient selectivity of the probe pulse. This issue is a further motivation for the initial-state characterization of the next chapter, as bound and unbound populations might be expected to occupy significantly different internuclear separations demanding different probe-pulse designs.

## **6.1 Experimental method**

The ultrafast apparatus used to generate the pump and probe pulses, the MOT that served as a source of cold atoms, and the detection scheme have already been outlined

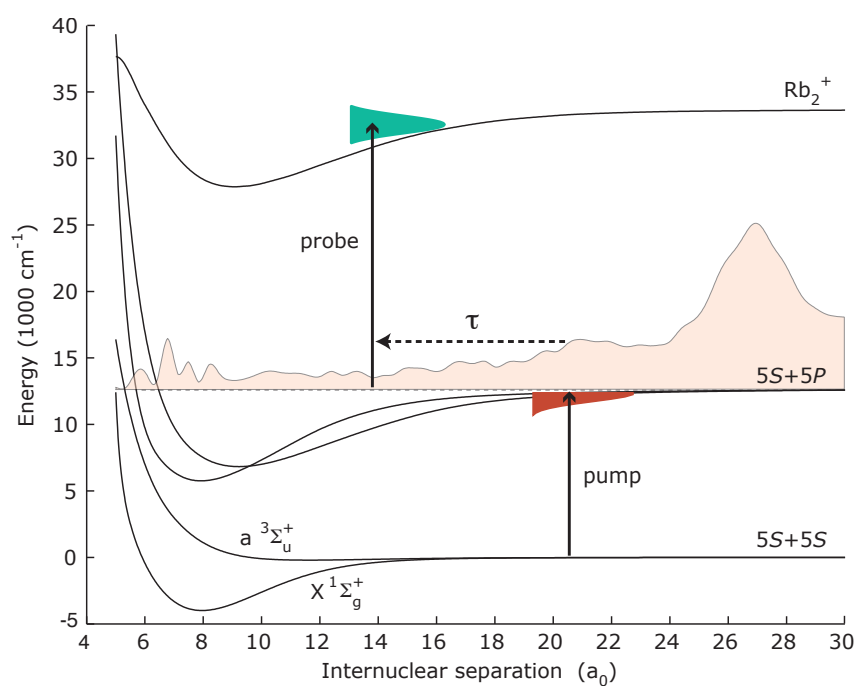


**Figure 6.1** A schematic of the pump-probe experiment. A femtosecond pump pulse photoassociates ultracold  $5S$  ground-state atom pairs, forming a wavepacket spanning a range of vibrational states within the  $5S + 5P$  potential manifold. A typical simulated population distribution is shown (shaded). After a variable time delay  $\tau$ , a probe pulse ionizes the excited-state population in preparation for detection via TOF mass spectrometry.

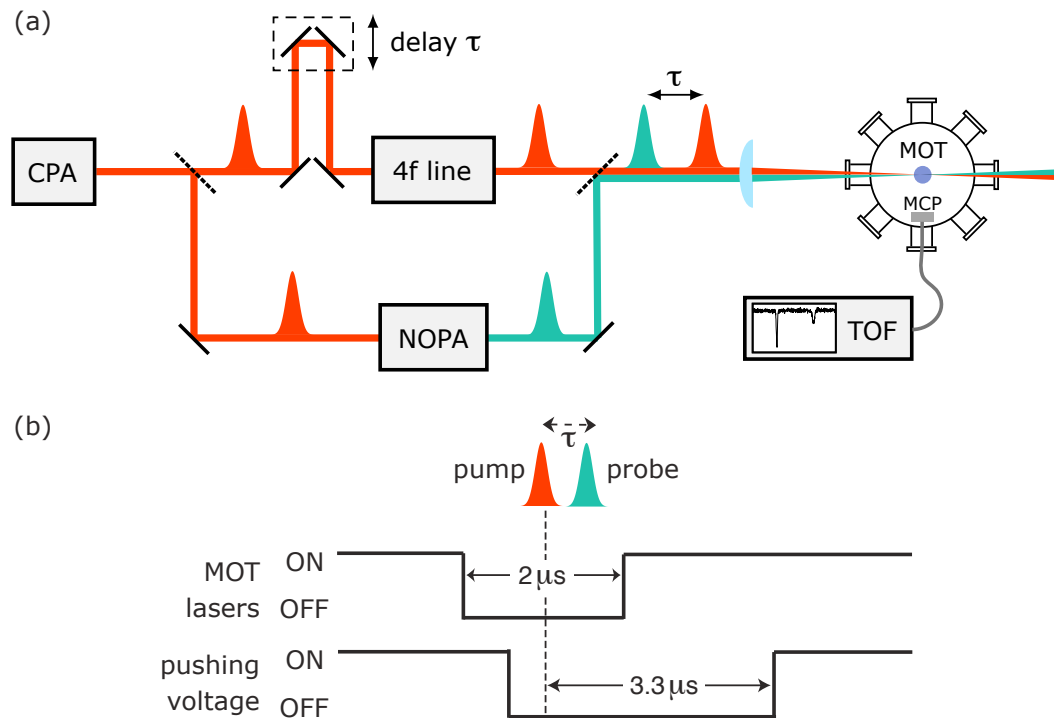


**Figure 6.2** (a) Experimental layout. Pulses from a CPA laser pass through a beamsplitter, with the majority of the pulse energy pumping the NOPA to form the probe pulses whilst the remainder is spectrally filtered in a 4f line and acts as the pump. The pulses are combined with a variable delay  $\tau$  and focussed onto the MOT. Ionized rubidium atoms and molecules are accelerated towards an MCP detector and distinguished via TOF mass spectrometry. (b) A schematic of the experimental timing. The MOT lasers are shut off for a 2  $\mu\text{s}$  window spanning the arrival of the ultrafast pulses. The TOF pushing electrode is switched to a positive voltage 3.3  $\mu\text{s}$  after ionization.

in Chapter 4. Typical pulse spectra and temporal profiles have been given in Fig. 4.5. The transitions involved in the pump-probe experiment are shown in Fig. 6.1, and a schematic layout is given in Fig. 6.2(a). A broadband pump pulse photoassociates ultracold ground-state  $5S$  atom pairs within a rubidium MOT, generating a coherent superposition of vibrational states within the  $5S + 5P$  potential manifold. The pump pulse was filtered within the pulse shaper in order to remove all spectral intensity at frequencies at or above the  $D_1$  line. In this way, the possibility of excitation of unbound excited-state atom pairs was eliminated. The bandwidth of the pump pulse is much greater than the excited-state vibrational level spacing, and so the number of populated vibrational levels is determined by the Franck–Condon factors for the transition.

The excited-state dimer is then allowed to evolve freely during a controllable time delay before being ionized by a broadband probe pulse through a single-photon transition to the ground  $\text{Rb}_2^+$  potential. In order to study the excited-state dynamics over the oscillation timescales of long-range molecules, this pump-probe delay was varied over up to 250 ps. The duration of the broadband probe pulse is short on the timescale of the expected wavepacket oscillations, and thus offers the opportunity for a ‘snap-shot’ measurement of the excited-state distribution.

The efficiency of the photoassociation process is limited by the density of the MOT; hence the  $\text{Rb}_2^+$  ionization rate is exceeded by  $\text{Rb}^+$  ionization despite the off-resonant, multi-photon nature of the latter process. The challenge is therefore to resolve the nascent atomic and molecular ions from the atomic ions with a sensitive

detection mechanism. This was achieved using TOF mass spectrometry with a MCP detector, as outlined in Chapter 4. The TOF electric field was switched on  $3.3 \mu\text{s}$  after the arrival of the pump pulse [see Fig. 6.2(b)]. This provided for an expansion of the ion cloud that increased the signal size. Adjustment of the pushing voltage changed the sensitivity and accommodated the measurement of atomic or molecular ions, as described in Section 4.4.1. In order to ensure that the atom pairs commence the experiment in their ground state, the MOT lasers (which, like the pump pulse, operate on the  $5S \rightarrow 5P$   $D$ -line transition) were shuttered for a  $2 \mu\text{s}$  window spanning the arrival of the pump and probe pulses [see Fig. 6.2(b)].

## 6.2 Numerical pump-probe simulations

As a complement to the experimental study, a colleague conducted numerical simulations of the excited-state dynamics induced by the pump pulse. These simulations distinguished between two different initial-state scenarios for the population addressed by the pump pulse. The intuitive picture of this pump-probe experiment concerns the photoassociation of an unbound pair of ground-state  $5S$  atoms. A corresponding theoretical treatment would therefore consider the evolution of the population excited from an initial  $s$ -wave scattering wavefunction. There are, however, two mechanisms that can contribute a background population of loosely bound ground-state  $a^3\Sigma_u^+$  molecules in the absence of dedicated photoassociation light. These mechanisms are three-body recombination [62] and photoassociation by the MOT lasers [16]. A more detailed discussion of these populations is pre-

sented in Chapter 7, together with an experimental demonstration that the latter mechanism was the dominant background process for this experiment.

A successful experimental implementation of this pump-probe scheme relies on the design of a suitable position-selective measurement of the excited-state population. As discussed above, the experimental scheme uses ionization by a broadband pulse as a probe mechanism. The ionizing action of this probe pulse, however, is difficult to model from a theoretical perspective. An operator that may mimic its behaviour is nevertheless conjectured in order to make a prediction of a likely molecular ion signal.

### 6.2.1 Excited-state population densities

These numerical simulations were repeated for both bound and unbound initial-state scenarios. The time-dependent Schrödinger equation was solved for two different initial density matrices: a thermal distribution of scattering states, and the incoherent mixture of bound  $5S + 5P_{3/2} 0_g^-$  decay products. The details of the coupled-channel model and the numerical implementation are as discussed in Ref. [106], but with the pump pulse selected to match Fig. 4.5(b).

The time- and position-dependent excited-state population densities for both initial-state scenarios are shown in Fig. 6.3. The dynamics due to transitions from the unbound initial state to excited states of both gerade and ungerade symmetries are shown separately; however, dipole selection rules prohibit the population of ungerade excited states from the bound  $a^3\Sigma_u^+$  initial state. These simulations

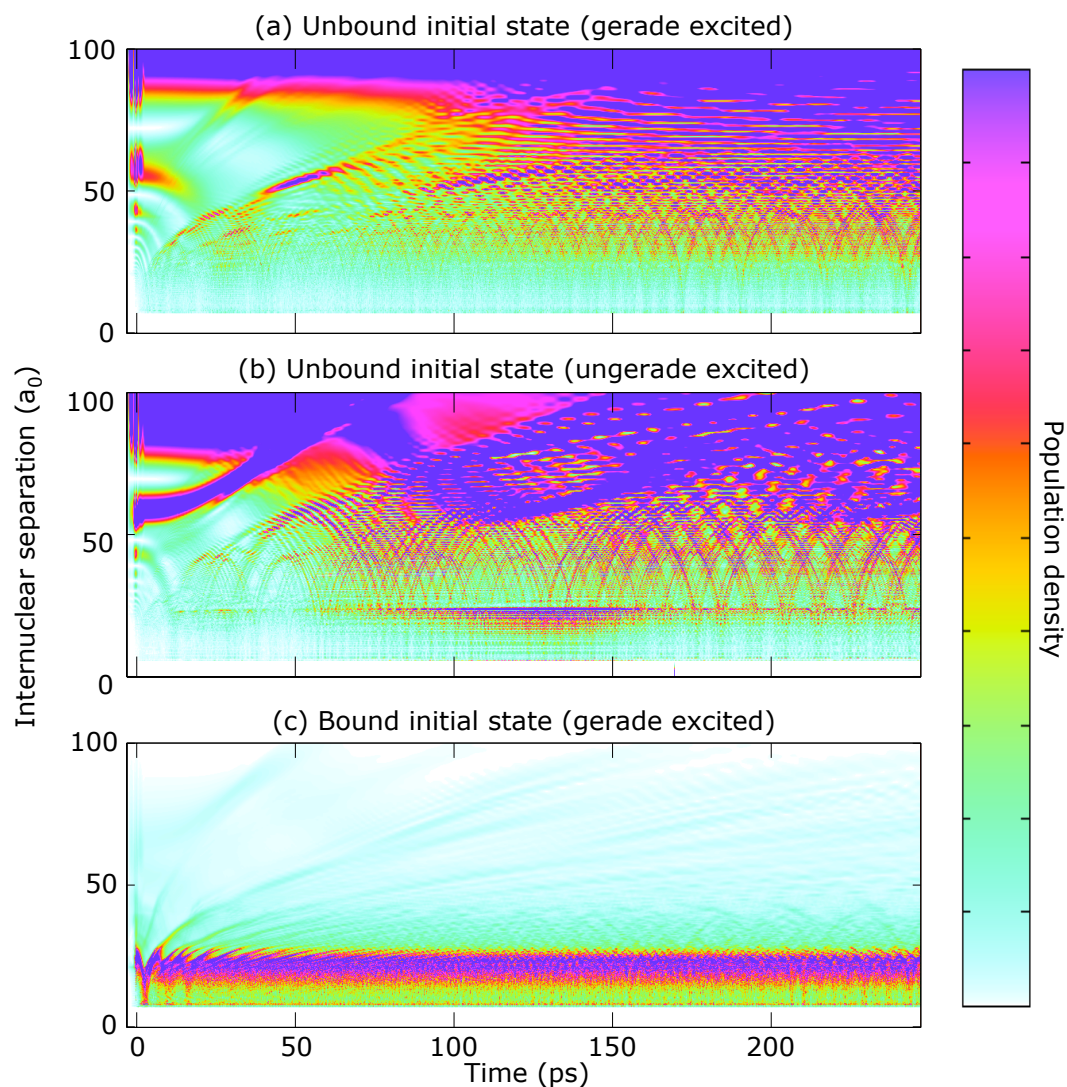


**Figure 6.3** Simulations of the time- and position-dependent excited-state population density induced by the pump pulse. Coherent dynamics occur at a range of internuclear separations (represented by the dark shaded areas) despite the incoherence of the initial states. Results are shown for transitions from an unbound initial population to both gerade (a) and ungerade (b) excited states, as well as from a bound initial population to gerade excited states only (c) (single-photon transitions to ungerade states are prohibited from the  $a^3\Sigma_u^+$  potential).

predict a time-varying internuclear separation distribution due to the evolution of the excited-state wavepacket. Close-range, few-picosecond timescale dynamics occur from the bound initial state, compared to slower and longer-range dynamics from the unbound initial state.

These dynamics are attributable to the fact that the population no longer occupies a time-independent distribution upon promotion to the excited state, since different potential energy curves govern its motion. Localized pockets of excited-state population are created as a consequence of both the nodal structure of the initial state and also the finite-width Franck–Condon window in which the pump pulse acts. The anharmonicity of the excited potential at large internuclear separation precludes harmonic motion, but coherent interference effects still cause oscillations at any internuclear separation. The incoherence of the initial state, whether from thermally distributed scattering states or from preassociated molecules, is not a barrier to the formation of coherently oscillating excited-state population by the pump pulse [106]. This result is a key motivation for conducting this experiment within the impure initial state afforded by the MOT.

### **6.2.2 Ionization signal simulations**

Given these predicted dynamics, a suitable position-sensitive measurement of the excited-state population should therefore produce a time-varying signal. This experiment therefore offers an evaluation of the efficaciousness of single-photon ionization by a broadband probe pulse for this role. There is a much lesser theoretical under-

standing, however, of the action of the probe pulse. A major reason for this is that the Franck–Condon principle, which is used to describe bound-bound transitions, is no longer applicable due to the scope for the ejected electron to carry surplus energy and momentum. The experimental probe pulse described in Section 4.3 is sufficiently short to resolve the predicted dynamics provided that it permits the requisite position-selective measurement.

In order nevertheless to forecast the observed pump-probe dynamics based upon these excited-state calculations, an operator was conjectured to mimic the action of the probe. This operator projected excited-state population onto the  $\text{Rb}_2^+$  potential according to the probe spectral intensity at frequencies sufficient to make that transition energetically viable. The operator simulating the contribution to the  $\text{Rb}_2^+$  signal from the  $j^{\text{th}}$  excited-state potential took the form

$$O_j(R) = \frac{\int_{\omega_{\min}(R)}^{\infty} I(\omega) d\omega}{\int_{-\infty}^{\infty} I(\omega) d\omega}, \quad (6.1)$$

where the lower bound for integration corresponds to the threshold for ionization as a function of internuclear separation:

$$\omega_{\min}(R) = \frac{1}{\hbar} [V_{\text{ion}}(R) - V_j(R)]. \quad (6.2)$$

$V_j(R)$  is the Born-Oppenheimer potential of the  $j^{\text{th}}$  excited electronic state and  $V_{\text{ion}}(R)$  is the ground  $\text{Rb}_2^+$  potential. The spectral intensity distribution of the probe pulse is assumed to be Gaussian with  $\omega_0$  as the central frequency and  $\Delta\omega$  the

FWHM bandwidth in accordance with experimental spectra:

$$I(\omega) = \exp \left[ -4 \ln 2 \left( \frac{\omega - \omega_0}{\Delta\omega} \right)^2 \right]. \quad (6.3)$$

The expectation value of the total operator  $\sum_j O_j(R)$  is shown as a function of pump-probe delay in Fig. 6.4 for both initial states. The Fourier decompositions of the positive-delay signals are also shown. The few-picosecond-timescale excited-state oscillations pertaining to the bound initial state are mapped into corresponding oscillations in the ionization signal. Oscillations are practically absent, however, for the case of the unbound initial state. A possible explanation for this is that the predicted excited-state dynamics from the unbound initial state occurred predominantly at large internuclear separation (see Fig. 6.3): at these separations, the threshold ionization wavelength only varies slightly with separation, and the probe pulse is consequently not position-sensitive.

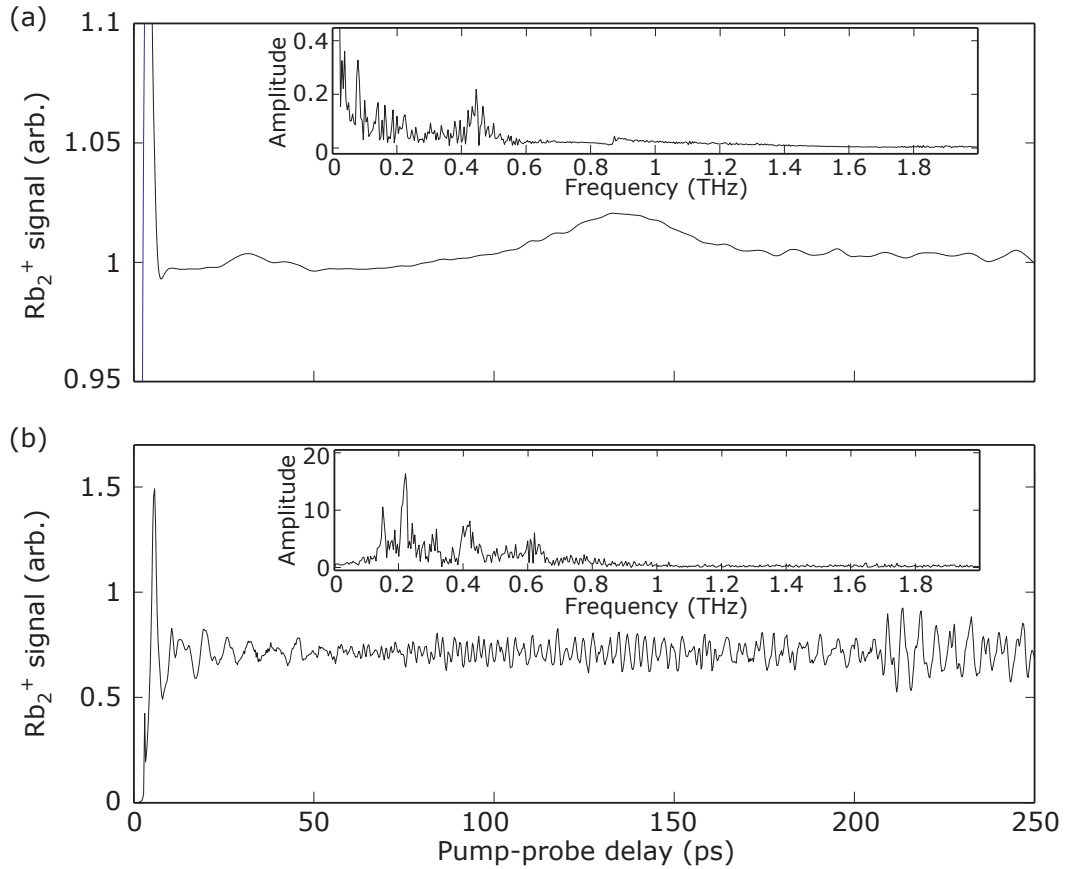
### 6.3 Rubidium pump-probe dynamics

Figure 6.5(a) shows typical atomic and molecular ion signals as a function of pump-probe delay. A low pump-pulse energy of 85 nJ was used in order to allow atomic and molecular dynamics to be monitored simultaneously without excessive atomic ionization. A Fourier transform of the positive-delay molecular ion signal is inset.<sup>1</sup>

Fig. 6.5(b) shows a typical molecular pump-probe signal obtained with the higher

---

<sup>1</sup>The Fourier transform was applied to the positive-delay section of the signal with the d.c. offset removed.



**Figure 6.4** Simulations of the molecular ion signal. The operator  $\sum_j O_j(R)$  (Equation 6.1) is applied to the excited-state population distribution at each pump-probe delay in an attempt to simulate the  $\text{Rb}_2^+$  signal. Results are shown for both (a) unbound, and (b) bound initial-state scenarios. Fourier transforms of the positive-delay signals are shown as insets. Oscillations in the ion signal are much more pronounced for the bound initial state, with characteristic timescales of a few picoseconds. They are negligible for the case of the unbound initial state (note the relative  $y$ -axis scales of the unbound pump-probe plot and Fourier decomposition).

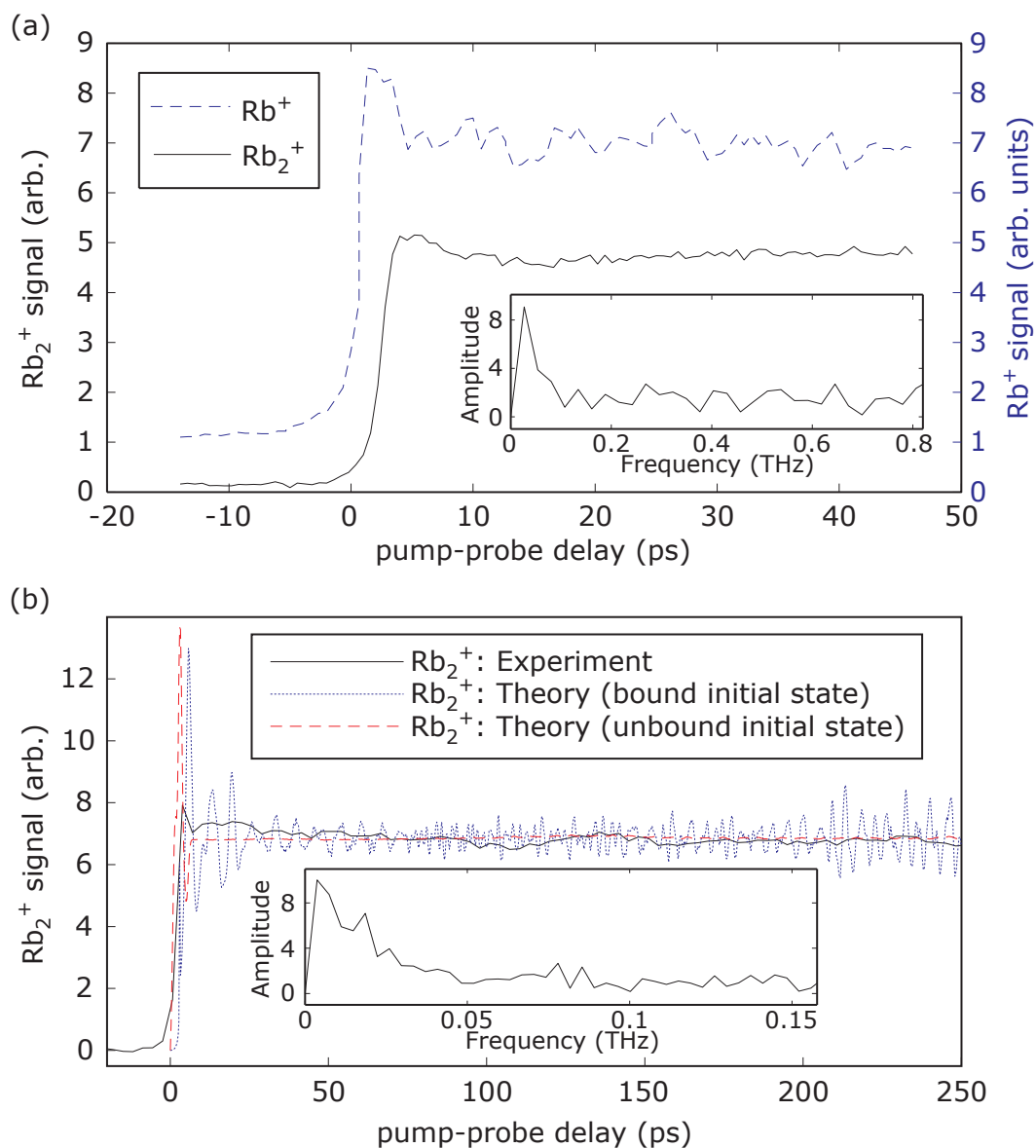


**Figure 6.5** (a) Typical atomic and molecular ion signals as a function of pump-probe delay. The atomic ion signal has been scaled for comparison (though the vertical offset is observed rather than added). Both signals exhibit a step at zero delay and a peak at small positive delays due to transient effects induced by the pump pulse. Fourier analysis of the subsequent positive-delay  $\text{Rb}_2^+$  signal reveals no dominant oscillatory timescales (inset). (b) Experimental molecular ion signals as a function of pump-probe delay for higher pump-pulse energy, together with simulations for bound and unbound initial states. The signals are normalized to have the same step at zero delay. Fourier analysis of the experimental signal again reveals no dominant oscillatory timescales (inset).

pump-pulse energy of 400 nJ, together with simulations of the molecular dynamics for the bound and unbound initial state cases. A Fourier transform of the positive-delay experimental signal is inset. The absolute  $\text{Rb}^+$  and  $\text{Rb}_2^+$  signal scalings employed in the plots are arbitrary, though no offset has been added. The scalings have been chosen such that the signal magnitudes are similar [in the case of Fig. 6.5(a)] and match those of the theoretical simulations [Fig. 6.5(b)].

Both the  $\text{Rb}^+$  and  $\text{Rb}_2^+$  experimental signals show a distinct step at zero delay: the signals are greater for a pump-probe sequential pulse order, though significant off-resonant atomic ionization is still evident with probe-pump timings [Fig. 6.5(a)]. In the  $\text{Rb}_2$  pump-probe experiment of Salzmann *et al.* [101], the sharp spectral cut applied to the pump pulse introduced a long tail into the pump-pulse envelope in the corresponding temporal domain. In exciting an atom pair, the pump pulse induces an electronic dipole which interacts coherently with this long temporal tail, causing oscillations in the excited-state population and hence the  $\text{Rb}_2^+$  signal. This behaviour is similar to the observations of Zamith *et al.* in a Rb vapour cell [103]. These dipole transient effects are not apparent in the long-timescale pump-probe signals of this work due to the employment of a less sharp spectral cut of the pump pulse.

Fourier analysis of the positive-delay signal that follows the coherent transient peak does not reveal any dominant characteristic oscillatory periods. This is in contrast with the picosecond-timescale coherent excited-state dynamics predicted by the simulations (which the probe pulse was short enough to resolve), particularly

for the case of the bound initial state. The calculations of Section 6.2.1 revealed a wide range of conditions under which coherent oscillations may be formed within the excited-state manifold. Though the validity of the operator applied in order to simulate the molecular ion signal is unproven (Section 6.2.2), it indicated that these excited-state dynamics would be observable on the ion signal, particularly for the case of the bound initial state.

It therefore seems likely that the absence of such oscillations in the pump-probe signal can be attributed to an insufficiently position-dependent measurement being effected by the probe, for which there are several likely causes. Firstly, the ionization mechanism of the probe pulse is not as well understood as for the case of neutral-neutral transitions, since the ejected electron may carry extra energy and momentum (as outlined in Section 6.2.1). Furthermore, in order to attain a sufficiently short pulse to resolve the dynamics, a large bandwidth is required which may therefore compromise selectivity with respect to internuclear separation. Other indirect mechanisms, such as autoionization or probe-pulse excitation to neutral Rydberg states that couple to the  $\text{Rb}_2^+$  potential, may also complicate the process. Finally, the detection mechanism may not be sensitive to very long-range excited-state population. At best, it is unlikely to be very position-selective at long range due to the slow variation in the threshold ionization wavelength; the spectral filter applied to the probe pulse (Section 4.3.1) may additionally be compromising the effectiveness of long-range ionization.

Further information is thus required concerning the nature of the initial pop-

ulation addressed by the pump pulse. These issues are further discussed below in Chapter 7.

## 6.4 Summary

In this chapter, the results of a pump-probe experiment into the excited-state dynamics of  $\text{Rb}_2$  molecules were presented together with theoretical calculations. The calculations considered two alternative initial states: unbound atom pairs, and a preformed population of loosely bound molecules. The calculations indicated that coherent oscillations within the excited state may be expected to be induced by the pump pulse for a range of initial conditions. These oscillations were of few-picosecond characteristic timescales for the bound initial state, but were slower and occurred at longer range for the unbound state. A valid theoretical treatment of the ionizing action of the probe pulse is subject to more uncertainty; however, a plausible operator was trialled that described ionization in terms of the threshold wavelength for the transition. This operator predicted an oscillating molecular ion signal that would be significantly more prominent for the bound initial state.

In the experiment, a spectrally filtered broadband pump pulse photoassociated ultracold rubidium atoms, creating a coherent superposition of bound excited states. This excited dimer was allowed to evolve freely for a variable delay before being ionized by a broadband probe pulse. Experimental results showed a prominent pump-probe step; however, the positive-delay signal was relatively flat, and did not contain any dominant characteristic frequencies that might indicate evidence

for wavepacket dynamics. This ability to detect population in the excited state is encouraging for the future incorporation of a dump pulse. The lack of evidence of dynamics within the signal, however, prohibits the design of tailored pulses to control and focus the wavepacket. It is likely that this indicates a lack of probe-pulse selectivity with respect to internuclear separation, such that the excited-state dynamics are ‘integrated out’.

In order to understand the window within which the probe needs to detect population selectively and efficiently, more information about the initial state of the atom pairs addressed by the pump pulse is required. The population densities of bound and unbound initial-state candidates lie predominantly at different internuclear separations, and the ensuing dynamics are expected to be very different. The characterization of relative contributions of these initial states is presented in the next chapter.

## Chapter 7

# Characterization of the initial state

*The Warrior of Light allows the decision to reveal itself.*

The previous chapter presented the results of a pump-probe experiment investigating the dynamics of rubidium dimers promoted to the excited-state manifold by a broadband pump pulse. The predicted dynamics were not evident in the molecular ion signal. The simulations forecast a wide range of conditions under which coherent oscillations may be expected to be induced; however, they also indicated that the initial state of the atom pairs would have a major bearing on the nature and the visibility of the oscillations.

The intuitive picture of this process concerns the photoassociation of a scattering pair of unbound atoms. There are, however, two mechanisms that produce a

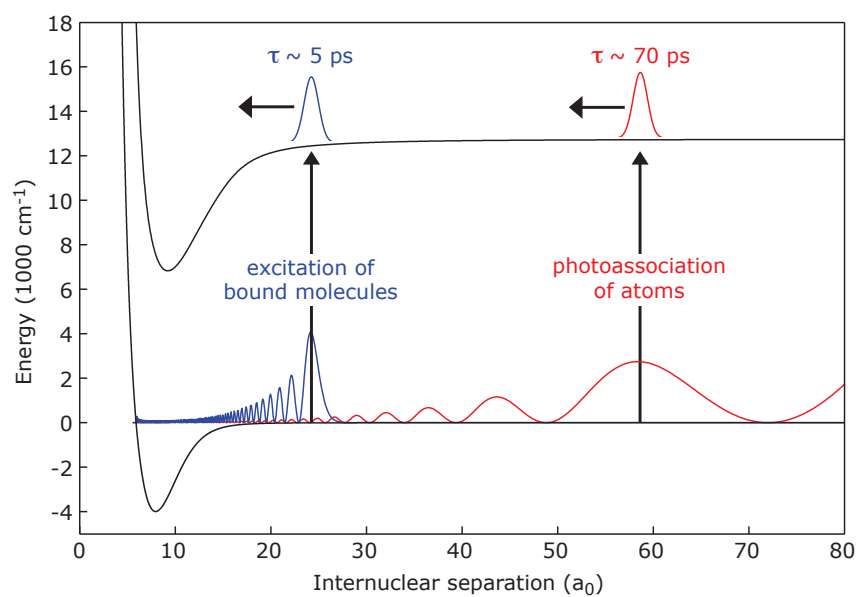


**Figure 7.1** The impact of the initial state on the excited-state dynamics. A wavepacket excited from the penultimate antinode of the scattering state oscillates with a classical period of 70 ps. In contrast, a wavepacket excited from the outer turning point of a loosely bound molecule created by background mechanisms oscillates with the much faster classical period of 5 ps.

‘background’ population of bound molecules that may also interact with the pump pulse: MOT laser photoassociation [16], and three-body recombination [62]. In this chapter, these mechanisms are described, and a spectroscopic measurement of the background molecule distribution within the apparatus is presented. This serves to identify the dominant background mechanism within this experiment, and also highlights the fact that this bound population must be considered as another potential initial state for the pump-probe experiment. This is an important concern, as wavepackets excited at long range from a scattering state will exhibit very different characteristic oscillation times from those excited at shorter range from a bound state (see Fig. 7.1).

The chapter concludes with a discussion of the results of a study of the dependence of the atomic and molecular ion signals on the location of the spectral cut applied to the pump pulse. The atomic ion signal drops off rapidly as the cut is detuned away from the atomic asymptote; however, the molecular ion signal persists for detunings of several tens of inverse centimetres. The discrepancy between their behaviours firstly provides evidence for the formation of bound excited-state dimers. Furthermore, it was possible to fit the experimental data to theoretical calculations in order to determine the distribution of internuclear separations of the initial population. This distribution lies at longer range than the characterized background population, and is consistent with the photoassociation of free atom pairs.

## 7.1 Bound and unbound initial states

The two mechanisms that produce a ‘background’ population of loosely bound ground-state molecules in an  $^{85}\text{Rb}$  MOT in the absence of dedicated photoassociation light are three-body recombination [62], and photoassociation by the MOT trapping light [16]. Experimental studies in  $^{85}\text{Rb}$  have concluded that the former mechanism dominates at low trapping light intensities [59] but that the latter plays a more prominent role at higher intensities [169].

It is possible that these preformed bound ground-state molecules play an important role in the pump-probe dynamics despite their paucity in comparison to unbound atom pairs, since the low MOT atomic density implies a low probability for two neighbouring atoms to interact. A precise characterization of the initial state of the interacting atom pairs is therefore essential for meaningful numerical simulation of the pump-probe process. As shown in the previous chapter, and illustrated schematically in Fig. 7.1, the dynamics of excited-state wavepackets originating from bound and unbound initial states occur on different characteristic timescales, and are concentrated at different internuclear separations.

The formation mechanism effected by the trapping light involves long-range photoassociation to  $5S + 5P_{3/2}$  potentials followed by spontaneous decay to high-lying states within the  $a^3\Sigma_u^+$  ground triplet potential (see Fig. 7.2). Though the  $5S + 5P_{3/2} 0_u^+$  and  $1_g$  potentials are also attractive and coupled to the ground state, the  $0_g^-$  potential is expected to dominate, since it is shallow and purely long-range, and so will offer the most significant Franck–Condon factors for decay from the inner

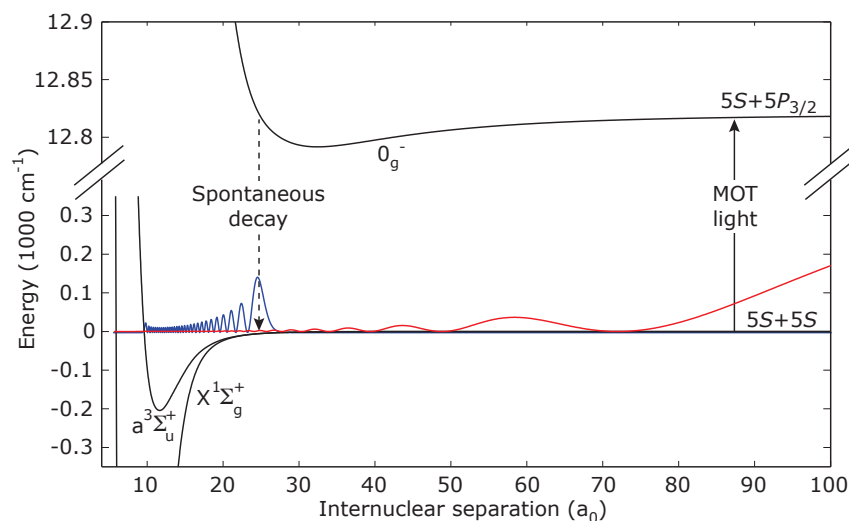


**Figure 7.2** The mechanism for the preparation of a background molecule population by MOT laser photoassociation. The MOT trapping light photoassociates free atom pairs to loosely bound states within the long-range  $5S + 5P_{3/2} 0_g^-$  potential, from where they spontaneously decay to the  $a^3\Sigma_u^+$  ground triplet potential.

turning point to bound ground states.

This photoassociative mechanism is expected to dominate three-body recombination within our setup, as our experimental parameters more closely match the higher intensities of Ref. [169]. In order to test this hypothesis, a comparison of the measured ground-state occupancy to the calculated population distribution resulting from this decay channel is presented below.

## 7.2 Background molecule spectroscopy

The initial distribution of bound ground-state triplet molecules was studied via REMPI. A two-photon process preferentially ionized the molecules via a resonant intermediate potential, while atomic ionization followed an off-resonant pathway

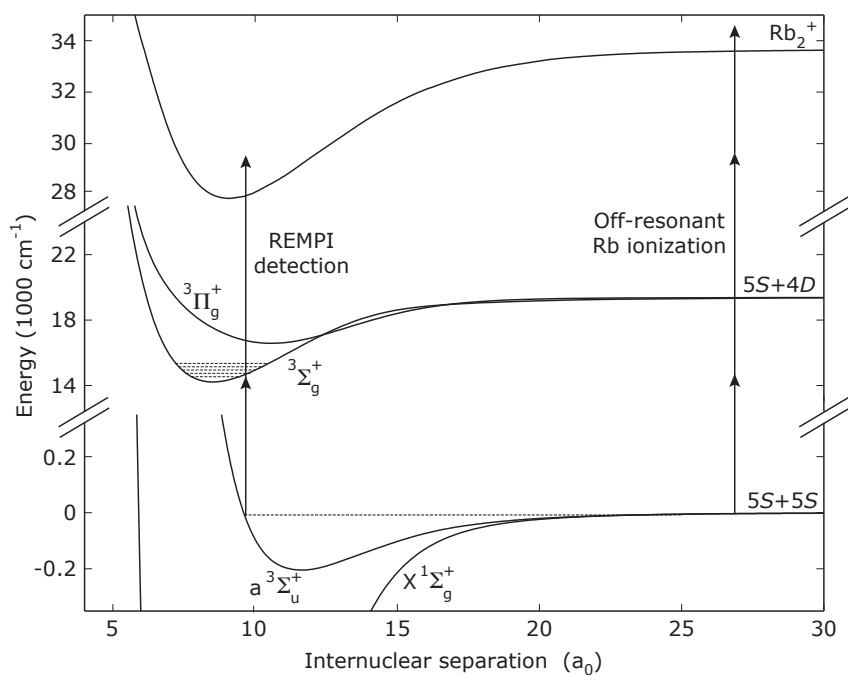


**Figure 7.3** A schematic of the initial-state characterization experiment. The ‘background’ ground triplet molecules may be detected via a two-photon resonant ionization pathway via deeply bound states within the  $(2)^3\Sigma_g^+$  potential. The high-lying populated states within the  $a^3\Sigma_u^+$  ground state are more closely spaced than the deeply bound intermediates within the  $(2)^3\Sigma_g^+$  potential, allowing the ground-state population distribution to be deduced from the resultant spectrum. Atomic ionization proceeds via an off-resonant, three-photon process.

and required an extra photon. A common REMPI pathway for the detection of ground-state triplet molecules employs loosely bound vibrational states within the  $(2)^3\Pi_g$  potential as an intermediate [59], as described in Section 5.1. Since the vibrational level spacings of these initial and intermediate states are comparable, it is not easy to unravel the initial distribution from a spectroscopic measurement via this pathway. Instead, this study uses an alternative REMPI route that passes through more deeply bound levels within the  $(2)^3\Sigma_g^+$  potential (see Fig. 7.3) [170]. The resultant spectroscopic scan enables distinction between the large energy spacing of the intermediate states and the close spacing of the ground-state triplets whose occupancy it is desired to study.

An estimation of the population distribution of molecules photoassociated by the MOT lasers was made by considering the Franck–Condon overlap of high-lying  $0_g^-$  states with each  $a^3\Sigma_u^+$  vibrational state. The expected resultant spectrum for REMPI ionization via the  $(2)^3\Sigma_g^+$  was calculated using the excited-state vibrational level energies given in Ref. [170], together with the corresponding transition Franck–Condon factors. A realistic bandwidth for the REMPI laser was assumed.

The light for the REMPI pathway outlined above was generated with the dye laser using Pyridine 1 dye, with typical pulse energies of up to  $400\ \mu\text{J}$ . The pulse wavelength was tuned between 685 nm and 705 nm through rotation of a diffraction grating within the laser cavity, and was calibrated with reference to two-photon atomic transitions to the  $4p^66d$  configuration (see Table A.2).

Figure 7.4(a) shows the result of a spectroscopic scan of the REMPI ionization

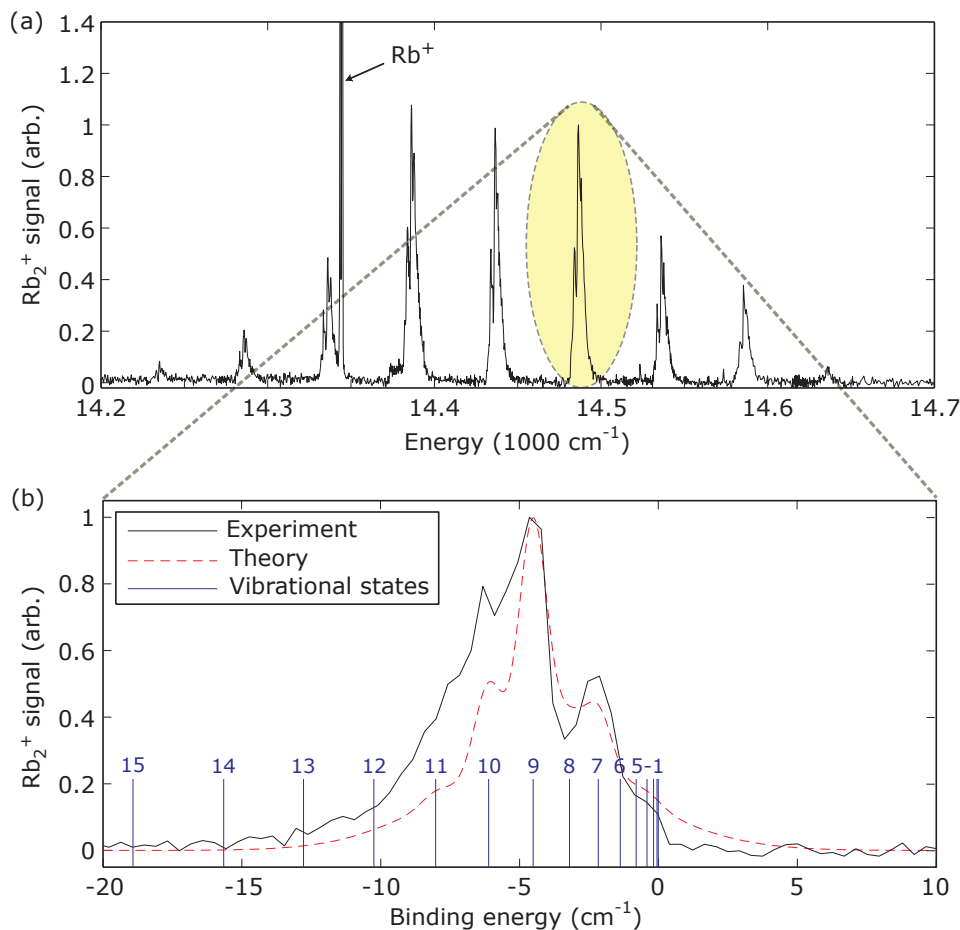


**Figure 7.4** A spectroscopic measurement of the initial state. High-lying vibrational states within the  $a^3\Sigma_u^+$  ground triplet formed through MOT laser photoassociation are ionized using a REMPI pathway through the  $(2)^3\Sigma_g^+$  potential. The  $\text{Rb}_2^+$  signal is shown as a function of ionization energy. (a) The full experimental spectrum reveals the large vibrational level spacing within the  $(2)^3\Sigma_g^+$  potential. The atomic resonance used for calibration is indicated. The overall spectrum is modulated by the tuning range of the ionization laser. (b) A close-up plot of the spectral feature at  $14,500\text{ cm}^{-1}$  reveals the initial population distribution within the  $a^3\Sigma_u^+$ . A close agreement is found with simulations of the population distribution obtained by MOT photoassociation to the  $5S + 5P_{3/2} 0_g^-$  potential. The locations of the highest-lying  $a^3\Sigma_u^+$  vibrational levels are shown and enumerated according to increasing binding energy.

signal from the high-lying ground vibrational states as a function of photon energy. The full spectrum reveals a repeating structure at intervals of  $50\text{ cm}^{-1}$ . This macroscopic structure corresponds to the spacing of the vibrational levels within the  $(2)^3\Sigma_g^+$  excited state (as recorded in Fig. 6 of Lozeille et al. [170]). The detected  $\text{Rb}_2^+$  signal strength is modulated by the available ionization laser pulse energy as the wavelength is tuned. A large peak corresponds to the two-photon resonance in the atomic ionization signal that was used for wavelength calibration.

As discussed above, the microscopic structure within the repeated peaks of the spectrum reveals the  $a^3\Sigma_u^+$  ground-state occupancy. A close-up of the spectral feature around  $14,500\text{ cm}^{-1}$  is shown in Fig. 7.4(b), together with the calculated population distribution formed via MOT laser photoassociation to the  $0_g^-$  potential followed by spontaneous decay. The spectrum is plotted as a function of binding energy in the ground-state triplet potential. The experimental spectrum is in close agreement with a calculation derived from an initial population formed through MOT laser photoassociation via the  $0_g^-$  potential. Photoassociation via the other candidate intermediate potentials would have produced significant population in only the few highest-lying ground vibrational states, resulting in a distinct spectrum. The  $0_g^-$  potential is thus confirmed as the dominant pathway.

The ground-state occupation implied by this background formation mechanism is shown in Fig. 7.5. The greatest population is found to be contained within the ninth-highest vibrational level, which corresponds to the level with the greatest Franck–Condon overlap from the excited state populated by the MOT light. Around

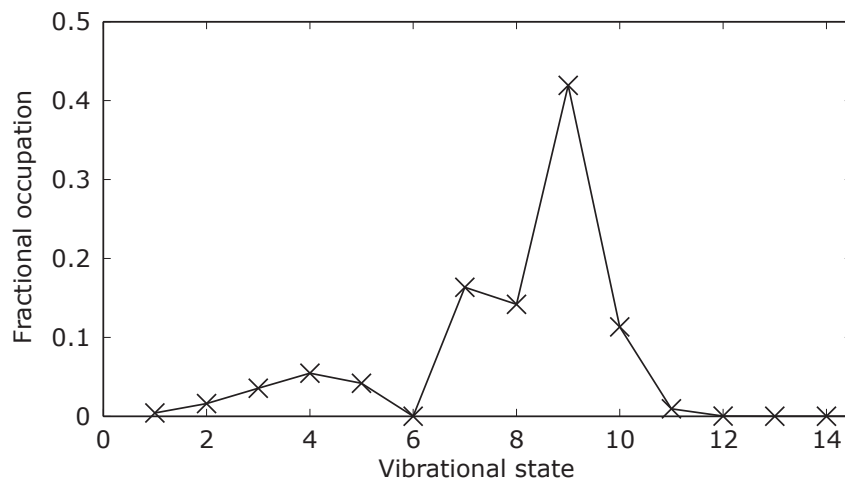


**Figure 7.5** The fractional occupation of the  $a^3\Sigma_u^+$  vibrational states populated through MOT photoassociation via the  $5S + 5P_{3/2} 0_g^-$  potential, as deduced from the theoretical fit to Fig. 7.4(b). The vibrational states are enumerated according to increasing binding energy. The highest occupancy is found for the ninth highest vibrational state; around ten states are populated in total.

ten bound states are found to be populated in total.

The agreement between the experimental and theoretical REMPI spectra confirms that this MOT photoassociation process dominates other mechanisms with regard to the formation of background molecules within this experimental setup. This is consistent with the observations of Caires *et al.* [169], whose experimental parameters are similar to those of this experiment. Were another mechanism to be significant, the observed distribution would be expected to exhibit significant qualitative differences from the calculation. The detection of a strong background triplet molecule signal implies that this bound initial population, additionally to unbound scattering atom pairs, is a candidate for contribution to the photoassociation dynamics. The relative roles of these two candidate initial states in the pump-probe

signal is analyzed below.

### 7.2.1 Bound excited-state dimers

The step in the pump-probe signal at zero delay, together with the linearity of the signal with respect to the pump and probe pulse energies, confirms the pump-probe pathway via the  $5S + 5P$  excited-state manifold (as outlined in Fig. 6.1). The fact that the molecular ion signal was still observed with all spectral intensity at frequencies on or higher than the  $D_1$  atomic transition blocked implies the creation of bound molecular population, rather than coherent transient effects or photoassociation of an unbound  $5S$  and  $5P$  atom to bound molecular ions.

In order to reinforce this conclusion, a further study was performed. A fixed, positive pump-probe delay of 40 ps was selected and the atomic and molecular ion signals were recorded as a function of the position of the pump-pulse spectral cut. The results are shown in Fig. 7.6. As the spectral cut was further detuned from the atomic asymptote (increasing the binding energy of the energetically accessible excited states), the atomic ion signal was observed to fall off more quickly than the  $\text{Rb}_2^+$  signal. Indeed, atomic ion formation reverts to the constant ‘probe-pump’ background levels at detunings beyond  $10\text{ cm}^{-1}$ , while a substantial molecular ion signal persisted. The fast decline in  $\text{Rb}^+$  signal is caused by the loss of spectral intensity resonant with the atomic transition. Hence less atomic population is excited and subsequently ionized. The  $\text{Rb}_2^+$  signal persists, however, due to excitation into bound vibrational levels below the atomic asymptote. The difference between

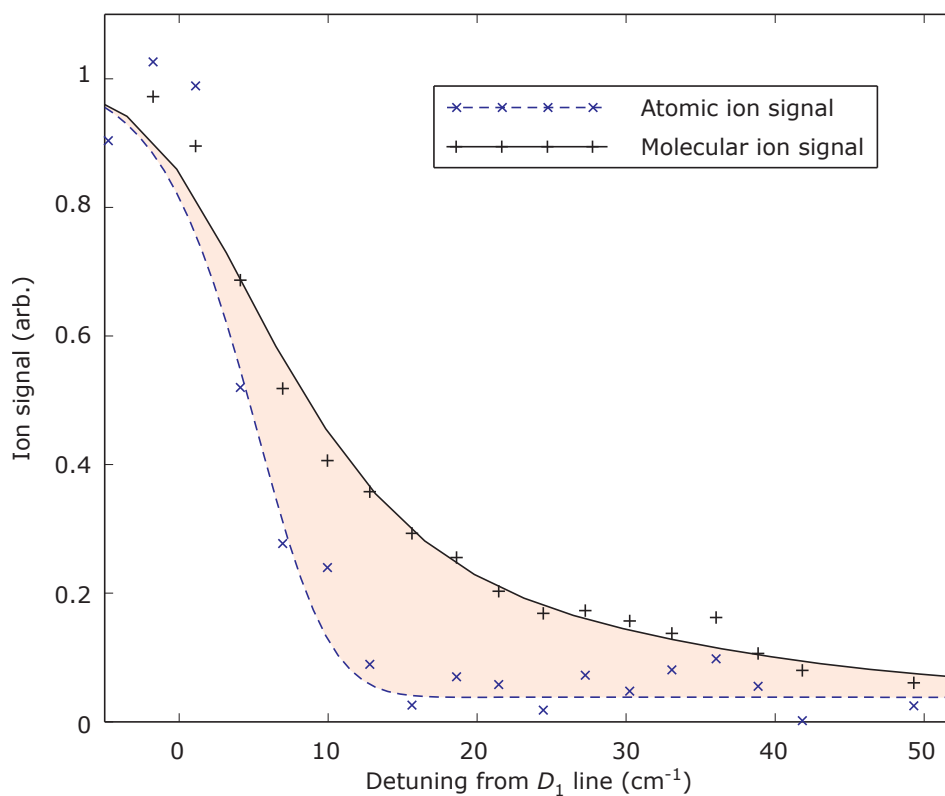


**Figure 7.6** Normalized atomic and molecular ion signals at a fixed pump-probe delay of 40 ps versus detuning of the pump-pulse spectral cut from the  $D_1$  line. The molecular ion signal falls off more slowly than the atomic ion signal with detuning. The shaded area indicates evidence for the formation of bound excited-state dimers.

the  $\text{Rb}^+$  and  $\text{Rb}_2^+$  data series (shaded) therefore provides strong evidence for the formation of bound excited-state dimers by the pump pulse.

As discussed above, there are both bound and unbound candidate initial states that may be the source of this excited-state population. As mentioned, the scattering-state population distribution is predominantly distributed at large ( $R > 50 a_0$ ) internuclear separations, whereas the outer node of the most populated background vibrational state lies at  $25 a_0$ . Though oscillations whose characteristics might have identified the initial state were not evident in the pump-probe signal, the drop-off rate of the molecular ion signal with respect to detuning nevertheless contains information about the nature of the initial state. This is, in essence, a result of the fact that the resonant transition energy is a function of internuclear separation.

Theoretical calculations were accordingly performed of the excited-state population transfer induced by a realistic experimental pump pulse as a function of spectral-cut detuning. This was repeated for a range of initial-state internuclear separations. Thus a series of curves were produced predicting transfer as a function of detuning for a range of different initial separations. The results are shown in Fig. 7.7, together with the  $\text{Rb}_2^+$  experimental data featured in Fig. 7.6 (the red dashed lines show the calculations for initial separations as indicated, and the black crosses show the experimental data). The asymptotic long-range form of the excited-state potentials scales as  $R^{-3}$  due to dipole-dipole interactions, whereas the ground-state potentials scale as  $R^{-6}$  due to van der Waals interactions (see Section 2.1.3). The pump-pulse transition energy therefore becomes more detuned from the atomic asymptote at

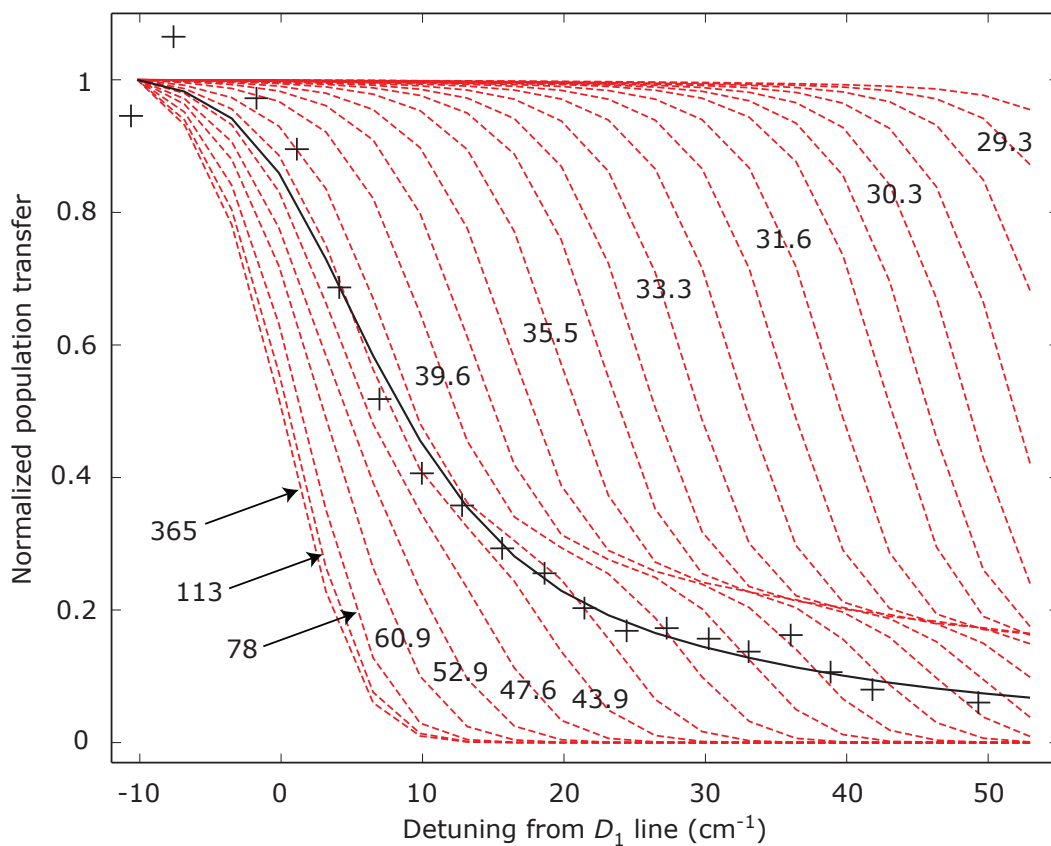


**Figure 7.7** Normalized calculations of the excited-state population transfer induced by the pump pulse versus spectral-cut detuning (red dashed lines). The different series represent initial population at different internuclear separations within the  $a^3\Sigma_u^+$  ground state (labelled in atomic units). The experimental molecular ion signal is plotted together with an optimized theoretical fit for a distribution of initial separations around  $50 a_0$ .

Analytical distribution	Mathematical form	Parameters	Error
Product of two sigmoids	$\frac{1}{1+e^{-\frac{R-a}{b}}} \times \frac{1}{1+e^{-\frac{R-c}{d}}}$	4 ( $a, b, c, d$ )	0.0619
Sigmoid + decaying exponential	$\frac{1}{1+e^{-\frac{R-a}{b}}} \times e^{-R/c}$	3 ( $a, b, c$ )	0.0617
Gaussian	$e^{-\left(\frac{R-a}{b}\right)^2}$	2 ( $a, b$ )	0.0629

**Table 7.1** Analytical models applied to the initial population distribution, along with the associated best-fit sum-of-squares error.

closer range. As a consequence, these simulated population transfers fall off more slowly with spectral-cut detuning for shorter-range initial populations.

A first appraisal of Fig. 7.7 might conclude that there is poor agreement between theory and experiment, as the raw data do not align well with the theoretical curve of any one initial state. It may be conjectured, however, that the atom pairs contributing to this pump-probe process will realistically be distributed over a range of internuclear separations rather than located at a single point. Indeed, the fact that the experimental data span a number of these theoretical series may be interpreted as a corroboration of this hypothesis. Consequently, a numerical optimization was computed to find the weighted sum of the theoretical series that best reproduced the data.

The most general approach to this calculation would involve the optimization of an arbitrary numerical distribution over these series; thus the number of fitting

parameters would be equal to the number of simulated curves. This was considered to be too computationally intense, and so the optimization was instead performed using a range of trial analytical curves for the initial distribution (see Table 7.1 for details). Thus the number of fitting parameters was greatly reduced. Excellent agreement between theory and experiment was found for each of these analytical fits (Fig. 7.7).<sup>1</sup> They all shared the common characteristic that population was localized and confined to internuclear separations of 30-60  $a_0$  (see Fig. 7.8). By contrast, the outer turning point of the most populated triplet vibrational state according to the study of Section 7.2 is located at 25  $a_0$ .

This provides evidence that the population addressed by the pump-probe experiment is different from the background triplet distribution photoassociated by the MOT light. The fit is qualitatively robust with respect to the mathematical description employed. Instead, the inferred distribution is consistent with the association of unbound atoms, coinciding with several antinodes of the scattering wavefunction. In this case, the detuning of the probe pulse from the  $\text{Rb}^+$  asymptote might account for the lack of a contribution from the very long-range portion of the scattering wavefunction. As an alternative explanation, calculations indicate that the TOF electric field is sufficient to dissociate molecular ions (causing  $\text{Rb}_2^+ \rightarrow \text{Rb}^+ + \text{Rb}$ ) of longer range than around 90  $a_0$ .

---

<sup>1</sup>For the sake of clarity, only the Gaussian fit is featured in this figure.

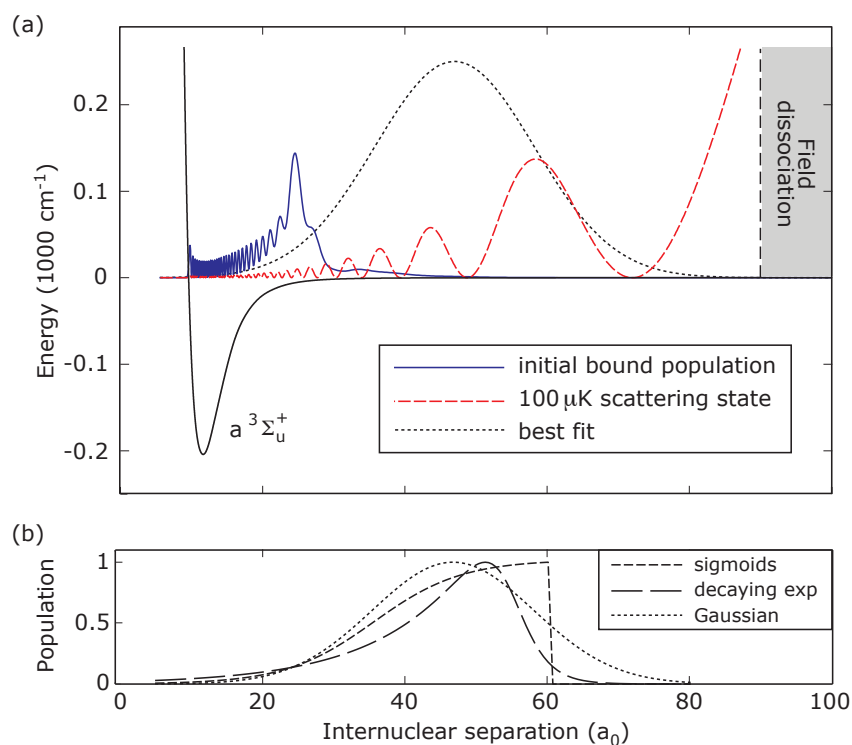


**Figure 7.8** (a) The population distributions of both the background molecules characterized in Section 7.2 and a  $100 \mu\text{K}$  scattering state, together with a Gaussian analytical best fit of the population distribution that contributes to the pump-probe signal. The contributing population is of longer range than the background molecules, but is consistent with the association of unbound scattering atoms by the pump pulse. Dissociation of molecular ions by the TOF electric field is calculated to account for the lack of contribution of very long-range scattering atom pairs to the  $\text{Rb}_2^+$  signal. (b) Further details of the three optimized analytical fits as described in the text. The three are in close qualitative agreement with each other, showing the robustness of this fit with respect to the choice of model.

### 7.3 Summary

In this chapter, a spectroscopic measurement of the preformed population of loosely bound ground-state triplet molecules within the MOT was presented. The measurement employed a two-photon REMPI scheme, with the coarse structure within the resultant spectrum reflecting the excited-state spacing and the fine structure revealing the ground-state occupancy. The twin mechanisms of three-body recombination and trapping light photoassociation are known to contribute to this background population with relative impacts that are determined by the particular experimental conditions. The measurement of the initial ground triplet-state occupancy revealed a distribution that closely matched the photoassociative mechanism via the  $0_g^-$  intermediary potential, confirming this to be the dominant contribution in this case. This bound population therefore needs to be considered as a candidate initial state for the pump pulse in addition to unbound atom pairs.

In a further experiment, the atomic and molecular ion signals were measured as a function of pump-pulse spectral-cut detuning and at a fixed positive delay. The atomic ion signal dropped off rapidly with detuning, whereas the molecular ion signal persisted for a few tens of inverse centimetres. This indicates that the pump pulse is exciting population into bound molecular states. The behaviour of the  $\text{Rb}_2^+$  signal contains information about the initial internuclear separation of the atom pair, and was consistent with calculations for a distribution of separations around 30-60  $a_0$ . This implies the association of unbound scattering atom pairs, rather than the excitation of background triplet molecules. Calculations indicated that the bulk

of the excited-state dynamics induced from such an unbound initial state would occur at larger internuclear separations than are resonantly addressed by the probe pulse. This may therefore be a factor in the lack of experimental observation of pump-probe dynamics.

The ultimate goal, however, remains the coherent control of this population so as to maximize the Franck–Condon overlap to the dump-pulse target state after a suitably chosen delay; a signal presenting evidence of wavepacket oscillations is therefore required. Simulations reveal that pre-associated molecules in an incoherent mixture of states can be made to oscillate coherently with 5 ps timescales at relatively close range using a single ultrafast pump pulse [106]. By contrast, the classical oscillation period of molecules photoassociated from scattering atom pairs is greater by an order of magnitude or more, and occur predominantly at long range where detection is particularly difficult. Increasing the signal-to-noise size at the larger pump-pulse detunings that address the relatively close-range pre-formed molecules should therefore allow this coherent behaviour to be revealed and controlled. The implications of this — namely an improvement to the photoassociation efficiency via an increase in MOT number and density — are discussed in more detail in the conclusion.



## Chapter 8

# Conclusion and outlook

*The Warrior of Light asks himself: ‘How will this affect the fifth generation of my descendants?’*

This thesis is motivated by an interest in the formation of ultracold molecules within their ground electronic and rovibrational states. The art of atomic cooling is now well established, and has been applied in many laboratories with diverse applications. The application, however, of the closed-loop optical cycle — the most robust approach to atomic cooling — to the molecular regime is frustrated by the more intricate spectroscopy.

The formation of translationally cold molecules in prescribed internal states has thus been bifurcated into approaches that seek to cool molecules directly and approaches that seek to associate pre-cooled atoms. The former techniques show promise for the attainment of deeply bound rovibrational states, but cannot reach sub-millikelvin temperatures where quantum mechanical processes dominate colli-

sions. By contrast, both optical (photoassociation) and magnetic (association by Feshbach resonance) approaches to indirect cooling are able to harness the ultracold temperatures of the initial atoms; however, more subtle techniques are necessary for the prescription of near-arbitrary, deeply bound internal states. Such techniques are now the subject of exploration in the laboratory, and show significant potential. It therefore appears that the indirect approaches show the greater promise in the quest for ultracold, ground-state molecules.

Two promising indirect approaches are the transfer of Feshbach molecules to lower-lying vibrational states using STIRAP and broadband incoherent optical cycling. Both have been applied to form vibrational ground-state molecules; however, the former requires a detailed spectroscopic knowledge of the system whilst the latter requires a pathway for initial-state preparation that is serendipitous to one particular species and causes heating.

These strategies are therefore complemented by broadband photoassociation techniques. The application of tailored optical fields to steer the course of a chemical reaction has shown potential in a diverse range of applications, and these quantum control tools lend themselves to this particular problem. Despite the counterintuitive contrast of scales, ultrafast pulses from a Ti:sapphire system are ideally suited to the formation of ultracold molecules, since their frequencies and bandwidths are well matched to the molecular spectroscopy of various alkali metals. The excitation of a coherent superposition of vibrational states may create a localized wavepacket that evolves within a manifold of attractive excited-state potentials. As the wavepacket

moves to closer range, a dump pulse may subsequently be applied in order to transfer the population coherently to a deeply bound target state.

Previous studies of ultrafast photoassociation revealed that broadband pulses acted to suppress a background population of pre-associated molecules, rather than to create new ones. Within this thesis, this experiment was extended into a higher pulse-energy regime, using an amplified ultrafast system at lower repetition rate (see Chapter 5). The higher pulse energies allowed strong-field interactions with the atom pairs, and the lower repetition rate prevented the deleterious effect of subsequent pulses counteracting the results of their predecessors. The ground-state quenching observations were reproduced within this regime, with the molecular signal decaying exponentially with pulse fluence. No dependence of the signal on the group velocity dispersion of the pulses was observed, though significant levels of noise motivated refinements to the apparatus.

The various improvements effected to the experimental setup were discussed in Chapter 4. The MOT, which acted as the source of both cold atoms and background molecules, was redesigned in order to improve its shape and stability. These improvements were guided by some simulations of the MOT atom-capture process. As a result, great improvements were made in the day-to-day alignment of the experiment, facilitating the subsequent experiments. The ultrafast system was redesigned in order to bring its central wavelength into line with the optimum Franck–Condon windows for photoassociation in  $\text{Rb}_2$ , and a new ultrafast source (the NOPA) was developed to act as a time-resolved probe of the excited state. The ground-state

REMPI detection schemes were expanded to resolve the distribution of background molecules and address different populations.

In Chapter 6, attention was then turned from the ground to the excited state. Rather than detecting the effect of an ultrafast pulse on the background molecular population using a ‘slow’ detection laser after sufficient time for decay to the ground state, it was decided to measure the excited-state dimers directly in a time-resolved pump-probe experiment. These experiments demonstrated the formation of bound excited-state population by an ultrafast photoassociation pulse. This represents an important milestone in the design of a coherent pump-dump transfer strategy.

Calculations predict that the degree of evidence of wavepacket dynamics is influenced by the initial state of the interacting atom pairs. Two candidates merit consideration within this experiment: unbound scattering atom pairs, and loosely bound, pre-associated molecules. It is predicted that excited-state oscillations from the latter would occur at shorter range and be more prominent. With this in mind, the background molecules were first characterized using a spectroscopic measurement, and the resultant distribution was found to match the expected product of photoassociation by the MOT light (see Chapter 7). The behaviour of the atomic and molecular ion signals was analyzed as the pump pulse was detuned, and the implied initial distribution deduced. This fit was consistent with the pump pulse acting to photoassociate free atom pairs at long range, rather than exciting the pre-associated background molecules.

The identification of the initial population that is addressed by the pump pulse

is particularly important in light of the contrasting predicted dynamics of the two candidates. Further increasing the signal-to-noise ratio at larger pump-pulse detunings would allow the dynamics of the relatively close-range pre-formed molecules to be observed. This would permit the more predominant coherent behaviour of this initial state to be revealed and controlled.

## 8.1 Outlook

The central objective of this experiment is the creation, control and transfer between electronic potentials of localized molecular wavepackets using ultrafast pulses. The pump-dump strategy involves three steps: the creation of an excited molecular wavepacket at long range; free evolution to short range within an attractive potential manifold; and the transfer of population to short-range, deeply bound product states within the ground potential.

Chapters 6 and 7 describe the first experimental demonstration of the first stage of this pump-dump process. It was hoped that the pump-probe signal of Chapter 6 would contain periodic oscillations as evidence of excited-state dynamics. The absence of such oscillations has been attributed to both an unhelpfully long-range interacting initial population and an insufficiently selective detection mechanism. The observation of a time-varying, position-selective signal attributable to excited-state dynamics is identified as a key target milestone before the final step can be tailored; thus the immediate outlook of this experiment concerns the addressing of these twin issues.

Chapter 7 identified that the pump pulse addresses long-range population that is likely to originate from scattering atom pairs. Calculations predict that the dynamics resulting from bound background molecules promoted to the excited state would occur at closer range and be more visible. With reference to Figs. 7.7 and 7.8, the experimental consequences of this objective are a visible pump-probe signal at spectral cut detunings of the order of  $50 \text{ cm}^{-1}$ . With the existing apparatus, the signal-to-noise ratio at these detunings is palpably too poor; an improvement in photoassociation efficiency is therefore required. Since the photoassociation rate scales in proportion to the product of the density and the number of trapped atoms (Equation 2.33), these two parameters are identified as targets for an improvement to the experimental apparatus.

Neutral-neutral transitions to, and subsequent evolution within, the relatively modestly sized potential manifolds corresponding to low-lying excited atomic asymptotes may be addressed by quantitative calculations. A common experimental detection approach involves ionization, with TOF detection schemes offering detection and resolution of different species with decent sensitivity; however, molecular ionization is currently a much murkier theoretical domain than the atomic case. Only limited guidance is therefore placed at the experimentalist's disposal with regard to the design of the probe pulse. The choice of bandwidth offers a dilemma between the Scylla of pulse duration and Charybdis of ionization window width; meanwhile, indirect ionization mechanisms further complicate the navigation of the probe pathway.

An alternative detection mechanism could be conjectured based around absorption imaging of a weak probe beam. A narrowband probe could be tuned to promote population to the Condon point of a higher lying neutral potential. This would offer high selectivity with regard to internuclear separation at the expense of time resolution. More pertinently for the pump-probe process, an ultrafast probe beam could instead be employed in this fashion, with the central wavelength selected in the infrared region to coincide with a narrow excitation window to a higher neutral potential. In either circumstance, the absorption of the beam would thus indicate the excited-state population within the addressed window. As an alternative, the fluorescence resulting from the subsequent spontaneous decay could instead be monitored. In either instance, however, a much higher molecular density would be required in order for an appreciable absorption or fluorescence signal to be produced.

These two impediments to the observation of excited-state dynamics might therefore both be addressable through a common strategy: an increase to the number and density of the trapped atoms. To this effect, the construction of a new apparatus is already underway under the leadership of another D. Phil. student (Duncan England). This apparatus comprises a MOT with higher atom numbers, together with the infrastructure required for evaporation within both optical and magnetic traps, and current-stabilized magnetic coils for the manipulation of Feshbach resonances. The goal is to approach or attain the degeneracy of a BEC. At such densities, it is hoped that the closer-range population formed by either background photoassociated or Feshbach associated molecules may be addressed in preference to unbound

atom pairs. This new apparatus thus provides optimism for the observation of excited-state wavepacket dynamics and the concomitant insight into the design of a pump-dump route to deeply bound vibrational states.

# Appendix A

## Rubidium: atomic and molecular data

*The Warrior of Light gives before he is asked.*

### A.1 Atomic data

Some properties of the two naturally occurring isotopes of rubidium,  $^{85}\text{Rb}$  and  $^{87}\text{Rb}$ , are presented in Table A.1. Some energy levels are given in Table A.2. Data are from Steck [137, 138] and Sansonetti [171].

Property	<sup>85</sup> Rb	<sup>87</sup> Rb
Atomic number $Z$	37	37
Mass number $A$	85	87
Relative atomic mass (g/mol)	84.912	86.909
Relative natural abundance	72.17 %	27.83 %
Lifetime (years)	stable	$4.8 \times 10^{10}$
Nuclear spin	5/2	3/2

**Table A.1** Properties of the isotopes of rubidium.

Configuration	$J$	$E$ (cm <sup>-1</sup> )	Configuration	$J$	$E$ (cm <sup>-1</sup> )
$4p^65s$	1/2	0	$4p^67d$	3/2	30 280.113
$4p^65p$	1/2	12 578.950		5/2	30 281.620
	3/2	12 816.545	$4p^69s$	1/2	30 499.031
$4p^64d$	5/2	19 355.203	$4p^66f$	7/2	30 627.962
	3/2	19 355.649		5/2	30 627.978
$4p^66s$	1/2	20 132.510	$4p^69p$	1/2	30 958.91
$4p^66p$	1/2	23 715.081		3/2	30 970.19
	3/2	23 792.591	$4p^68d$	3/2	31 221.440
$4p^65d$	3/2	25 700.536		5/2	31 222.453
	5/2	25 703.498	$4p^610s$	1/2	31 362.331
$4p^67s$	1/2	26 311.437	$4p^67f$	7/2	31 441.718
$4p^64f$	7/2	26 792.092		5/2	31 441.730
	5/2	26 792.118	$4p^610p$	1/2	31 653.85
$4p^67p$	1/2	27 835.02		3/2	31 661.16
	3/2	27 870.11	$4p^69d$	3/2	31 821.855
$4p^66d$	3/2	28 687.127		5/2	31 822.550
	5/2	28 689.390	$4p^611s$	1/2	31 917.221
$4p^68s$	1/2	29 046.816	$4p^68f$	7/2	31 969.616
$4p^65f$	7/2	29 277.768		5/2	31 969.621
	5/2	29 277.787	$4p^611p$	1/2	32 113.55
$4p^65g$	7/2	29 296.196		3/2	32 118.52
	9/2	29 296.196	$4p^610d$	3/2	32 227.610
$4p^68p$	1/2	29 834.94		5/2	32 228.108
	3/2	29 853.79	$\text{Rb}_2^+$		33 690.81

**Table A.2** Rubidium energy levels,  $E$ , with fine structure.

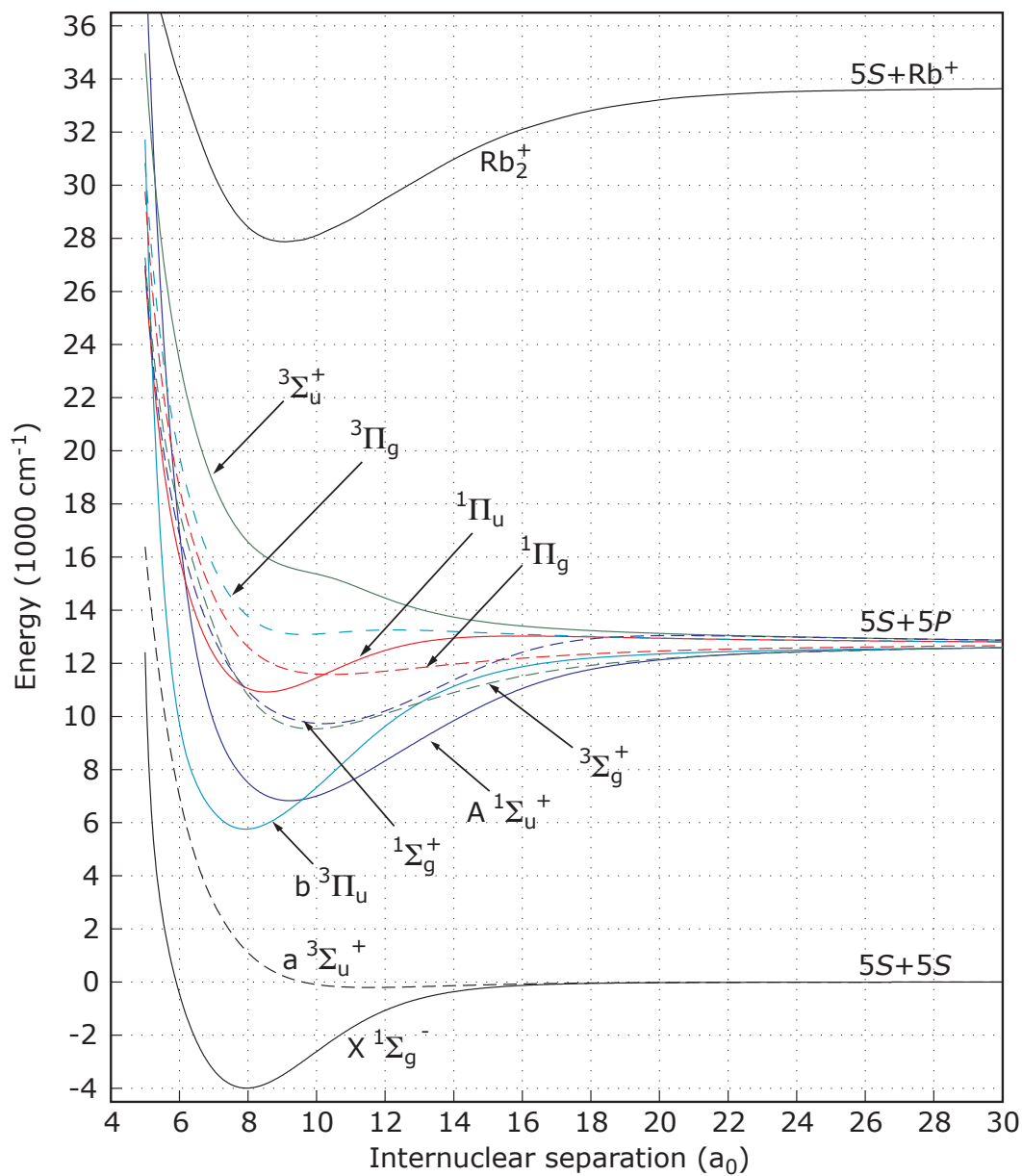


**Figure A.1**  $\text{Rb}_2$  molecular potentials asymptotic to a  $5S+5P$  atom pair, together with the ground triplet,  $a^3\Sigma_u^+$ , and singlet,  $X^1\Sigma_g^+$ , potentials and the ground  $\text{Rb}_2^+$  potential. The potentials are labelled according to the appropriate Hund's case (a) spectroscopic notation. The ground triplet state is dashed, as are coupled  $5S + 5P$  excited states. The ground singlet state and coupled excited states are solid.

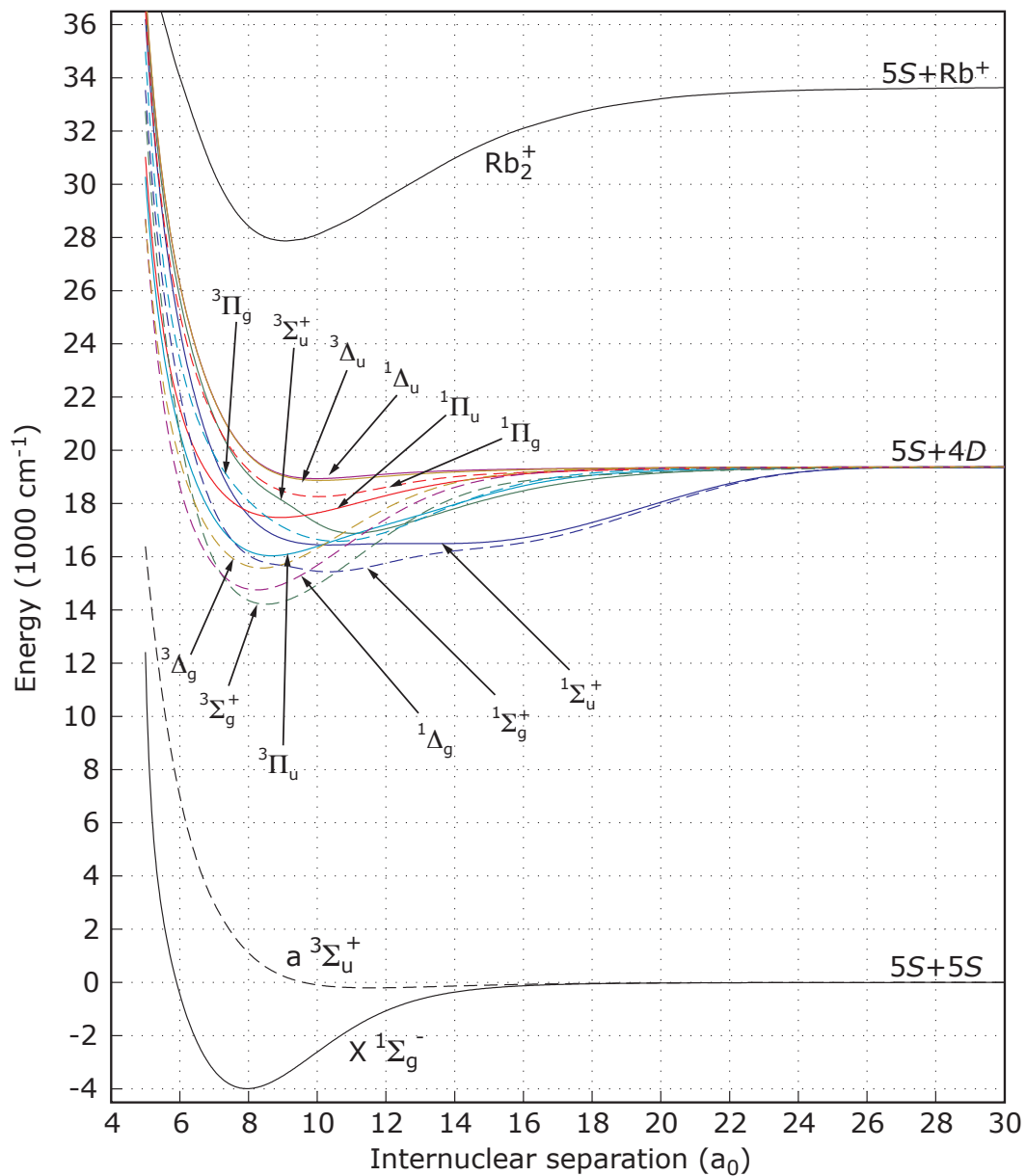


**Figure A.2** As per the previous figure but for the case of the  $5S + 4D$  potential manifold.

## A.2 Molecular potentials

Some reference short-range potentials are plotted in Hund's case (a) notation in Fig. A.1 (correlating to the  $5S + 5P$  atomic asymptote) and Fig. A.2 (correlating to  $5S + 4D$ ). The ground triplet,  $a^3\Sigma_u^+$ , and singlet,  $X^1\Sigma_g^+$ , potentials are included for reference together with the ground molecular ion potential. Parity conservation requires a change in symmetry ( $u \leftrightarrow g$ ) for each transition. Hence excited states accessible from the ground singlet according to this selection rule are indicated with solid lines, whilst excited states coupled to the triplet are indicated with dashed lines.

The short-range portion of the  $X^1\Sigma_g^+$  potential is obtained from the spectroscopic study of Seto *et al.* [172]. It was fitted to a long-range tail from van Kempen *et al.* [144]. The  $a^3\Sigma_u^+$  potential was obtained from the research group of Chris Greene at JILA, Boulder, Colorado [173, 174]. The  $A^1\Sigma_u^+$  and  $b^3\Pi_u$  potentials were derived from spectroscopic measurements [175]. The remaining neutral potentials are *ab initio* calculations by Park *et al.* [176]. The ion potential was obtained from Aymar *et al.* [177].

## A.3 Two-photon ionization wavelengths

This thesis refers to two-photon REMPI detection pathways for ground-state molecules. With this in mind, the transition wavelengths for both photons are presented in Fig. A.3 (for pathways via the  $5S + 5P$  manifold) and Fig. A.4 (for pathways via the

$5S + 4D$  manifold). In each figure, pathways via potentials that couple to (a) the ground singlet, and (b) the ground triplet potentials are presented separately.

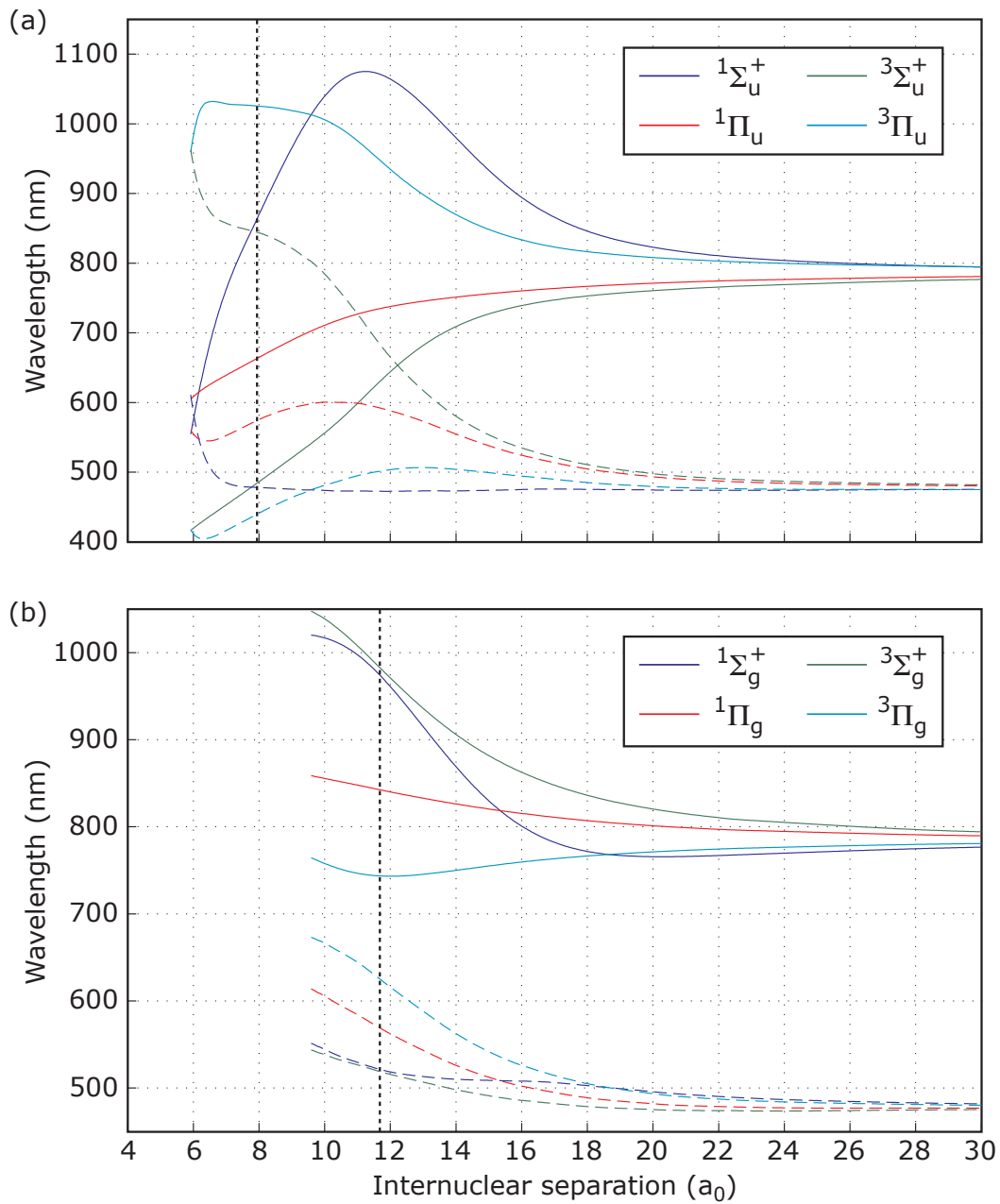


**Figure A.3** Two-photon ionization wavelengths from (a) the ground singlet,  $X^1\Sigma_g^+$ , and (b) the ground triplet,  $a^3\Sigma_u^+$ , potentials, via an intermediate potential within the  $5S + 5P$  manifold. Pathways via each different intermediate potential are represented by a different colour according to the legend. The solid line represents the wavelength for the first photon (i.e.  $5S + 5S \rightarrow 5S + 5P$ ), and the dashed line represents the wavelength for the second photon (i.e.  $5S + 5P \rightarrow 5S + \text{Rb}^+$ ). The vertical dotted line marks the minimum of the ground-state potential.

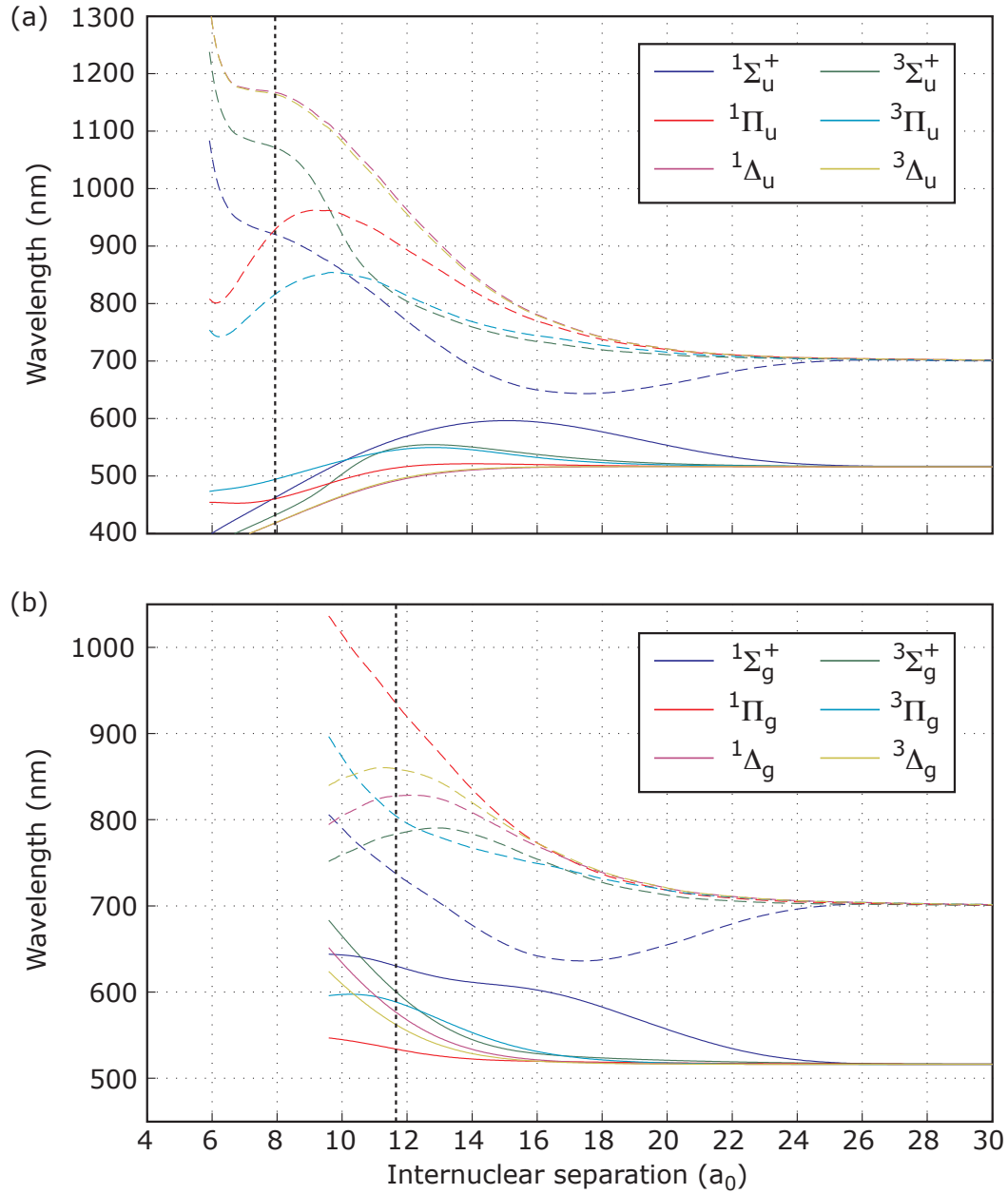


**Figure A.4** Two-photon ionization wavelengths from (a) the ground singlet,  $X^1\Sigma_g^+$ , and (b) the ground triplet,  $a^3\Sigma_u^+$ , potentials, via an intermediate potential within the  $5S + 4D$  manifold. The details are as per the previous figure.

## Appendix B

# MOT characterization

*The Warrior of Light pays attention to small things because they can severely hamper him.*

This appendix presents brief details of the experimental methods used to characterize the MOT, together with relevant calculations.

### B.1 MOT number characterization

The number of trapped atoms was estimated via a measurement of the MOT fluorescence, according to the method outlined in Section VI C of [151]. A lens imaged the fluorescence onto a photodiode, and the scattering rate was deduced from the ensuing signal in combination with certain MOT parameters. A narrow bandwidth filter at 780 nm restricted background noise from room lights.

The rate at which a single two-level atom scatters photons (see Equation 4.2) is given by

$$R_{\text{scatt}} = \frac{\Gamma}{2} \frac{I/I_{\text{sat}}}{1 + I/I_{\text{sat}} + (2\delta/\Gamma)^2} \quad (\text{B.1})$$

with terms as defined in 4.2.1. Assuming a Gaussian intensity distribution, the peak trapper intensity is  $I = P \ln 2 / \pi w^2$ , where  $P$  is the total power and  $w$  the half-width beam waist; for the purposes of this calculation the effective MOT intensity was also doubled due to the counter-propagating beam configuration. The scattered photons are emitted isotropically, with a lens of diameter  $d$  and at a distance  $D$  from the MOT collecting the fraction

$$\eta = \frac{\pi(d/2)^2}{4\pi D^2} = \frac{d^2}{16D^2}. \quad (\text{B.2})$$

The photon flux at the photodiode may be calculated according to its responsivity  $\rho$ , load resistance  $R$ , and measured voltage  $V$  as follows:

$$R_{\text{det}} = \frac{V}{\rho R} \frac{\lambda}{hc}. \quad (\text{B.3})$$

The number of scattering atoms<sup>1</sup> within the MOT may therefore be deduced:

$$N = \frac{R_{\text{det}}}{\eta R_{\text{scatt}}}. \quad (\text{B.4})$$

Using the typical experimental parameters listed in Table B.1, a typical MOT size

---

<sup>1</sup>Note that, for the case of a dark SPOT MOT, the fraction of the population residing in the dark state must also be taken into account.

Experimental parameter	Typical value
Natural linewidth, $\Gamma$	5.9 MHz
Trapper power, $P$	25 mW
Beamwaist, $w$	3 mm
Saturation intensity, $I_{\text{sat}}$	4.1 mW/cm <sup>2</sup>
Detuning, $\delta$	15 MHz
Lens diameter, $d$	3.5 cm
Lens distance from MOT, $D$	19 cm
Photodiode responsivity at 780 nm, $\rho$	0.5 A/W
Load resistance, $R$	940 k $\Omega$
Trapping wavelength, $\lambda$	780 nm
Photodiode voltage, $V$	10 mV

**Table B.1** Typical MOT experimental parameters.

was therefore estimated at  $2 \times 10^7$  atoms.

## B.2 MOT temperature characterization

The temperature of the atoms in the MOT was estimated using the release-and-recapture technique [158]. The MOT is loaded and a steady-state population attained. Then the trapping light is extinguished for a variable window using the AOMs, resulting in a period of free expansion before the light is unshuttered and those atoms that remain within the capture region are recaptured. By measuring the photodiode fluorescence signal when the trapper is unshuttered, the number of recaptured atoms may be measured as a function of expansion period. This plot is shown in Fig. B.1. A theoretical simulation assumes a Maxwell-Boltzmann distribution of velocities characterized by a temperature, and calculates the population fraction that remains within a trapping region defined by the volume of overlap of

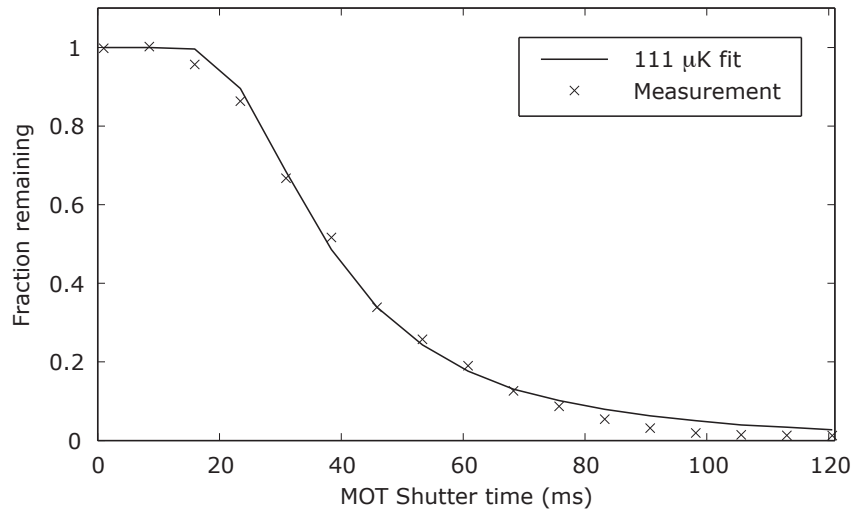


**Figure B.1** A release-and-recapture measurement of the MOT temperature. The number of recaptured atoms is shown as a function of delay before the resumption of the trapping light. The theoretical best fit, which assumes a Maxwell-Boltzmann distribution of velocities, is obtained at a temperature of  $111 \mu\text{K}$ .

the MOT light after a given period of free expansion. Close agreement between data and simulation was obtained for a temperature of  $111 \mu\text{K}$ .

# Bibliography

- [1] Paulo Coelho. *Manual of the Warrior of Light*. HarperCollins, 2003.
- [2] William D. Phillips. Nobel lecture: Laser cooling and trapping of neutral atoms. *Rev. Mod. Phys.*, 70(3):721–741, 1998.
- [3] Steven Chu. Nobel lecture: The manipulation of neutral particles. *Rev. Mod. Phys.*, 70(3):685–706, 1998.
- [4] Claude N. Cohen-Tannoudji. Nobel lecture: Manipulating atoms with photons. *Rev. Mod. Phys.*, 70(3):707–719, 1998.
- [5] C. S. Adams and E. Riis. Laser cooling and trapping of neutral atoms. *Progress in Quantum Electronics*, 21(1):1 – 79, 1997.
- [6] H. J. Metcalf and P. van der Straten. Laser cooling and trapping of atoms. *J. Opt. Soc. Am. B*, 20(5):887–908, 2003.
- [7] E.A. Cornell and C.E. Wieman. Nobel lecture: Bose-Einstein condensation in a dilute gas, the first 70 years and some recent experiments. *Rev. Mod. Phys.*, 74:875–893, 2002.
- [8] Wolfgang Ketterle. Nobel lecture: When atoms behave as waves: Bose-Einstein condensation and the atom lasers. *Rev. Mod. Phys.*, 74(4):1131–1151, 2002.
- [9] J. Küpper, H. L. Bethlem, B. Sartakov, A. J. A. van Roij, and G. Meijer. Decelerated molecular beams for high-resolution spectroscopy. *Eur. Phys. J. D*, 31(2):337–349, 2004.
- [10] D. DeMille. Quantum computation with trapped polar molecules. *Phys. Rev. Lett.*, 88(6):067901, 2002.
- [11] Carmen M. Tesch and Regina de Vivie-Riedle. Quantum computation with vibrationally excited molecules. *Phys. Rev. Lett.*, 89(15):157901, 2002.
- [12] B.E. Sauer, H.T. Ashworth, J.J. Hudson, M.R. Tarbutt, and E.A. Hinds. Probing the electron EDM with cold molecules. In C Roos, H Haffner, and R Blatt, editors, *20th International Conference on Atomic Physics*, pages 44–51, 2006.

- [13] Jonathan D. Weinstein, Robert deCarvalho, Thierry Guillet, Bretislav Friedrich, and John M. Doyle. Magnetic trapping of calcium monohydride molecules at millikelvin temperatures. *Nature*, 395:148–150, 1998.
- [14] Hendrick L. Bethlem, Giel Berden, Floris M. H. Crompvoets, Rienk T. Jongma, André J. A. van Roij, and Gerard Meijer. Electrostatic trapping of ammonia molecules. *Nature*, 406:491–494, 2000.
- [15] H.R. Thorsheim, J. Weiner, and P.S. Julienne. Laser-induced photoassociation of ultracold sodium atoms. *Phys. Rev. Lett.*, 58(23):2420–2423, 1987.
- [16] A. Fioretti, D. Comparat, A. Crubellier, O. Dulieu, F. Masnou-Seeuws, and P. Pillet. Formation of cold Cs<sub>2</sub> molecules through photoassociation. *Phys. Rev. Lett.*, 80(20):4402–4405, 1998.
- [17] Markus Greiner, Cindy A. Regal, and Deborah S. Jin. Emergence of a molecular Bose-Einstein condensate from a Fermi gas. *Nature*, 426:537, 2003.
- [18] M.W. Zwierlein, C. A. Stan, C. H. Schunck, S.M.F. Raupach, S. Gupta, Z. Hadzibabic, and W. Ketterle. Observation of Bose-Einstein condensation of molecules. *Phys. Rev. Lett.*, 91(25):250401, 2003.
- [19] S. Jochim, M. Bartenstein, A. Altmeyer, G. Hendl, S. Riedl, C. Chin, J. Hecker Denschlag, and R. Grimm. Bose-Einstein condensation of molecules. *Science*, 302:2101, 2003.
- [20] Matthieu Viteau, Amodsen Chotia, Maria Allegrini, Nadia Bouloufa, Olivier Dulieu, Daniel Comparat, and Pierre Pillet. Optical pumping and vibrational cooling of molecules. *Science*, 321(5886):232–234, 2008.
- [21] Johann G. Danzl, Elmar Haller, Mattias Gustavsson, Manfred J. Mark, Russell Hart, Nadia Bouloufa, Olivier Dulieu, Helmut Ritsch, and Hanns-Christoph Nägerl. Quantum gas of deeply bound ground state molecules. *Science*, 321(5892):1062–1066, 2008.
- [22] F. Lang, K. Winkler, C. Strauss, R. Grimm, and J. Hecker Denschlag. Ultracold triplet molecules in the rovibrational ground state. *Phys. Rev. Lett.*, 101(13):133005, 2008.
- [23] K. Winkler, F. Lang, G. Thalhammer, P. v. d. Straten, R. Grimm, and J. Hecker Denschlag. Coherent optical transfer of Feshbach molecules to a lower vibrational states. *Phys. Rev. Lett.*, 98(4):043201, 2007.
- [24] K.-K. Ni, S. Ospelkaus, M. H. G. de Miranda, A. Pe’er, B. Neyenhuis, J. J. Zirbel, S. Kotochigova, P. S. Julienne, D. S. Jin, and J. Ye. A high phase-space-density gas of polar molecules. *Science*, 322(5899):231–235, 2008.
- [25] Warren S. Warren, Herschel Rabitz, and Mohammed Dahleh. Coherent control of quantum dynamics: The dream is alive. *Science*, 259(5101):1581–1589, 1993.

- [26] Herschel Rabitz, Regina de Vivie-Riedle, Marcus Motzkus, and Karl Kompa. Whither the future of controlling quantum phenomena? *Science*, 288:824–828, 2000.
- [27] Benjamin L. Brown, Alexander J. Dicks, and Ian A. Walmsley. Coherent control of ultracold molecule dynamics in a magneto-optical trap by use of chirped femtosecond laser pulses. *Phys. Rev. Lett.*, 96(17):173002, 2006.
- [28] Wenzel Salzmann, Ulrich Poschinger, Roland Wester, Matthias Weidemüller, Andrea Merli, Stefan M. Weber, Franziska Sauer, Mateusz Plewicky, Fabian Weise, Aldo Mirabal Esparza, Ludger Wöste, and Albrecht Lindinger. Coherent control with shaped femtosecond laser pulses applied to ultracold molecules. *Phys. Rev. A*, 73(2):023414, 2006.
- [29] G.K. Woodgate. *Elementary Atomic Structure*. McGraw-Hill, 1970.
- [30] G. Herzberg. *Molecular Spectra and Molecular Structure: I. Spectra of Diatomic Molecules*. VNR, 2nd edition, 1950.
- [31] P. W. Atkins. *Molecular Quantum Mechanics (Part III)*, volume II. Clarendon Press, 1970.
- [32] Kevin M. Jones, Eite Tiesinga, Paul D. Lett, and Paul S. Julienne. Ultracold photoassociation spectroscopy: Long-range molecules and atomic scattering. *Rev. Sci. Instrum.*, 78(2):483, 2006.
- [33] Harold J. Metcalf and Peter van der Straten. *Laser cooling and trapping*. Springer, 1999.
- [34] Lev Pitaevskii and Sandro Stringari. *Bose-Einstein condensation*. Oxford Science Publications, 2003.
- [35] C. J. Pethick and H. Smith. *Bose-Einstein condensation in dilute gases*. Cambridge University Press, 2002.
- [36] John S. Townsend. *A modern approach to quantum mechanics*. University Science Books, 2000.
- [37] Christopher J. Foot. *Atomic Physics*. OUP, 2005.
- [38] Mary L. Boas. *Mathematical methods in the physical sciences*. John Wiley & Sons, 2nd edition, 1983.
- [39] L. S. Butcher, D. N. Stacey, C. J. Foot, and K. Burnett. Ultracold collisions for Bose-Einstein condensation. *Phil. Trans. R. Soc. Lond. A*, 357:1421–1439, 1999.
- [40] M. Gupta and D. Herschbach. Slowing and speeding molecular beams by means of a rapidly rotating source. *J. Phys. Chem. A.*, 105(9):1626–1637, 2001.

- [41] John M. Doyle, Bretislav Friedrich, Jinha Kim, and David Patterson. Buffer gas loading of atoms and molecules into a magnetic trap. *Phys. Rev. A.*, 52(4):R2515–R2518, 1995.
- [42] Richard J. Knight. Deceleration of polar molecules in inhomogeneous electric fields. Master’s thesis, University of Oxford, 2005.
- [43] E. S. Shuman, J. F. Barry, D. R. Glenn, and D. DeMille. Radiative force from optical cycling on a diatomic molecule. *Phys. Rev. Lett.*, 103(22):223001, 2009.
- [44] M. Zeppenfeld, M. Motsch, P. W. H. Pinkse, and G. Rempe. Optoelectrical cooling of polar molecules. *Phys. Rev. A*, 80(4):041401, 2009.
- [45] Thorsten Kohler, Krzysztof Goral, and Paul S. Julienne. Production of cold molecules via magnetically tunable Feshbach resonances. *Rev. Mod. Phys.*, 78(4):1311, 2006.
- [46] S. Inouye, M. R. Andrews, J. Stenger, H.-J. Miesner, D. M. Stamper-Kurn, and W. Ketterle. Observation of Feshbach resonances in a Bose-Einstein condensate. *Nature*, 392:151, 1998.
- [47] E. Hodby, S. T. Thompson, C. A. Regal, M. Greiner, A. C. Wilson, D. S. Jin, E. A. Cornell, and C. E. Wieman. Production efficiency of ultracold Feshbach molecules in bosonic and fermionic systems. *Phys. Rev. Lett.*, 94(12):120402, 2005.
- [48] G. Thalhammer, K. Winkler, F. Lang, S. Schmid, R. Grimm, and J. Hecker Denschlag. Long-lived Feshbach molecules in a three-dimensional optical lattice. *Phys. Rev. Lett.*, 96(5):050402, 2006.
- [49] Elizabeth A. Donley, Neil R. Claussen, Sarah T. Thompson, and Carl E. Wieman. Atom-molecule coherence in a Bose-Einstein condensate. *Nature*, 417:529–533, 2002.
- [50] Jens Herbig, Tobias Kraemer, Michael Mark, Tino Weber, Cheng Chin, Hanns-Christoph Nägerl, and Rudolf Grimm. Preparation of a pure molecular quantum gas. *Science*, 301(5639):1510–1513, 2003.
- [51] Stephan Durr, Thomas Volz, Andreas Marte, and Gerhard Rempe. Observation of molecules produced from a Bose-Einstein condensate. *Phys. Rev. Lett.*, 92(2):020406, 2004.
- [52] K. Xu, T. Mukaiyama, J. R. Abo-Shaeer, J. K. Chin, D. E. Miller, and W. Ketterle. Formation of quantum-degenerate sodium molecules. *Phys. Rev. Lett.*, 91(21):210402, 2003.
- [53] J. Cubizolles, T. Bourdel, S. J. J. M. F. Kokkelmans, G. V. Shlyapnikov, and C. Salomon. Production of long-lived ultracold  $\text{Li}_2$  molecules from a Fermi gas. *Phys. Rev. Lett.*, 91(24):240401, 2003.

- [54] Kevin E. Strecker, Guthrie B. Partridge, and Randall G. Hulet. Conversion of an atomic Fermi gas to a long-lived molecular Bose gas. *Phys. Rev. Lett.*, 91(8):080406, 2003.
- [55] Cindy A. Regal, Christopher Ticknor, John L. Bohn, and Deborah S. Jin. Creation of ultracold molecules from a Fermi gas of atoms. *Nature*, 424:47–50, 2003.
- [56] J. J. Zirbel, K.-K. Ni, S. Ospelkaus, J. P. D’Incao, C. E. Wieman, J. Ye, and D. S. Jin. Collisional stability of fermionic Feshbach molecules. *Phys. Rev. Lett.*, 100(14):143201, 2008.
- [57] K. Pilch, A. D. Lange, A. Prantner, G. Kerner, F. Ferlaino, H.-C. Nägerl, and R. Grimm. Observation of interspecies Feshbach resonances in an ultracold Rb-Cs mixture. *Phys. Rev. A*, 79(4):042718, 2009.
- [58] P. Pillet, A. Crubellier, A. Bleton, O. Dulieu, P. Nosbaum, I. Mourachko, and F. Masnou-Seeuws. Photoassociation in a gas of cold alkali atoms: I. perturbative quantum approach. *J. Phys. B*, 30(12):2801–2820, 1997.
- [59] C. Gabbanini, A. Fioretti, A. Lucchesini, S. Gozzini, and M. Mazzoni. Cold rubidium molecules formed in a magneto-optical trap. *Phys. Rev. Lett.*, 84(13):2814–2817, 2000.
- [60] A. Fioretti, C. Amiot, C.M. Dion, O. Dulieu, M. Mazzoni, G. Smirne, and C. Gabbanini. Cold rubidium molecule formation through photoassociation: A spectroscopic study of the  $0_g^-$  long-range state of  $^{87}\text{Rb}_2$ . *Eur. Phys. J. D*, 15:189–198, 2001.
- [61] A. N. Nikolov, E. E. Eyler, X. T. Wang, J. Li, H. Wang, W. C. Stwalley, and P. L. Gould. Observation of ultracold ground-state potassium molecules. *Phys. Rev. Lett.*, 82(4):703–706, 1999.
- [62] T. Takekoshi, B. M. Patterson, and R. J. Knize. Observation of cold ground-state cesium molecules produced in a magneto-optical trap. *Phys. Rev. A*, 59(1):R5–R7, 1999.
- [63] D. Comparat, C. Drag, B. Laburthe Tolra, A. Fioretti, P. Pillet, A. Crubellier, O. Dulieu, and F. Masnou-Seeuws. Formation of cold  $\text{Cs}_2$  ground state molecules through photoassociation in the  $1_u$  pure long-range states. *Eur. Phys. J. D*, 11:59–71, 2000.
- [64] C. M. Dion, C. Drag, O. Dulieu, B. Laburthe Tolra, F. Masnou-Seeuws, and P. Pillet. Resonant coupling in the formation of ultracold ground state molecules via photoassociation. *Phys. Rev. Lett.*, 86(11):2253–2256, 2001.
- [65] Fredrik K. Fatemi, Kevin M. Jones, Paul D. Lett, and Eite Tiesinga. Ultracold ground-state molecule production in sodium. *Phys. Rev. A*, 66(5):053401, 2002.

- [66] A. N. Nikolov, J. R. Ensher, E. E. Eyler, H. Wang, W. C. Stwalley, and P. L. Gould. Efficient production of ground-state potassium molecules at sub-mK temperatures by two-step photoassociation. *Phys. Rev. Lett.*, 84(2):246–249, 2000.
- [67] He Wang and William C. Stwalley. Ultracold photoassociative spectroscopy of heteronuclear alkali-metal diatomic molecules. *J. Chem. Phys.*, 108(14):5767, 1998.
- [68] C. Haimberger, J. Kleinert, M. Bhattacharya, and N. P. Bigelow. Formation and detection of ultracold ground-state polar molecules. *Phys. Rev. A*, 70(2):021402, 2004.
- [69] M. W. Mancini, G. D. Telles, A. R. L. Caires, V. S. Bagnato, and L. G. Marcassa. Observation of ultracold ground-state heteronuclear molecules. *Phys. Rev. Lett.*, 92(13):133203, 2004.
- [70] D. Wang, J. Qi, M. F. Stone, O. Nikolayeva, H. Wang, B. Hattaway, S. D. Gensemer, P. L. Gould, E. E. Eyler, and W. C. Stwalley. Photoassociative production and trapping of ultracold KRb molecules. *Phys. Rev. Lett.*, 93(24):243005, 2004.
- [71] Andrew J. Kerman, Jeremy M. Sage, Sunil Sainis, Thomas Bergeman, and David DeMille. Production of ultracold, polar RbCs\* molecules via photoassociation. *Phys. Rev. Lett.*, 92(3):033004, 2004.
- [72] Andrew J. Kerman, Jeremy M. Sage, Sunil Sainis, Thomas Bergeman, and David DeMille. Production and state-selective detection of ultracold RbCs molecules. *Phys. Rev. Lett.*, 92(15):153001, 2004.
- [73] T. Bergeman, A.J. Kerman, J. Sage, S. Sainis, and D. DeMille. Prospects for production of ultracold  $X^1\Sigma^+$  RbCs molecules. *Eur. Phys. J. D*, 31(2):179–188, 2004.
- [74] Jeremy M. Sage, Sunil Sainis, Thomas Bergeman, and David DeMille. Optical production of ultracold polar molecules. *Phys. Rev. Lett.*, 94(20):203001, 2005.
- [75] J. Deiglmayr, A. Grochola, M. Repp, K. Mörtlbauer, C. Glück, J. Lange, O. Dulieu, R. Wester, and M. Weidemüller. Formation of ultracold polar molecules in the rovibrational ground state. *Phys. Rev. Lett.*, 101(13):133004, 2008.
- [76] D. Sofikitis, S. Weber, A. Fioretti, R. Horchani, M. Allegrini, B. Chatel, D. Comparat, and P. Pillet. Molecular vibrational cooling by optical pumping with shaped femtosecond pulses. *New J. Phys.*, 11:055037, 2009.

- [77] Dimitris Sofikitis, Ridha Horchani, Xiaolin Li, Marin Pichler, Maria Allegrini, Andrea Fioretti, Daniel Comparat, and Pierre Pillet. Vibrational cooling of cesium molecules using noncoherent broadband light. *Phys. Rev. A*, 80(5):051401, 2009.
- [78] Matthieu Viteau, Amodsen Chotia, Maria Allegrini, Nadia Bouloufa, Olivier Dulieu, Daniel Comparat, and Pierre Pillet. Efficient formation of deeply bound ultracold molecules probed by broadband detection. *Phys. Rev. A*, 79(2):021402, 2009.
- [79] E Gomez, L A Orozco, and G D Sprouse. Spectroscopy with trapped francium: advances and perspectives for weak interaction studies. *Rep. Prog. Phys.*, 69(1):79–118, 2006.
- [80] K. Bergmann, H. Theuer, and B. W. Shore. Coherent population transfer among quantum states of atoms and molecules. *Rev. Mod. Phys.*, 70(3):1003–1025, 1998.
- [81] Johann G. Danzl, Manfred J. Mark, Elmar Haller, Mattias Gustavsson, Russell Hart, Jesus Aldegunde, Jeremy M. Hutson, and Hanns-Christoph Nägerl. An ultracold high-density sample of rovibronic ground-state molecules in an optical lattices. *Nature Physics*, 6:265–270, 2010.
- [82] Ahmed H. Zewail. Femtochemistry: Atomic-scale dynamics of the chemical bond. *J. Phys. Chem. A*, 104(24):5660–5694, 2000.
- [83] Mette Machholm, Annick Giusti-Suzor, and F. H. Mies. Photoassociation of atoms in ultracold collisions probed by wave-packet dynamics. *Phys. Rev. A*, 50(6):5025–5036, 1994.
- [84] M. V. Korolkov, J. Manz, G. K. Paramonov, and B. Schmidt. Vibrationally state-selective photoassociation by infrared sub-picosecond laser pulses: model simulations for  $O + H \rightarrow OH(\nu)$ . *Chem. Phys. Lett.*, 260(5-6):604 – 610, 1996.
- [85] Una Marvet and Marcos Dantus. Femtosecond photoassociation spectroscopy: coherent bond formation. *Chem. Phys. Lett.*, 245(4-5):393 – 399, 1995.
- [86] Peter Backhaus, Burkhard Schmidt, and Marcos Dantus. Control of photoassociation yield: a quantum-dynamical study of the mercury system to explore the role of pulse duration from nanoseconds to femtoseconds. *Chem. Phys. Lett.*, 306(1-2):18 – 24, 1999.
- [87] A. Vardi, D. Abrashkevich, E. Frishman, and M. Shapiro. Theory of radiative recombination with strong laser pulses and the formation of ultracold molecules via stimulated photo-recombination of cold atoms. *J. Chem. Phys.*, 107(16):6166–6174, 1997.

- [88] J. Vala, O. Dulieu, F. Masnou-Seeuws, P. Pillet, and R. Kosloff. Coherent control of cold-molecule formation through photoassociation using a chirped-pulsed-laser field. *Phys. Rev. A*, 63(1):013412, 2000.
- [89] E. Luc-Koenig, R. Kosloff, F. Masnou-Seeuws, and M. Vatasescu. Photoassociation of cold atoms with chirped laser pulses: Time-dependent calculations and analysis of the adiabatic transfer within a two-state model. *Phys. Rev. A*, 70(3):033414, 2004.
- [90] E. Luc-Koenig, M. Vatasescu, and F. Masnou-Seeuws. Optimizing the photoassociation of cold atoms by use of chirped laser pulses. *Eur. Phys. J. D*, 31:239–262, 2004.
- [91] Christiane P. Koch, Eliane Luc-Koenig, and Françoise Masnou-Seeuws. Making ultracold molecules in a two-color pump-dump photoassociation scheme using chirped pulses. *Phys. Rev. A*, 73(3):033408, 2006.
- [92] A. M. Weiner. Femtosecond pulse shaping using spatial light modulators. *Rev. Sci. Instrum.*, 71(5):1929–1960, 2000.
- [93] Benjamin L. Brown, Alexander J. Dicks, and Ian A. Walmsley. The coherent effect of chirped femtosecond laser pulses on the formation of ultracold molecules in a magneto-optical trap. *Opt. Commun.*, 264:278–284, 2006.
- [94] Peter Sta anum, Stephan D. Kraft, Jorg Lange, Roland Wester, and Matthias Weidemüller. Experimental investigation of ultracold atom-molecule collisions. *Phys. Rev. Lett.*, 96(2):023201, 2006.
- [95] Christiane P. Koch, Ronnie Kosloff, and Françoise Masnou-Seeuws. Short-pulse photoassociation in rubidium below the  $D_1$  line. *Phys. Rev. A*, 73(4):043409, 2006.
- [96] Ulrich Poschinger, Wenzel Salzmann, Roland Wester, Matthias Weidemüller, Christiane P. Koch, and Ronnie Kosloff. Theoretical model for ultracold molecule formation via adaptive feedback control. *J. Phys. B*, 39:S1001–S1015, 2006.
- [97] Jordi Mur-Petit, Eliane Luc-Koenig, and Françoise Masnou-Seeuws. Dynamical interferences to probe short-pulse photoassociation of Rb atoms and stabilization of  $Rb_2$  dimers. *Phys. Rev. A*, 75(6):061404, 2007.
- [98] Christiane P. Koch and Robert Moszyński. Engineering an all-optical route to ultracold molecules in their vibronic ground state. *Phys. Rev. A*, 78(4):043417, 2008.
- [99] Christiane P. Koch, Mamadou Ndong, and Ronnie Kosloff. Two-photon coherent control of femtosecond photoassociation. *Faraday Discuss.*, 142:389–402, 2009.

- [100] Fredrik Fatemi, Kevin M. Jones, He Wang, Ian Walmsley, and Paul D. Lett. Dynamics of photoinduced collisions of cold atoms probed with picosecond laser pulses. *Phys. Rev. A*, 64(3):033421, 2001.
- [101] W. Salzmann, T. Mullins, J. Eng, M. Albert, R. Wester, M. Weidemüller, A. Merli, S. M. Weber, F. Sauer, M. Plewicky, F. Weise, L. Wöste, and A. Lindinger. Coherent transients in the femtosecond photoassociation of ultracold molecules. *Phys. Rev. Lett.*, 100(23):233003, 2008.
- [102] F. Eimer, F. Weise, A. Merli, S. Birkner, F. Sauer, L. Wöste, A. Lindinger, R. Ağanoglu, C. P. Koch, W. Salzmann, T. Mullins, S. Götz, R. Wester, and M. Weidemüller. Spectrally resolved coherent transient signal for ultracold rubidium molecules. *Eur. Phys. J. D*, 2009.
- [103] Sébastien Zamith, Jérôme Degert, Sabine Stock, Béatrice de Beauvoir, Valérie Blanchet, M. Aziz Bouchene, and Bertrand Girard. Observation of coherent transients in ultrashort chirped excitation of an undamped two-level system. *Phys. Rev. Lett.*, 87(3):033001, 2001.
- [104] Jovana Petrovic, David McCabe, Duncan England, Hugo Martay, Melissa Friedman, Alexander Dicks, Emiliya Dimova, and Ian Walmsley. A pump-probe study of the photoassociation of cold rubidium molecules. *Faraday Discuss.*, 142:403–413, 2009.
- [105] David J. McCabe, Duncan G. England, Hugo E. L. Martay, Melissa E. Friedman, Jovana Petrovic, Emiliya Dimova, Béatrice Chatel, and Ian A. Walmsley. Pump-probe study of the formation of rubidium molecules by ultrafast photoassociation of ultracold atoms. *Phys. Rev. A*, 80(3):033404, 2009.
- [106] Hugo E. L. Martay, David J. McCabe, Duncan G. England, Melissa E. Friedman, Jovana Petrovic, and Ian A. Walmsley. Demonstrating coherent control in  $^{85}\text{Rb}_2$  using ultrafast laser pulses: A theoretical outline of two experiments. *Phys. Rev. A*, 80(3):033403, 2009.
- [107] David J. Tannor and Allon Bartana. On the interplay of control fields and spontaneous emission in laser cooling. *J. Phys. Chem. A*, 103(49):10359–10363, 1999.
- [108] P. W. Brumer and M. Shapiro. *Principles of the Quantum Control of Molecular Processes*. Wiley-Interscience, 2003.
- [109] Stuart A. Rice and Meishan Zhao. *Optical Control of Molecular Dynamics*. Wiley-Interscience, 2000.
- [110] E. Dupont, P. B. Corkum, H. C. Liu, M. Buchanan, and Z. R. Wasilewski. Phase-controlled currents in semiconductors. *Phys. Rev. Lett.*, 74(18):3596–3599, 1995.

- [111] Langchi Zhu, Valeria Kleiman, Xiaonong Li, Shao Ping Lu, Karen Trentelman, and Robert J. Gordon. Coherent laser control of the product distribution obtained in the photoexcitation of HI. *Science*, 270(5233):77–80, 1995.
- [112] Langchi Zhu, Kunihiro Suto, Jeanette Allen Fiss, Ryuichi Wada, Tamar Seideman, and Robert J. Gordon. Effect of resonances on the coherent control of the photoionization and photodissociation of HI and DI. *Phys. Rev. Lett.*, 79(21):4108–4111, 1997.
- [113] Doron Meshulach and Yaron Silberberg. Coherent quantum control of multiphoton transitions by shaped ultrashort optical pulses. *Phys. Rev. A*, 60(2):1287–1292, 1999.
- [114] Vadim V. Lozovoy, Igor Pastirk, Katherine A. Walowicz, and Marcos Dantus. Multiphoton intrapulse interference. II. control of two- and three-photon laser induced fluorescence with shaped pulses. *J. Chem. Phys.*, 118(7):3187–3196, 2003.
- [115] Benjamin J. Sussman, Dave Townsend, Misha Yu. Ivanov, and Albert Stolow. Dynamic Stark control of photochemical processes. *Science*, 314(5797):278–281, 2006.
- [116] Benjamin J. Sussman, Jonathan G. Underwood, R. Lausten, Misha Yu. Ivanov, and Albert Stolow. Quantum control via the dynamic Stark effect: Application to switched rotational wave packets and molecular axis alignment. *Phys. Rev. A*, 73(5):053403, 2006.
- [117] David J. Tannor and Stuart A. Rice. Control of selectivity of chemical reaction via control of wave packet evolution. *J. Chem. Phys.*, 83(10):5013–5018, 1985.
- [118] David J. Tannor, Ronnie Kosloff, and Stuart A. Rice. Coherent pulse sequence induced control of selectivity of reactions: Exact quantum mechanical calculations. *J. Chem. Phys.*, 85(10):5805–5820, 1986.
- [119] Bern Kohler, Vladislav V. Yakovlev, Jianwei Che, Jeffrey L. Krause, Michael Messina, Kent R. Wilson, Nikolaus Schwentner, Robert M. Whitnell, and Yi-Jing Yan. Quantum control of wave packet evolution with tailored femtosecond pulses. *Phys. Rev. Lett.*, 74(17):3360–3363, 1995.
- [120] Richard S. Judson and Herschel Rabitz. Teaching lasers to control molecules. *Phys. Rev. Lett.*, 68(10):1500–1503, 1992.
- [121] T C Weinacht and P H Bucksbaum. Using feedback for coherent control of quantum systems. *J. Opt. B*, 4(3):R35–R52, 2002.
- [122] T. Baumert, T. Brixner, V. Seyfried, M. Strehle, and G. Gerber. Femtosecond pulse shaping by an evolutionary algorithm with feedback. *Appl. Phys. B*, 65:779–782, 1997.

- [123] D. Yelin, D. Meshulach, and Y. Silberberg. Adaptive femtosecond pulse compression. *Opt. Lett.*, 22(23):1793–1795, 1997.
- [124] Christopher J. Bardeen, Vladislav V. Yakovlev, Kent R. Wilson, Scott D. Carpenter, Peter M. Weber, and Warren S. Warren. Feedback quantum control of molecular electronic population transfer. *Chem. Phys. Lett.*, 280(1-2):151–158, 1997.
- [125] T. Brixner, N. H. Damrauer, P. Niklaus, and G. Gerber. Photosensitive adaptive femtosecond quantum control in the liquid phase. *Nature*, 414(6859):57–60, 2001.
- [126] A. Assion, T. Baumert, M. Bergt, T. Brixner, B. Kiefer, V. Seyfried, M. Strehle, and G. Gerber. Control of chemical reactions by feedback-optimized phase-shaped femtosecond laser pulses. *Science*, 282(5390):919–922, 1998.
- [127] Robert J. Levis, Getahun M. Menkir, and Herschel Rabitz. Selective bond dissociation and rearrangement with optimally tailored, strong-field laser pulses. *Science*, 292(5517):709–713, 2001.
- [128] M. Strehle and G. Gerber. Feedback-controlled optimization of atomic double ionization. *Multiphoton Processes: ICOMP VIII: 8th International Conference*, 525(1):295–303, 2000.
- [129] B. J. Pearson, J. L. White, T. C. Weinacht, and P. H. Bucksbaum. Coherent control using adaptive learning algorithms. *Phys. Rev. A*, 63(6):063412, 2001.
- [130] J. M. Geremia, Wusheng Zhu, and Herschel Rabitz. Incorporating physical implementation concerns into closed loop quantum control experiments. *J. Chem. Phys.*, 113(24):10841–10848, 2000.
- [131] D. Zeidler, S. Frey, K.-L. Kompa, and M. Motzkus. Evolutionary algorithms and their application to optimal control studies. *Phys. Rev. A*, 64(2):023420, 2001.
- [132] Jianshu Cao, Christopher J. Bardeen, and Kent R. Wilson. Molecular “ $\pi$  pulse” for total inversion of electronic state population. *Phys. Rev. Lett.*, 80(7):1406–1409, 1998.
- [133] Jianshu Cao, Christopher J. Bardeen, and Kent R. Wilson. Molecular  $\pi$  pulses: Population inversion with positively chirped short pulses. *J. Chem. Phys.*, Volume 113(5):1898–1909, 2000.
- [134] Benjamin L Brown and Ian A Walmsley. Analysis of some intuitive approaches to the coherent control of state-selected ultracold molecules. *J. Phys. B*, 39(19):S1055–S1075, 2006.

- [135] Benjamin L. Brown. *Towards coherent control of ultracold molecule formation*. PhD thesis, University of Rochester, 2005.
- [136] G. Kirchoff and R. Bunsen. Chemische analyse durch spectralbeobachtungen. *Annalen der Physik und Chemie*, 189(7):337–381, 1861.
- [137] Daniel A. Steck. Rubidium 85 D line data. available online at <http://steck.us/alkalidata> (revision 0.2), 1 September 2008.
- [138] Daniel A. Steck. Rubidium 87 D line data. available online at <http://steck.us/alkalidata> (revision 2.1), 1 September 2008.
- [139] H. M. J. M. Boesten, C. C. Tsai, J. R. Gardner, D. J. Heinzen, and B. J. Verhaar. Observation of a shape resonance in the collision of two cold  $^{87}\text{Rb}$  atoms. *Phys. Rev. A*, 55(1):636–640, 1997.
- [140] Ph. Courteille, R. S. Freeland, D. J. Heinzen, F. A. van Abeelen, and B. J. Verhaar. Observation of a Feshbach resonance in cold atom scattering. *Phys. Rev. Lett.*, 81(1):69–72, 1998.
- [141] J. L. Roberts, N. R. Claussen, James P. Burke, Chris H. Greene, E. A. Cornell, and C. E. Wieman. Resonant magnetic field control of elastic scattering in cold  $^{85}\text{Rb}$ . *Phys. Rev. Lett.*, 81(23):5109–5112, 1998.
- [142] J. L. Roberts, James P. Burke, N. R. Claussen, S. L. Cornish, E. A. Donley, and C. E. Wieman. Improved characterization of elastic scattering near a Feshbach resonance in  $^{85}\text{Rb}$ . *Phys. Rev. A*, 64(2):024702, 2001.
- [143] N. R. Claussen, S. J. J. M. F. Kokkelmans, S. T. Thompson, E. A. Donley, E. Hodby, and C. E. Wieman. Very-high-precision bound-state spectroscopy near a  $^{85}\text{Rb}$  Feshbach resonances. *Phys. Rev. A*, 67(6):060701, 2003.
- [144] E. G. M. van Kempen, S. J. J. M. F. Kokkelmans, D. J. Heinzen, and B. J. Verhaar. Interisotope determination of ultracold rubidium interactions from three high-precision experiments. *Phys. Rev. Lett.*, 88(9):093201, 2002.
- [145] A. Marte, T. Volz, J. Schuster, S. Dürr, G. Rempe, E. G. M. van Kempen, and B. J. Verhaar. Feshbach resonances in rubidium 87: Precision measurement and analysis. *Phys. Rev. Lett.*, 89(28):283202, 2002.
- [146] J. D. Miller, R. A. Cline, and D. J. Heinzen. Photoassociation spectrum of ultracold Rb atoms. *Phys. Rev. Lett.*, 71(14):2204–2207, 1993.
- [147] R. A. Cline, J. D. Miller, and D. J. Heinzen. Study of  $\text{Rb}_2$  long-range states by high-resolution photoassociation spectroscopy. *Phys. Rev. Lett.*, 73(5):632–635, 1994.

- [148] R. A. Cline, J. D. Miller, and D. J. Heinzen. Errata: Study of  $\text{Rb}_2$  long-range states by high-resolution photoassociation spectroscopy. *Phys. Rev. Lett.*, 73(19):2636, 1994.
- [149] D. Leonhardt and J. Weiner. Direct two-color photoassociative ionization in a rubidium magneto-optic trap. *Phys. Rev. A*, 52(6):R4332–R4335, 1995.
- [150] D. Leonhardt and J. Weiner. Erratum: Direct two-color photoassociative ionization in a rubidium magneto-optic trap. *Phys. Rev. A*, 53(4):2904, 1996.
- [151] Carl Wieman, Gwenn Flowers, and Sarah Gilbert. Inexpensive laser cooling and trapping experiment for undergraduate laboratories. *Am. J. Phys.*, 63(4):317–330, 1995.
- [152] K. B. MacAdam, A. Steinbach, and C. Wieman. A narrow-band tunable diode laser system with grating feedback, and a saturated absorption spectrometer for Cs and Rb. *Am. J. Phys.*, 60(12):1098–1111, 1992.
- [153] L. Ricci, M. Weidemüller, T. Esslinger, A. Hemmerich, C. Zimmermann, V. Vuletic, W. König, and T. W. Hänsch. A compact grating-stabilized diode laser system for atomic physics. *Opt. Commun.*, 117(5-6):541 – 549, 1995.
- [154] Carl E. Wieman and Leo Hollberg. Using diode lasers for atomic physics. *Rev. Sci. Instrum.*, 62(1):1–20, 1991.
- [155] Daryl W. Preston. Doppler-free saturated absorption: Laser spectroscopy. *Am. J. Phys.*, 64(11):1432–1436, 1996.
- [156] David A. Smith and Ifan G. Hughes. The role of hyperfine pumping in multilevel systems exhibiting saturated absorption. *American Journal of Physics*, 72(5):631–637, 2004.
- [157] Umakant D. Rapol, Ajay Wasan, and Vasant Natarajan. Loading of a Rb magneto-optic trap from a getter source. *Phys. Rev. A*, 64(2):023402, 2001.
- [158] Steven Chu, L. Hollberg, J. E. Bjorkholm, Alex Cable, and A. Ashkin. Three-dimensional viscous confinement and cooling of atoms by resonance radiation pressure. *Phys. Rev. Lett.*, 55(1):48–51, 1985.
- [159] Wolfgang Ketterle, Kendall B. Davis, Michael A. Joffe, Alex Martin, and David E. Pritchard. High densities of cold atoms in a dark spontaneous-force optical trap. *Phys. Rev. Lett.*, 70(15):2253–2256, 1993.
- [160] F. Verluise, V. Laude, Z. Cheng, Ch. Spielmann, and P. Tournois. Amplitude and phase control of ultrashort pulses by use of an acousto-optic programmable dispersive filter: pulse compression and shaping. *Opt. Lett.*, 25(8):575–577, 2000.

- [161] Donna Strickland and Gerard Mourou. Compression of amplified chirped optical pulses. *Opt. Commun.*, 56(3):219 – 221, 1985.
- [162] Sterling Backus, Charles G. Durfee III, Margaret M. Murnane, and Henry C. Kapteyn. High power ultrafast lasers. *Rev. Sci. Instrum.*, 69(3):1207–1223, 1998.
- [163] C. Iaconis and I. A. Walmsley. Spectral phase interferometry for direct electric-field reconstruction of ultrashort optical pulses. *Opt. Lett.*, 23(10):792–794, 1998.
- [164] Matthijs P. A. Branderhorst, Pablo Londero, Piotr Wasylczyk, Constantin Brif, Robert L. Kosut, Herschel Rabitz, and Ian A. Walmsley. Coherent control of decoherence. *Science*, 320(5876):638–643, 2008.
- [165] M P A Branderhorst, I A Walmsley, R L Kosut, and H Rabitz. Optimal experiment design for quantum state tomography of a molecular vibrational mode. *J. Phys. B*, 41(7):074004, 2008.
- [166] Giulio Cerullo and Sandro De Silvestri. Ultrafast optical parametric amplifiers. *Rev. Sci. Instrum.*, 74(1):1–18, 2003.
- [167] Joseph Ladislav Wiza. Microchannel plate detectors. *Nuclear Instruments and Methods*, 162:587–601, 1979.
- [168] S.D. Kraft, J. Mikosch, P. Staantum, J. Deiglmayr, J. Lange, A. Fioretti, R. Wester, and M. Weidemüller. A high-resolution time-of-flight mass spectrometer for the detection of ultracold molecules. *Appl. Phys. B*, 89(4):453–457, 2007.
- [169] A. R. L. Caires, V. A. Nascimento, D. C. J. Rezende, V. S. Bagnato, and L. G. Marcassa. Atomic density and light intensity dependences of the  $\text{Rb}_2$  molecule formation rate constant in a magneto-optical trap. *Phys. Rev. A*, 71(4):043403, 2005.
- [170] J. Lozeille, A. Fioretti, C. Gabbanini, Y. Huang, H.K. Pechkis, D. Wang, P.L. Gould, E.E. Eyler, W.C. Stwalley, M. Aymar, and O. Dulieu. Detection by two-photon ionization and magnetic trapping of cold  $\text{Rb}_2$  triplet state molecules. *Eur. Phys. J. D*, 39:261–269, 2006.
- [171] J. E. Sansonetti. Wavelengths, transition probabilities, and energy levels for the spectra of rubidium (Rb I through Rb XXXVII). *Journal of Physical and Chemical Reference Data*, 35(1):301–421, 2006.
- [172] Jennings Y. Seto, Robert J. Le Roy, Jean Vergès, and Claude Amiot. Direct potential fit analysis of the  $X^1\Sigma_g^+$  state of  $\text{Rb}_2$ : Nothing else will do! *J. Chem. Phys.*, 113(8):3067–3076, 2000.

- 
- [173] James P. Burke, John L. Bohn, B. D. Esry, and Chris H. Greene. Prospects for mixed-isotope Bose-Einstein condensates in rubidium. *Phys. Rev. Lett.*, 80(10):2097–2100, 1998.
- [174] Nille N. Klausen, John L. Bohn, and Chris H. Greene. Nature of spinor Bose-Einstein condensates in rubidium. *Phys. Rev. A*, 64(5):053602, 2001.
- [175] T Bergeman, J Qi, D Wang, Y Huang, H K Pechkis, E E Eyler, P L Gould, W C Stwalley, R A Cline, J D Miller, and D J Heinzen. Photoassociation of  $^{85}\text{Rb}$  atoms into  $0_u^+$  states near the  $5S + 5P$  atomic limits. *J. Phys. B*, 39(19):S813–S823, 2006.
- [176] Su Jin Park, Sung Won Suh, Yoon Sup Lee, and Gwang-Hi Jeung. Theoretical study of the electronic states of the  $\text{Rb}_2$  molecule. *Journal of Molecular Spectroscopy*, 207:129–135, 2001.
- [177] M Aymar, S Azizi, and O Dulieu. Model-potential calculations for ground and excited  $\Sigma$  states of  $\text{Rb}^+$ ,  $\text{Cs}^+$  and  $\text{RbCs}^+$  ions. *J. Phys. B*, 36:4799–4812, 2003.